Université du Québec
Institut National de la Recherche Scientifique
Énergie Matériaux Télécommunications

TIME–FREQUENCY ANALYSIS OF NONLINEAR TERAHERTZ SIGNALS DUE TO HOT ELECTRONS IN THE NONPARABOLIC CONDUCTION BAND OF n–DOPED $\mathbf{In_{0.57}Ga_{0.43}As}$ FILMS

By

Carlos Miguel García Rosas

A dissertation submitted in partial fulfillment of the requirements for the degree of
Master of Science, M. Sc.
in Energy and Material Sciences

Jury Members

President of the jury & Internal examiner	Dr. Luca Razzari INRS–EMT
External examiner	Dr. Jean–Michel Ménard University of Ottawa
Research director	Dr. Tsuneyuki Ozaki INRS–EMT

©Carlos Miguel García Rosas, 2021

Acknowledgements

The first person that I should have to thank, since I arrived for first time to this country, is Professor Ozaki. Since that time, he trusted me with full freedom a challenging research project, although he knew that my weakness was the experimental environment. He gave me the opportunity to use and play his laboratory resources. Moreover, even half of my master's degree was complete between the pandemic period, he motivates me to keep working on simulations related to my master's main research project. Additionally, Professor Ozaki was always open to work with potential collaborations and participate in international conferences.

I would really like to acknowledge my colleague and friend Dr. Xavier Ropagnol for his support, help, strong and deep discussions during my master's degree. Even though I do not have a strong experimental background, he was always there to explain and answer me any question that I had. It was big pleasure to work with you at the lab.

One person that was always open to explain me and call my curiosity to learn more about solid state of physics and condensed matter was my colleague Dr. Xin Chai. His help and motivation during the internship I made with the group and during my first year of my master's degree, is something that I would always be thankful.

I am also very thankful to Prof. François Blanchard for his insightful discussions and comments on our PRL manuscript.

I would sincerely like to thank Prof. Alejandro Reyes Coronado. Even you were not any more my research supervisor, you were always aware of my master's degree and how I was going in a new country. Thank you so much for sharing with me a conference as research colleagues.

I am extremely grateful for having such a good party friends. To Paquito, thank you so much for being and sharing some months with me here in Montreal. Your friendship was necessary during these hard times. To Juan Carlos, Lupillo and Alonso, thank you so much for being with me in this journey and never let me die alone at any party ☻. Also, I have no words to thank the *rum of my Coca–Cola:* Kim T. In a short period of time you became one of my closest friends during this pandemic and you are someone that I could always talk about anything even though our fields of knowledge are not the same. Lastly, I have to mention my faraway friends Juan T., Juan Jaime, Trejo and Emiliano. Even a continent or country separate us, you were always there to listen me at any time.

Great thanks to the members of the jury: Prof. Luca Razzari and Prof. Jean–Michel Ménard for reviewing and evaluating my thesis.

I would like to acknowledge the scholarship and financial support given by Globalink Graduate Fellowship Program to complete my master's degree.

Finally, I would like to thank my family, especially to my sister and two brothers: Susana, Julio and Poncho. Ustedes son mi motor y fuerza para salir adelante en esta vida. Do not worry so much about what is happening today, I am sure that everything will become better and better... just keep being strong.

Abstract

The interaction of intense, few–cycle terahertz (THz) pulses with matter and the observation of nonlinear terahertz effects have recently attracted considerable attention from the scientific community. Such studies are greatly benefiting from a unique aspect of terahertz spectroscopy, that is, coherent generation and detection combined with the pump–probe technique, which allows time–resolved terahertz electric field measurements. Previous works have studied the evolution of nonlinear effects and carrier dynamics during the interaction of subcycle and few–cycle terahertz pulses with doped semiconductors. Chai *et al.* performed nonlinear terahertz time–domain spectroscopy experiments on n–doped $\mathrm{In}_{0.57}\mathrm{Ga}_{0.43}\mathrm{As}$ using a quasi–half–cycle terahertz pulse with a fundamental frequency of less than 0.2 THz, demonstrating the subcycle control of terahertz nonlinearities and terahertz high–frequency generation based on intraband carrier scattering effects.

In this dissertation, we demonstrate strong nonlinear terahertz effects induced by an intense multi–cycle terahertz pulse in a doped semiconductor thin film. An important finding of this thesis is that we clarify, for the first time, the mechanism that results in the generation of low– and high–frequency components, which are purely related to intravalley effects, reflecting the nonparabolicity of the conduction band. Using the Gábor transform, we have clarified the time of emission of photons at different frequencies, providing a better understanding of the related carrier dynamics. We would like to note that similar low– and high–frequency components have been observed in recent reports on intense terahertz–matter interactions, such as those observed in the high–order harmonic spectra from graphene [H. Hafez *et al.*, Nature, **561**, 507–511 (2018)]. Considering the impact that nonlinear optics has had in physics and applied physics, and the recent rapid progress in intense terahertz–matter interactions and nonlinear terahertz optics, we believe that the new knowledge that the current work presents would be of high importance and interest.

We also detail the different mechanisms responsible for the high–order harmonic emission for both relatively low– and high–frequency (0.2 THz ~ 1.5 THz) terahertz pulses with incident peak electric fields ranging from 100 kV/cm up to 500 kV/cm. Our results show that for relatively low–frequency multi–cycle terahertz pulses and high incident peak fields, the carriers are accelerated to high average energy, resulting in the truncation in the current density, leading to discrete high–order harmonic generation. To explain the high–order harmonic generation, we analyze the carrier populations in the Γ, L and X valleys, with a 0.2 THz pulse, showing a drastic decay in the carrier population of the Γ valley at a certain time. At that moment, because of the high incident field (350 kV/cm), the ponderomotive acceleration is strong enough that the carriers gain sufficient kinetic energy to efficiently undergo intervalley scattering from the Γ to the L and X valleys [X. Chai *et al.*, Phys. Rev. Lett. **121**, 143901 (2018)]. The high–order harmonic generation is mainly caused by the intervalley transitions of the carriers from the Γ valley to L and X valleys, and also from L valleys to X valleys and vice versa. For relatively high–frequency multi–cycle terahertz pulses and low incident peak fields, we find that it is challenging to have current truncations faster than the duration of the half–cycle of the original incident terahertz waveform, and as a result, harmonics are harder to see.

Keywords: Terahertz, Multi–cycle terahertz pulses, High–order harmonic generation, Low– and high–frequency components, Inter– and intra–valley scattering, Gábor transform.

Université du Québec
Institut National de la Recherche Scientifique
Énergie Matériaux Télécommunications

ANALYSE TEMPS-FRÉQUENCE DES VARIATIONS DE SIGNAL TERAHERTZ NON–LINÉAIRE INDUIT PAR LA GENERATION D'ELECTRONS CHAUDS DANS LA BANDE DE CONDUCTION NON PARABOLIQUE DE COUCHE MINCE D'$In_{0.57}Ga_{0.43}As$ DOPÉ DE TYPE N

Par
Carlos Miguel García Rosas

Mémoire présenté pour l'obtention du grade de
Maître es Sciences, M. Sc.
en sciences de l'énergie et des matériaux

Jury d'evaluation

Président du jury & Examinateur interne	Dr. Luca Razzari INRS–EMT
Examinateur externe	Dr. Jean–Michel Ménard University of Ottawa
Directeur de recherche	Dr. Tsuneyuki Ozaki INRS–EMT

@Carlos Miguel García Rosas, 2021

Résumé

L'interaction d'impulsions térahertz (THz) intenses de quelques cycles avec la matière et l'observation des effets térahertz non linéaires ont récemment attiré l'attention de la communauté scientifique. Ces études bénéficient grandement d'un aspect unique de la spectroscopie térahertz, à savoir la génération et la détection cohérentes combinées à la technique pompe–sonde, qui permet de mesurer le champ électrique térahertz en fonction du temps. Des travaux antérieurs ont étudié l'évolution des effets non linéaires et de la dynamique des porteurs pendant l'interaction des impulsions THz sous–cycle et de quelques cycles avec un semi–conducteur dopé. Chai *et al.* ont réalisé des expériences de spectroscopie non–linéaire THz dans le domaine temporel sur un échantillon d'$\mathrm{In_{0.57}Ga_{0.43}As}$ dopés n en utilisant une impulsion de térahertz quasi–demi–cycle avec une fréquence fondamentale inférieure à 0.2 THz, démontrant le contrôle sous–cycle des interacrions non–linéaire THz et la génération de haute fréquence térahertz basée sur les effets de diffusion inter–bande des porteurs de charges.

Dans cette thèse, nous démontrons des effets THz non–linéaires forts induits par une impulsion térahertz intense à plusieurs cycles dans la couche mince du semi–conducteur dopé. Une conclusion importante de cette thèse est que nous clarifions, pour première fois, le mécanisme qui entraîne la génération de composantes à basse et haute fréquence, qui sont purement liées à des effets intra–vallée, reflétant la non–parabolicité de la bande de conduction. En utilisant la transformée de Gábor, nous avons clarifié le temps d'émission des photons à différentes fréquences, permettant une meilleure compréhension de la dynamique correspondantes. Nous aimerions noter que des composantes similaires à basse et haute fréquence ont été observées dans des rapports récents sur les interactions térahertz–matière intenses, comme celles observées dans les spectres harmoniques d'ordre supérieur du graphène [H. Hafez *et al.*, Nature, **561**, 507–511 (2018)]. Compte tenu de l'impact que l'optique non linéaire a eu en physique et en physique appliquée, et des récents progrès rapides dans les interactions térahertz–matière intenses et l'optique térahertz non linéaire, nous pensons que les nouvelles connaissances que présentent les travaux actuels sont d'une grande importance et d'un grand intérêt.

Nous détaillons également les différents mécanismes responsables de l'émission d'harmoniques d'ordre élevé pour les impulsions térahertz a basse et haute fréquence THz (0.2 THz ~ 1.5 THz) avec des champs électriques de crête incidents allant de 100 kV/cm à 500 kV/cm. Nos résultats montrent que pour les impulsions térahertz à fréquences relativement basses, à cycles multiples et à champs électriques de crête incidents élevés, les porteurs sont accélérés à une énergie moyenne élevée et la troncature de la densité de courant est d'abord obtenue, ce qui conduit à la génération d'harmoniques discrètes d'ordre élevé. Pour expliquer la génération d'harmoniques d'ordre élevé, nous analysons les populations de porteurs dans les vallées Γ, L et X, avec une impulsion de 0.2 THz, montrant une décroissance drastique de la population des porteurs de la vallée Γ autour de 16 ps. À ce moment, en raison du champ élevé (350 kV/cm), l'accélération ponderomotrice est suffisamment forte pour que les porteurs acquièrent suffisamment d'énergie cinétique pour subir efficacement la diffusion intermittente des vallées Γ vers les vallées L et X [X. Chai *et al.*, Phys. Rev. Lett. **121**, 143901 (2018)]. La génération d'harmoniques d'ordre élevé est principalement causée par les transitions intermittentes des porteurs de la vallée Γ vers les vallées L et X, et aussi des vallées L vers les vallées X et vice versa. Pour les impulsions térahertz à fréquences relativement élevées et à cycles multiples et les champs de crête faibles, nous constatons qu'il est difficile d'avoir des troncatures de courant plus rapides que la durée du demi–cycle de la forme d'onde térahertz incidente originale, et par conséquent, les harmoniques sont plus difficiles à voir.

Mots-clés: Térahertz, Impulsions térahertz à cycles multiples, Génération d'harmoniques d'ordre élevé, composantes basse et haute fréquence, Diffusion inter– et intra–vallée, Transformée de Gábor.

Sommaire Récapitulatif

0.1 Introduction

Le rayonnement térahertz (THz) a suscité un vif intérêt de la part des communautés scientifiques et technologiques, en raison de ses propriétés non invasives et non ionisantes et de ses capacités spectroscopiques et de détection exceptionnelles [SR.1, SR.2]. Par définition $1\,\mathrm{THz} = 10^{12}\,\mathrm{Hz}$ et correspond à une longueur d'onde de $300\,\mu\mathrm{m}$ $\left(33\,\mathrm{cm}^{-1}\right)$ et une période de 1 picoseconde. Via la constante de Boltzmann, 1 THz a une température d'énergie thermique de 48 Kelvin et une énergie photonique de 4.1 meV. En général, la gamme de fréquences de rayonnement de THz se situe entre 0.1 et 10 THz du spectre électromagnétique [voir la figure 1] [SR.3].

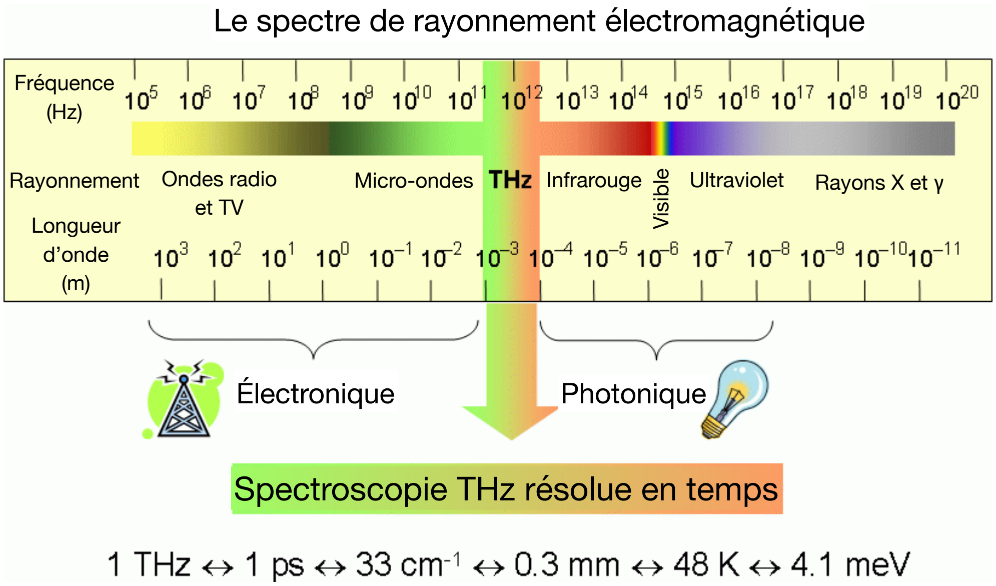
Le spectre de rayonnement électromagnétique
Fréquence (Hz)
10^5 10^6 10^7 10^8 10^9 10^{10} 10^{11} 10^{12} 10^{13} 10^{14} 10^{15} 10^{16} 10^{17} 10^{18} 10^{19} 10^{20}
Rayonnement
Ondes radio et TV
Micro-ondes
THz
Infrarouge
Visible
Ultraviolet
Rayons X et γ
Longueur d'onde (m)
10^3 10^2 10^1 10^0 10^{-1} 10^{-2} 10^{-3} 10^{-4} 10^{-5} 10^{-6} 10^{-7} 10^{-8} 10^{-9} 10^{-10} 10^{-11}
Électronique
Photonique
Spectroscopie THz résolue en temps
1 THz ↔ 1 ps ↔ 33 cm^{-1} ↔ 0.3 mm ↔ 48 K ↔ 4.1 meV

Figure 1: Le spectre de rayonnement électromagnétique [SR.3].

Historiquement, nous avons des sources de rayonnement des deux côtés du spectre THz, dans lesquelles les sources électroniques et photoniques ont été utilisées dans le domaine du millimètre et du proche infrarouge (NIR), respectivement [SR.1, SR.2]. Mais le manque de sources et de détecteurs THz a laissé un vitrou dans la compréhension des phénomènes physiques à ces fréquences particulières et une technique pour caractériser ou comprendre ce type de phénomènes est la spectroscopie dans le domaine temporelle [SR.1]. Un aspect technique de la spectroscopie THz est la génération et la détection cohérentes combinées avec la technique pompe sonde, qui permet de mesurer le champ électrique résolu en temps [SR.4 – SR.7]. La spectroscopie dans le domaine temporel (time–domain spectroscopy, TDS) est une méthode commune et une technique puissante pour étudier les propriétés diélectriques des matériaux et tous les systèmes ayant une configuration similaire, où le faisceau laser optique est séparé en deux parties: une pour la génération de THz et une autre pour la détection de THz, comme le montre la figure 2.

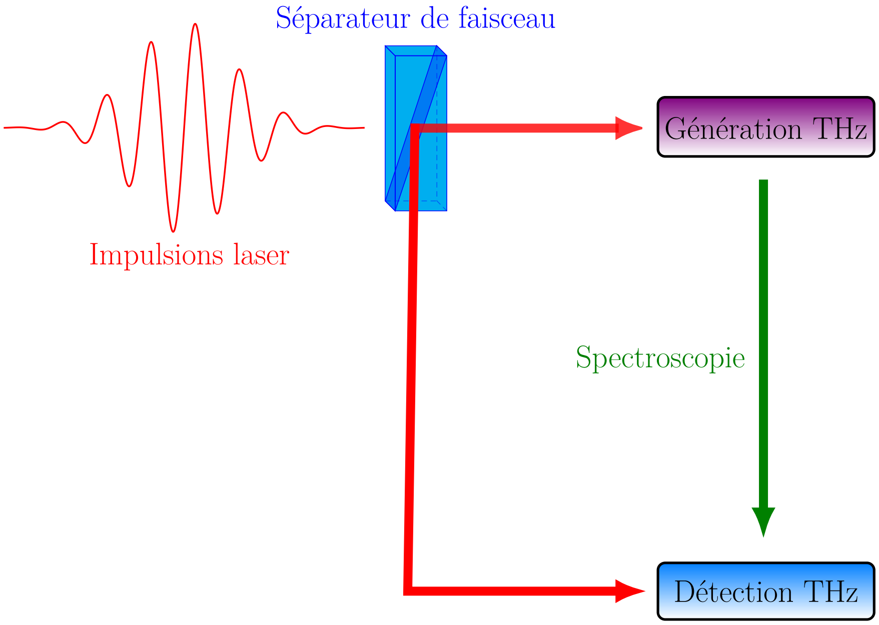

Figure 2: Schéma d'un système de spectroscopie THz résolue en temps.

Parce que les ondes THz ont comme voisines les ondes micro–ondes et les ondes infra–rouges, la technologie THz a une gamme importante d'applications en empruntant des techniques aux deux autres gammes d'ondes. Certaines sont, l'imagerie, télécommunication et diagnostique biomédicale [SR.8 – SR.10], mais nous pouvons aussi utiliser ondes THz pour étudier les effets optiques non linéaires, la dynamique des porteurs et la génération d'harmoniques d'ordre élevé des matériaux [SR.11 – SR.17]. Des travaux antérieurs ont étudié l'évolution des effets non linéaires et de la dynamique des porteurs pendant l'interaction des impulsions sous–cycle et de quelques cycle THz avec un semi–conducteur dopé [SR.11 – SR.13, SR.18].

0.1.1 Physique des semi–conducteurs

Les matériaux ayant des bandes pleines, séparées par une bande interdite (E_g) sont connus sous le nom de semi–conducteurs ou d'isolants. Le point essentiel est que le potentiel chimique réside dans une bande interdite séparant les états pleins des états vides. Les matériaux ayant une bande interdite plus petite sont considérés comme des semi–conducteurs et ceux ayant une bande interdite plus grande sont généralement des isolants. De plus, un semi–conducteur a une conductivité électrique entre un métal et un isolant. Les propriétés des semi–conducteurs dépendent fortement de la différence d'énergie (généralement de l'ordre de ~eV), de la température et des impuretés [SR.19 – SR.21].

Le vide laissé par mouvement continu dans l'espace d'un électron, connu sous le nom de trou, peut être considéré comme une particule chargée positivement qui se déplace à travers une structure cristalline [SR.19 – SR.21]. Ainsi, l'excitation d'un électron dans la bande de conduction fait apparaître un électron dans la bande de conduction et un trou dans la bande de valence. L'électron et le trou sont tous deux connus sous le nom de porteurs (paire électron–trou) [voir la figure 3]. Lorsqu'un champ de phonons, un champ électromagnétique ou électrique externe est appliqué à un semi–conducteur, des porteurs libres sont générés, ce qui entraîne une variation de conductivité. Cependant, la génération de porteurs peut être réalisée par des particules de haute énergie, comme des électrons ou des ions rapides.

Figure 3: Génération de paires électrons–trous (porteurs) dans les semi–conducteurs. Les cercles rouges et blancs représentent respectivement les électrons et les trous.

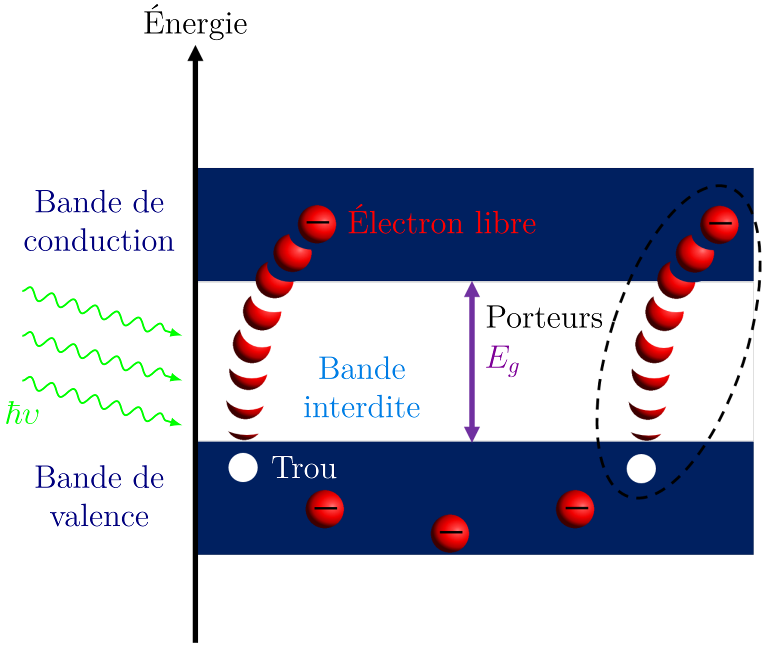

En outre, le calcul de la conductivité ou de la densité de courant d'un semi–conducteur peut être effectué à l'aide de l'équation de transport de Boltzmann, en tenant compte des contributions de la bande de valence et de la bande de conduction. L'équation de transport de Boltzmann est une équation cinétique générale qui fournit une base précise pour la caractérisation des fonctions de distribution de l'énergie et de l'espace [SR.19 – SR.21]. Tout d'abord, nous devons trouver une équation de mouvement pour une fonction de distribution spatiale de phase en présence d'une force appliquée aux électrons. Nous pouvons ainsi caractériser le comportement des particules face à des forces collectives de longue portée. Ensuite, pour décrire le transport des porteurs, nous devons considérer la contribution des forces de collision a de courte distance, approximativement. À la fin, nous saurons comment la niveau de Fermi (dans la physique des semi–conducteurs, nous désignons souvent le potentiel chimique par le niveau de Fermi) se déplace en réponse à ces forces, et nous pourrons calculer des choses comme la densité du courant. Cependant, l'équation de transport de Boltzmann est une équation différentielle complexe qui ne peut pas être résolue facilement, mais nous pouvons mettre en œuvre une approche analytique d'ensemble de bandes de Monte–Carlo pour la résoudre numériquement [SR.13, SR.22 – SR.27]. La méthode de Monte–Carlo d'ensemble est une méthode numérique statistique utilisée pour obtenir des informations physiques à partir d'expériences simulées. Avec cette méthode, nous pouvons simuler des processus aléatoires en modélisant les fonctions de distribution des particules en suivant le mouvement réel de chaque particule. De nombreux auteurs ont publié dans des articles scientifiques, différents types de méthodes de Monte–Carlo pour résoudre des problèmes de transport spécifiques [SR.28 – SR.31]. Cependant, dans le chapitre suivant, nous allons discuter et montrer les points pertinents et importants de la méthode de Monte–Carlo que nous mettons en œuvre pour étudier et comprendre la dynamique des porteurs transitoires et les effets non linéaires de THz.

0.2 Équations de transport des transporteurs

Les électrons et les trous dans les bandes de conduction et de valence ont un mouvement quasi libre dans l'espace et en énergie et peuvent obtenir de l'énergie d'un champ extérieur. Le transport des porteurs dans les semi–conducteurs présentant des défauts de cristallographie ou de réseau (impuretés) et des vibrations de réseau (phonons), est soumis à la diffusion avec un chemin libre moyen λ entre les événements de diffusion [SR.21]. L'interaction des électrons qui interagissent avec les imperfections du réseau, telles que les impuretés, les phonons optiques ou acoustiques, les émissions de photons, etc. est appelée événement de diffusion. Chaque événement de diffusion qui se produit modifie l'élan et le mouvement du porteur. Néanmoins, peu d'événements de diffusion, tels que la diffusion inélastique, peuvent changer radicalement l'énergie du porteur. En général, après que le porteur a reçu suffisamment d'énergie du champ pour permettre une diffusion inélastique, plusieurs événements de diffusion élastique sont suivis d'un événement inélastique [SR.21, SR.23, SR.27].

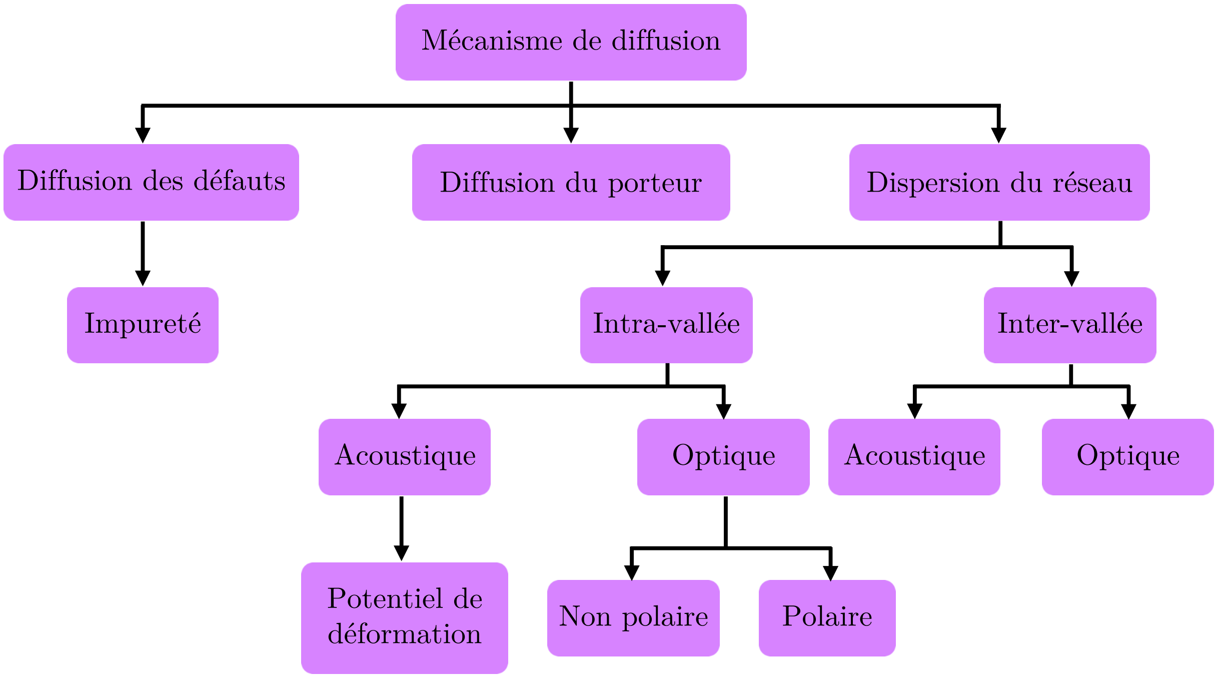

Figure 4: Mécanismes de diffusion dans un semi–conducteur typique.

Les mécanismes de diffusion essentiels dans un semi–conducteur qui doivent être pris en compte dans un algorithme de calcul typique, qui applique une méthode d'échantillonnage aléatoire répété pour faire des estimations numériques de paramètres inconnus [SR.21, SR.23, SR.27], sont énumérés dans la figure 4. Les mécanismes de diffusion sont généralement divisés en: (i) la diffusion causée par des défauts du cristal ou du réseau (événement de diffusion élastique), (ii) la diffusion du réseau entre les électrons/trous et les vibrations du réseau ou les phonons (événement de diffusion inélastique) et (iii) la diffusion entre les particules elles–mêmes (événement de diffusion inélastique ou élastique) [SR.27].

Les matériaux semi–conducteurs à bande interdite indirecte possèdent des vallées multisatellites avec un minimum à la limite de la bande de conduction dans différentes directions cristallographiques. Lorsque la diffusion des porteurs se produit à l'intérieur d'une de ces vallées satellites, nous avons une diffusion intra–vallée, et lorsqu'il y a diffusion d'une vallée satellite à une autre, une diffusion inter–vallée se produit. À titre d'exemple, la figure 5 montre la structure de bande de l'$In_{0.57}Ga_{0.43}As$, où la vallée satellitaire la plus basse est la vallée Γ. Les effets de diffusion possibles qui peuvent se produire, tels que les diffusions intra– et inter–vallées, sont illustrés. La séparation d'énergie entre les vallées Γ et la vallée L est de $\Delta_{\Gamma L} = E_L - E_g = 0.55$ eV, et celle entre les vallées Γ et la vallée X est de $\Delta_{\Gamma X} = E_X - E_g = 0.67$ eV [SR.32].

Figure 5: Schéma de la structure de la bande $\mathbf{In_{0.57}Ga_{0.43}As}$ [SR.33].

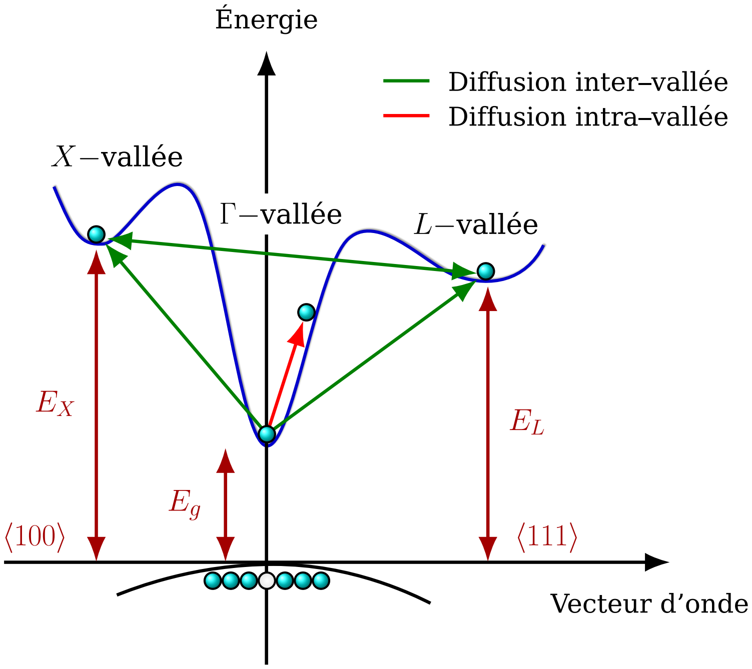

Pour décrire la dynamique des porteurs transitoires, nous devons supposer que la plupart des événements de diffusion ne sont pas inélastiques et qu'il faut distinguer tous les types de collisions qui se produisent. Ensuite, le temps constant et indépendant de l'énergie qui existe entre les événements de diffusion doit être affiné. Dans les semi–conducteurs, une distribution de porteurs déformée peut être approchée par une fonction de distribution de Boltzmann à l'intérieur des bandes, en supposant que la température du porteur est au–dessus de la température du réseau du cristal [SR.21].

0.2.1 L'équation de transport de Boltzmann

L'équation de transport de Boltzmann est une équation générale qui peut être utilisée lorsque nous voulons inclure et décrire les effets du potentiel du réseau. Ici, nous devons considérer les situations dans lesquelles les forces appliquées (comme un champ électrique) varient lentement dans l'espace, ce qui implique qu'elles sont essentiellement constantes dans la région concernée. De plus, les échelles spatiales doivent être suffisamment grandes pour que nous puissions considérer les électrons comme des paquets d'ondes dont la position et le vecteur d'onde sont bien définis. Ainsi, pour examiner la probabilité qu'un paquet d'ondes à une position $\mathbf{r}$, un vecteur d'onde $\mathbf{k}$ et un temps t soit occupé, nous définissons

$$f(x,y,z,k_x,k_y,k_z,t) \coloneqq f\left(\mathbf{r},\mathbf{k},t\right), \tag{1}$$

comme la probabilité qu'un état électronique avec la position $\mathbf{r}$ et le vecteur d'onde $\mathbf{k}$ soit occupé au temps t.

En l'absence de collisions, un électron à $(\mathbf{r},\mathbf{k})$ et au moment t doit avoir été à $\mathbf{r}-\mathbf{v}dt$, $\mathbf{k}-\hbar^{-1}\mathbf{F}dt$ une fois dt plus tôt. Ainsi, si *aucune collision* ne se produit, l'équation de mouvement pour $f\left(\mathbf{r},\mathbf{k},t\right)$ est donnée par

$$f\left(\mathbf{r},\mathbf{k},t\right) = f\left(\mathbf{r}-\mathbf{v}dt, \mathbf{k}-\frac{1}{\hbar}\mathbf{F}dt, t-dt\right),$$

Ainsi, les collisions ajouteront une correction à cette relation et la correction augmentera à mesure que dt augmentera, puis

$$f\left(\mathbf{r},\mathbf{k},t\right) = f\left(\mathbf{r}-\mathbf{v}dt, \mathbf{k}-\frac{1}{\hbar}\mathbf{F}dt, t-dt\right) + \left(\frac{\delta f}{\delta t}\right)_{\text{diff.}} dt,$$

mais si l'on considère seulement le premier terme d'une expansion Taylor

$$f\left(\mathbf{r},\mathbf{k},t\right) \approx f\left(\mathbf{r},\mathbf{k},t-dt\right) - \mathbf{v}dt\cdot\nabla_{\mathbf{r}}f - \frac{1}{\hbar}\mathbf{F}dt\cdot\nabla_{\mathbf{k}}f + \left(\frac{\delta f}{\delta t}\right)_{\text{diff.}} dt.$$

C'est pourquoi

$$\left(\frac{\delta f}{\delta t}\right)_{\text{diff.}} = \frac{f\left(\mathbf{r},\mathbf{k},t\right) - f\left(\mathbf{r},\mathbf{k},t-dt\right)}{dt} + \mathbf{v}\cdot\nabla_{\mathbf{r}}f + \frac{1}{\hbar}\mathbf{F}\cdot\nabla_{\mathbf{k}}f$$

ou[1]

L'équation de transport de Boltzmann

$$\left(\frac{\delta f}{\delta t}\right)_{\text{diff.}} = \frac{\partial f}{\partial t} + \frac{1}{\hbar}\nabla_{\mathbf{k}}\mathcal{E}\left(\mathbf{k}\right)\cdot\nabla_{\mathbf{r}}f + \frac{-e\mathbf{E}}{\hbar}\cdot\nabla_{\mathbf{k}}f. \tag{2}$$

Cette dernière équation est connue sous le nom *d'équation de transport de Boltzmann* [SR.19, SR.20]. Ici, $\left(\frac{\delta f}{\delta t}\right)_{\text{diff.}} dt$ est la probabilité de diffusion dans $(\mathbf{r},\mathbf{k})$ moins la probabilité de diffusion hors de $(\mathbf{r},\mathbf{k})$. En d'autres termes, c'est la variation de la probabilité d'occupation de $(\mathbf{r},\mathbf{k})$ due aux collisions pendant le temps dt.

La diffusion d'un état $|\mathbf{k}\rangle$ (particule incidente) à $|\mathbf{k}'\rangle$ (particule diffusée) à un taux, est donnée par

La règle d'or de Fermi

$$\Gamma_{\mathbf{k}\to\mathbf{k}'} = \frac{2\pi}{\hbar}\left|\left\langle\mathbf{k}'\right|\widehat{V}_{\text{dir.}}\left|\mathbf{k}\right\rangle\right|^2\delta\left(\mathcal{E}_{\mathbf{k}'}-\mathcal{E}_{\mathbf{k}}\right) \equiv W_{\mathbf{k}'\mathbf{k}}. \tag{3}$$

---

[1] Dans un cas plus général, $\mathbf{v} = \frac{1}{\hbar}\nabla_{\mathbf{k}}\mathcal{E}\left(\mathbf{k}\right)$, où $\mathcal{E}$ est l'énergie et $\nabla_{\mathbf{k}}$ est l'opérateur de gradient dans l'espace $\mathbf{k}$: $\nabla_{\mathbf{k}}\mathcal{E} = \partial\mathcal{E}_x/\partial k_x + \partial\mathcal{E}_y/\partial k_y + \partial\mathcal{E}_z/\partial k_y$

Ici, $V_{\text{dir.}}$ est le paysage énergétique potentiel supplémentaire dû aux impuretés (potentiel de défaut), $\delta\left(\mathcal{E}_{\mathbf{k}'} - \mathcal{E}_{\mathbf{k}}\right)$ nous indiquent que l'énergie est conservée et

$$\begin{aligned}
\left\langle \mathbf{k}' \right| \widehat{V}_{\text{dir.}} \left| \mathbf{k} \right\rangle &= \int \phi^{*}_{\mathbf{k}'}(\mathbf{r}) V_{\text{dir.}}(\mathbf{r}) \phi_{\mathbf{k}}(\mathbf{r})\, d^3\mathbf{r} \\
&= \left(\frac{1}{\sqrt{\text{Volume}}} \right)^2 \int e^{-i(\mathbf{k}'-\mathbf{k})\cdot\mathbf{r}}\, V_{\text{dir.}}(\mathbf{x})\, d^3\mathbf{r} \\
&\propto \sum_{\mathbf{R}} e^{-i(\mathbf{k}'-\mathbf{k})\cdot\mathbf{R}} \cdot \left[\int_{\text{cellule unitaire}} e^{-i(\mathbf{k}'-\mathbf{k})\cdot\mathbf{x}}\, V_{\text{dir.}}(\mathbf{r})\, d^3\mathbf{r} \right],
\end{aligned}$$

où le Volume désigne l'ensemble de l'espace, $\phi_{\mathbf{k}}$ est la fonction d'onde et $\mathbf{R}$ est le réseau de Bravais. Cela implique donc que pour la diffusion classique et quantique, l'amplitude diffusée est le produit de deux termes

$$\text{Amplitude} \propto \sum_{\mathbf{G}} \delta\left(\mathbf{k}' - \mathbf{k} - \mathbf{G}\right) \cdot \left[\int_{\text{cellule unitaire}} e^{-i(\mathbf{k}'-\mathbf{k})\cdot\mathbf{r}}\, V(\mathbf{r})\, d^3\mathbf{r} \right].$$

L'amplitude diffusée ne dépend donc que du réseau, puisque $\mathbf{G}$ est le réseau réciproque, et le facteur de structure $S\left(\mathbf{k}' - \mathbf{k}\right)$. Par conséquent, $W_{\mathbf{k}'\mathbf{k}}$ pourrait être considéré comme un taux de diffusion provenant d'autres sources comme les phonons, par exemple [SR.19, SR.20].

Parce que $W_{\mathbf{k}'\mathbf{k}}$ est une expression générale qui nous aide à déterminer le taux de diffusion des phonons, nous devons déterminer la variation de la probabilité d'occuper une position et du vecteur d'onde due aux collisions pendant un certain temps dt. D'une part, la probabilité de diffusion à partir de $\mathbf{k}$ dans le temps dt peut être définie comme:

$$\mathcal{P}_{\text{out}} = f\left(\mathbf{r}, \mathbf{k}, t\right) \sum_{\mathbf{k}'} W_{\mathbf{k}',\mathbf{k}}\, dt \left[1 - f\left(\mathbf{r}, \mathbf{k}', t\right)\right],$$

où $f\left(\mathbf{r}, \mathbf{k}, t\right)$ est la probabilité que $\mathbf{k}$ soit occupé et $1 - f\left(\mathbf{r}, \mathbf{k}', t\right)$ est la probabilité que $\mathbf{k}'$ soit inoccupé. D'autre part, la probabilité de dispersion dans $\mathbf{k}$ est, de la même manière:

$$\mathcal{P}_{\text{in}} = \left[1 - f\left(\mathbf{r}, \mathbf{k}, t\right)\right] \sum_{\mathbf{k}'} W_{\mathbf{k},\mathbf{k}'}\, dt f\left(\mathbf{r}, \mathbf{k}', t\right),$$

aussi

$$\begin{aligned}
\left(\frac{\delta f}{\delta t} \right)_{\text{diff.}} &= \frac{1}{dt} \left(\mathcal{P}_{\text{in}} - \mathcal{P}_{\text{out}}\right) \\
&= \sum_{\mathbf{k}'} \left[1 - f\left(\mathbf{r}, \mathbf{k}, t\right)\right] W_{\mathbf{k},\mathbf{k}'} f\left(\mathbf{r}, \mathbf{k}', t\right) - f\left(\mathbf{r}, \mathbf{k}, t\right) W_{\mathbf{k}',\mathbf{k}} \left[1 - f\left(\mathbf{r}, \mathbf{k}', t\right)\right] \\
&= \frac{V}{(2\pi)^3} \int d^3\mathbf{k}' \left\{ \left[1 - f\left(\mathbf{r}, \mathbf{k}, t\right)\right] W_{\mathbf{k},\mathbf{k}'} f\left(\mathbf{r}, \mathbf{k}', t\right) - f\left(\mathbf{r}, \mathbf{k}, t\right) W_{\mathbf{k}',\mathbf{k}} \left[1 - f\left(\mathbf{r}, \mathbf{k}', t\right)\right] \right\},
\end{aligned}$$

où V est le volume total du cristal [SR.21]. Cette dernière intégrale de collision représente le côté gauche de l'équation de transport de Boltzmann [voir éq. (2)] et est la partie importante pour le transport des porteurs car elle décrit la réponse ou la contribution des forces de collision à courte distance qui donnent le *friction* pour le transport des porteurs. Cependant, même si nous connaissons $W_{\mathbf{k}',\mathbf{k}}$, cela a transformé l'équation de Boltzmann en une équation integro–différentielle compliquée pour $f\left(\mathbf{r}, \mathbf{k}, t\right)$. Par conséquent, afin de résoudre numériquement cette équation, il est nécessaire d'utiliser une méthode de calcul. Dans ce travail, nous avons réalisé l'étude numérique en utilisant la méthode de Monte–Carlo.

0.2.2 Solution numérique de l'équation de Boltzmann: approche d'ensemble Monte–Carlo

Pour modéliser la dynamique des porteurs transitoires sous l'influence d'un champ électrique appliqué et des mécanismes de diffusion typiques, nous avons utilisé une approche numérique complète: le modèle de Monte–Carlo d'ensemble. Pour résoudre l'équation de transport de Boltzmann, la méthode de Monte–Carlo considère que le processus de diffusion (diffusion acoustique, de Coulomb et de phonon optique polaire, diffusion intra– et inter–vallées, etc.) et les états finaux sont sélectionnés de manière stochastique [SR.22, SR.23].

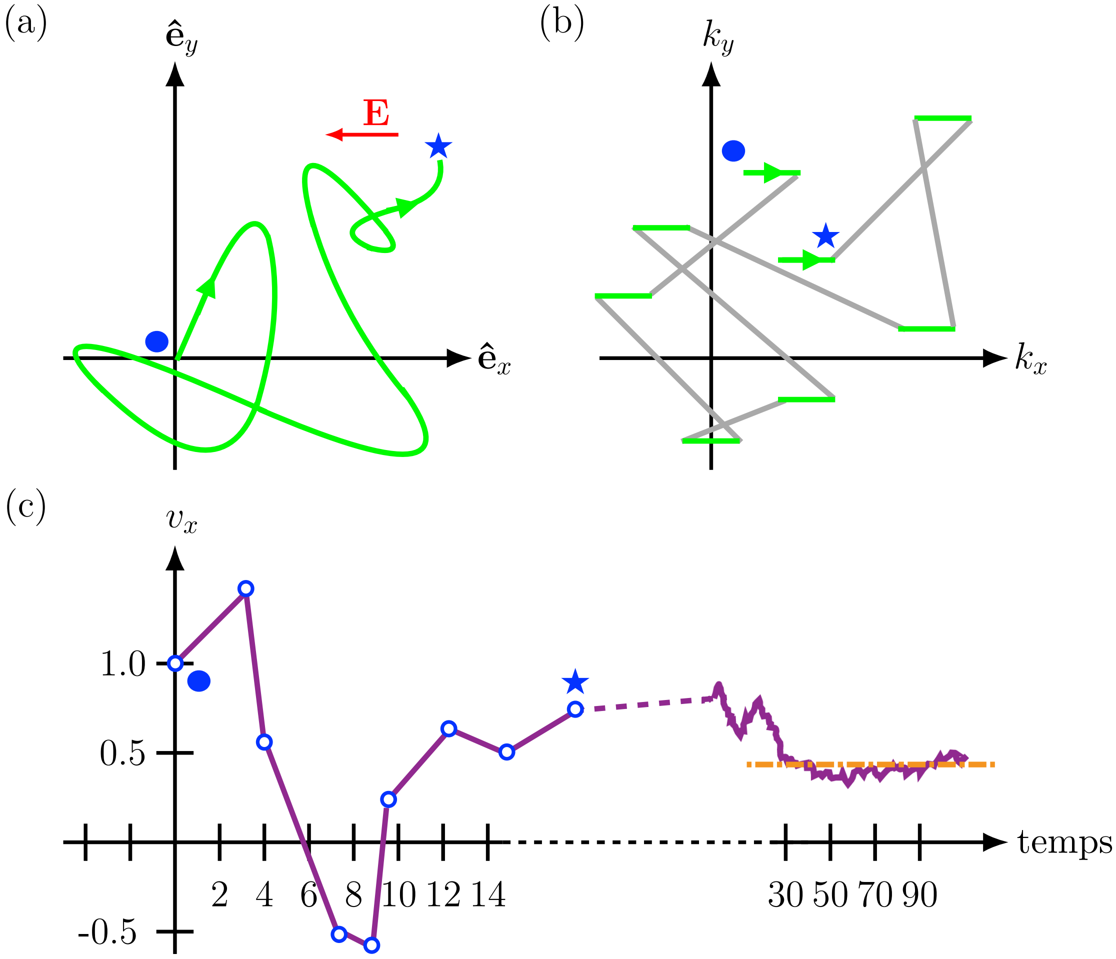

Figure 6: Schéma de la méthode de Monte-Carlo ; par souci de simplicité, la méthode est représentée en deux dimensions. a) Simulation du trajet des électrons d'échantillonnage sous l'influence d'un champ électrique externe E orienté dans la direction x. (b) Même trajectoire qu'en (a) mais dans l'espace de momentum. (c) Vitesse moyenne du porteur sur toutes les étapes à partir de l'étape 1 jusqu'au numéro de l'étape en cours en fonction du temps de simulation. Les icônes spéciales dans les trois figures indiquent le point de départ ($\bullet$) et le point d'arrivée ($\star$) de la trajectoire [SR.26].

La figure 6 montre la base de la méthode Monte–Carlo. La figure 6(a) montre la simulation du trajet des électrons par échantillonnage sous l'influence d'un champ électrique externe **E** orienté dans la direction x. Les huit fragments de paraboles correspondent aux huit trajets libres. La même trajectoire de l'électron mais dans l'espace du momentum, est montrée dans la figure 6(b). Les segments lourds (lignes vertes) sont dus à l'effet du champ pendant les vols libres, tandis que les lignes claires (lignes grises) représentent les changements de moment dans chaque processus de diffusion [SR.26]. La vitesse moyenne des porteurs à un point n–th sur tous les trajets $(n-1)$ précédents, est calculée sur la figure 6(c). En effectuant une simulation très longue, nous pouvons obtenir une vitesse de dérive précise, telle que représentée dans la figure 6(c) par les lignes horizontales orange pointillées.

Dans la méthode de Monte–Carlo, nous supposons que la dynamique semi–classique du mouvement des particules consiste en la génération de temps de vol libre aléatoires par des événements de diffusion instantanés et sans mémoire, qui modifient l'énergie et l'élan de la particule après chaque événement de diffusion. En outre, la probabilité de diffusion d'un électron dans un court intervalle de temps dt s'écrit $\Gamma\left[\mathbf{k}\left(t\right)\right]dt$, où $\Gamma\left[\mathbf{k}\left(t\right)\right]$ est le taux de diffusion d'un électron ou d'un trou d'onde–vecteur **k** par unité de temps [SR.22, SR.27]. Pour effectuer une simulation transitoire, il est essentiel de disposer d'un ensemble synchrone de particules, dans lequel l'algorithme doit être répété pour chaque particule de l'ensemble qui représente le système d'intérêt, jusqu'à ce que la simulation soit terminée. La figure 7 illustre le modèle de croquis du vol libre dispersé. Dans l'axe des temps de la durée du vol libre, N est le nombre total de particules dans la simulation, tandis que dans l'axe des temps d'échantillonnage, t_s est le temps total de la simulation et Δt représente le pas de temps auquel le mouvement de toutes les particules est synchronisé [SR.23, SR.34]. De plus, t_i est le temps de vol libre pour la i–ième particule et chaque croix rouge illustrée dans la figure 7 représente une collision ou un événement de diffusion aléatoire et instantané qui peut ou non se produire pendant un pas de temps.

Figure 7: Esquisse de vol libre dispersé où le mouvement de toutes les particules N est synchronisé à Δt. Les croix rouges (×) indiquent chaque événement de dispersion.

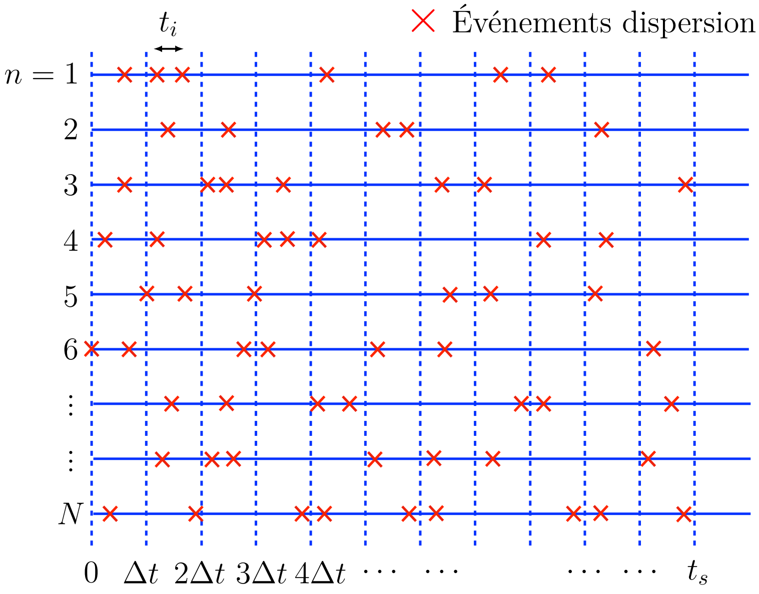

En résumé, dans l'approche Monte–Carlo d'ensemble, chaque porteur est simulé jusqu'à la fin du pas de temps, puis la particule suivante de l'ensemble est traitée. Le mouvement de chaque particule dans l'ensemble est simulé indépendamment des autres particules à chaque pas de temps et, en même temps, les effets non linéaires et le mécanisme de diffusion sont mis à jour.

0.3 Résultats des effets optiques non linéaires THz dans le semi–conducteur dopé n–In$_{0.57}$Ga$_{0.43}$As

Plusieurs études ont montré les effets de la génération d'harmoniques THz d'ordre élevé [SR.14 – SR.17, SR.36 – SR.38] et de la génération de bande latérale d'ordre élevé (HSG) [SR.16, SR.17], en utilisant des impulsions THz intenses à plusieurs cycles transmises à travers divers matériaux. Ces matériaux comprennent le graphène (expliqué par l'interaction entre le mouvement interbande et intrabande des porteurs et la dynamique des fermions chauds de Dirac) [SR.14, SR.36, SR.37], des cristaux massifs, tels que: le séléniure de gallium (interprété par des oscillations dynamiques de Bloch) [SR.15, SR.38], et le diséléniure de tungstène (modélisé par des collisions électron-trou pilotées par THZ) [SR.16, SR.17]. En utilisant une impulsion d'excitation proche de l'infrarouge de 100 femtosecondes et une impulsion THz de haute intensité avec des champs électriques de crête de l'ordre du MV/cm, Langer *et al.* ont observé dans le WSe$_2$ que les électrons et les trous en recollision émettent de la lumière via de multiples HSG [SR.16, SR.17].

Dans le mémoire présenté, nous effectuons des études détaillées sur la dynamique des porteurs transitoires et les effets THz non linéaires induits par une impulsion THz intense de plusieurs cycles dans un semi–conducteur dopé n–In$_{0.57}$Ga$_{0.43}$As. Nous clarifions, pour la première fois, le mécanisme qui aboutit à la génération de composants de basse fréquence (LFC) et de composants de haute fréquence (HFC), qui sont purement liés aux effets intra–vallée, reflétant la non-parabolicité de la bande de conduction. En particulier, pour expliquer et comprendre la génération de LFC et HFC présentés pour différentes fréquences dans les spectres d'amplitude transmis, nous appliquons le formalisme de la transformée de Gábor pour révéler l'émission temporelle de ces composantes à différentes fréquences [SR39 – SR.41]. Cependant, des LFC et HFC similaires, à la fréquence fondamentale, ont été observés dans des rapports récents sur les interactions THz–matière intenses, telles que celles détectées dans les spectres d'harmoniques d'ordre élevé du graphène [SR.14], qui sont qualitativement en bon accord avec nos simulations. Dans les deux matériaux, la réponse non linéaire de la masse effective des porteurs devient très forte avec des champs électriques THz relativement faibles. En outre, nous détaillons les différents mécanismes responsables de l'émission d'harmoniques d'ordre élevé pour les impulsions à fréquence THz et haute fréquence (0.2 THz – 1.5 THz) et avec des champs électriques de crête incidents allant de 100 kV/cm à 500 kV/cm.

Figure 8: Incidence et transmission normales du champ électrique THz à travers un film conducteur mince déposé sur un substrat diélectrique : configuration substrat / film mince / air.

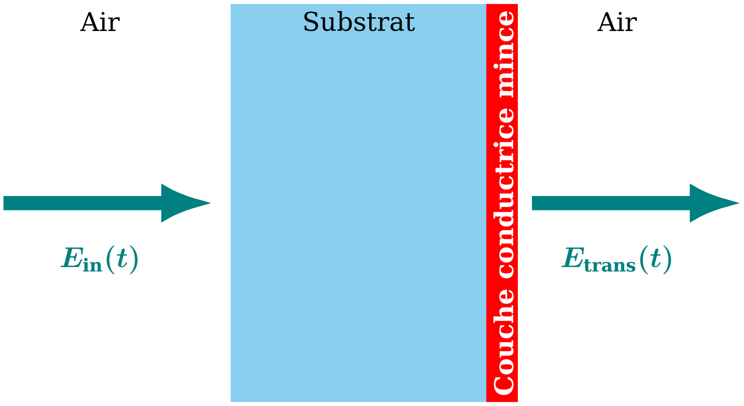

Pour comprendre la dynamique des porteurs non–linéaires du semiconducteur dopé n–In$_{0.57}$Ga$_{0.43}$As induit par des impulsions multi–cycles, nous avons effectué une analyse théorique dans le domaine temporel en utilisant l'équation des couches minces [SR.4, SR.11, SR.13, SR.37], en considérant que l'échantillon pourrait être idéalisé comme une mince feuille conductrice d'épaisseur d sur un substrat isolant à indice de réfraction N [SR.11]. Dans notre étude, l'échantillon est une couche de 500–nm–d'épaisseur n–type $\mathrm{In_{0.57}Ga_{0.43}As}$ (100) avec une concentration des electrons de 2×10^{18} cm^{-3} [SR.13]. Si l'impulsion THz irradie l'échantillon du côté du substrat InP (configuration: substrat / couche mince / air, voir la figure 8) [SR.42], l'équation de la couche mince est donnée par l'expression

L'équation des films minces

$$E_{\text{trans}}(t) = \frac{1}{Y_0 + Y_S}\left[\frac{4Y_S}{N+1}E_{\text{in}}(t) - J(t)\,d\right]. \tag{4}$$

Ici, $E_{\text{trans.}}(t)$ et $E_{\text{in.}}(t)$ sont respectivement les champs THz transmis et incident, $Y_0 = (377\,\Omega)^{-1}$ est l'admittance en espace libre, et $Y_S = NY_0$ est l'admittance du substrat, où $N = 3.1$ est l'indice de réfraction de l'InP aux fréquences THz [SR.4]. Nous mettons en œuvre une approche analytique d'ensemble de bandes Monte–Carlo pour résoudre l'équation de transport de Boltzmann [SR.22, SR.33, SR.35, SR.43] et pour modéliser la dynamique transitoire des porteurs de l'échantillon. Pour détailler les différents effets de diffusion dans nos simulations, nous considérons le mécanisme de diffusion typique dans un semi–conducteur composé tel que la diffusion acoustique, de Coulomb et de phonon optique polaire, ainsi que la diffusion intra– et inter–vallées [SR.22, SR.23]. Grâce à ces simulations, nous obtenons la dynamique des porteurs dans les vallées Γ, L et X de la bande de conduction et la densité de courant $J(t)$ a été directement déterminée par la vitesse de dérive moyenne [SR37, SR44 – SR.46].

Nous avons d'abord effectué des simulations sur les effets non–linéaires induits par un rayonnement THz intense à plusieurs cycles dans un échantillon d'$\mathrm{In_{0.57}Ga_{0.43}As}$. Dans les simulations, nous considérons une température de 300 K et utilisons les constantes physiques de l'échantillon d'$\mathrm{In_{0.57}Ga_{0.43}As}$ rapporté par Long *et al.* et Razzari *et al.* [SR.12, SR.33].

0.3.1 Impulsions de THz à fréquence relativement basse et haute

La figure 9 montre la forme d'onde THz incidente et transmise pour les impulsions THz avec des fréquences centrales de 0.2 THz, 0.4 THz, 1.0 THz et 1.5 THz. Les champs électriques crête incidents utilisés ici sont de 350 kV/cm pour les impulsions de 0,2 THz et 0,4 THz, 114 kV/cm pour l'impulsion de 1.0 THz et 125 kV/cm pour l'impulsion de 1.5 THz. Pour les impulsions de 0.2 THz et 0.4 THz, nous avons constaté que la densité de courant déformée présente une troncature nette [voir les figures 9(a) et 9(b)]. En revanche, pour les impulsions THz de 1.0 et 1.5 THz, il est difficile d'observer des troncatures de courant nettes plus rapides que la durée du demi–cycle de la forme d'onde THz incidente initiale [voir les figures 9(c) et 9(d)].

Pour les impulsions multicycles à fréquence relativement basse et les champs crête incidents élevés, la conséquence directe des phases de courant déformées avec les champs THz est la netteté des pics de haute harmonique (HH) dans les spectres d'intensité transmis (jusqu'à la 11$^{\text{ème}}$ et 7$^{\text{ème}}$ harmonique pour les impulsions de 0.2 THz et 0.4 THz, respectivement) [voir les figures 10(a) et 10(b)]. En revanche, pour les champs de crête à fréquence relativement élevée et de faible intensité, les changements de fréquence ne sont pas aussi évidents à observer en raison de l'absence de troncatures claires du courant. Cependant, nous pouvons encore observer la génération d'harmoniques d'ordre élevé (HHG) dans les spectres d'intensité (jusqu'au 5$^{\text{ème}}$ ordre lorsqu'ils sont pompés par les impulsions de 1.0 THz et jusqu'au 3$^{\text{ème}}$ ordre lorsqu'ils sont pompés par des impulsions de 1.5 THz) [voir les figures 10(c) et 10(d)]. En outre, nous pouvons également observer quelques petites crêtes qui se situent à 0.3 THz et 1.7 THz lorsque l'échantillon est pompé par des impulsions de 1.0 THz. Ces nouvelles fréquences, qui ne correspondent à aucun ordre d'harmonique, sont la composante basse fréquence (LFC) et la composante haute fréquence (HFC).

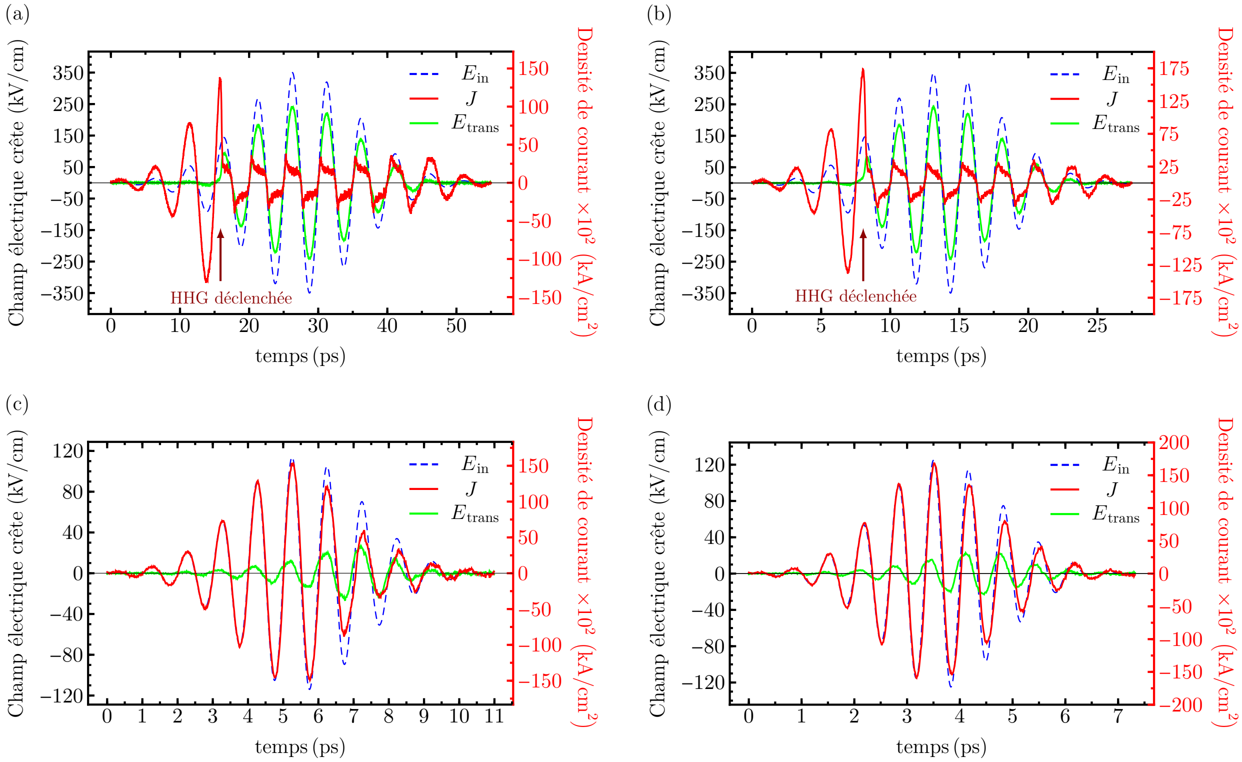

Figure 9: Densité de courant (ligne rouge continue) et forme d'onde THz transmise (ligne verte continue) générée par une impulsion THz à plusieurs cycles (ligne bleue pointillée) centrée sur (a) 0.2 THz, (b) 0.4 THz, (c) 1.0 THz et (d) 1.5 THz. Les champs de crête incidents utilisés ici sont de 350 kV/cm pour les impulsions de (a) 0.2 THz et (b) 0.4 THz, (c) 114 kV/cm pour l'impulsion de 1.0 THz et (d) 125 kV/cm pour l'impulsion de 1.5 THz.

Pour une onde carrée idéale, l'ordre d'harmonique de la transformée de Fourier s'étendrait à l'infini. Dans notre cas, l'intensité et l'ordre des HHG dépendent de la modulation du photocourant, plus les troncatures du photocourant sont fortes et rapides, plus l'ordre des HHs est élevé. En conséquence, le HHG est plus facile à voir en utilisant une source de fréquence relativement basse, ce qui entraîne un meilleur contraste de troncature temporelle dans la densité de courant [voir les figures 10(a) et 10(b)]. De plus, pour des impulsions THz, dite à haute fréquence, haute fréquence et à des intensités de champ similaires, il est difficile d'obtenir des troncatures plus nettes, et donc les harmoniques [comme la 5$^{\text{ème}}$ harmonique de l'impulsion de 1.0 THz sur la figure 10(c)] sont moins évidentes. Par conséquent, dans ces conditions, la génération de LFC et de HFC est plus claire dans les spectres d'amplitude transmis [voir les figures 10(c) et 10(d)], mais lorsque nous augmentons l'intensité du champ électrique, les harmoniques sont nettement moins intenses et beaucoup plus difficiles à observer [voir les figures 10(c) et 10(d)], tandis que les LFC et les HFC disparaissent. Dans ce cas, la population de porteurs des vallées X et L augmente rapidement, mais la gamme dynamique temporelle dans laquelle la diffusion intra– et inter–vallées peut se produire est inférieure à celle induite par les impulsions THz de basse fréquence. Ainsi, même si l'intensité de l'impulsion de la pompe est augmentée, les diffusions intra– et inter–vallées réduiront et les effets non linéaires commenceront à devenir complexes.

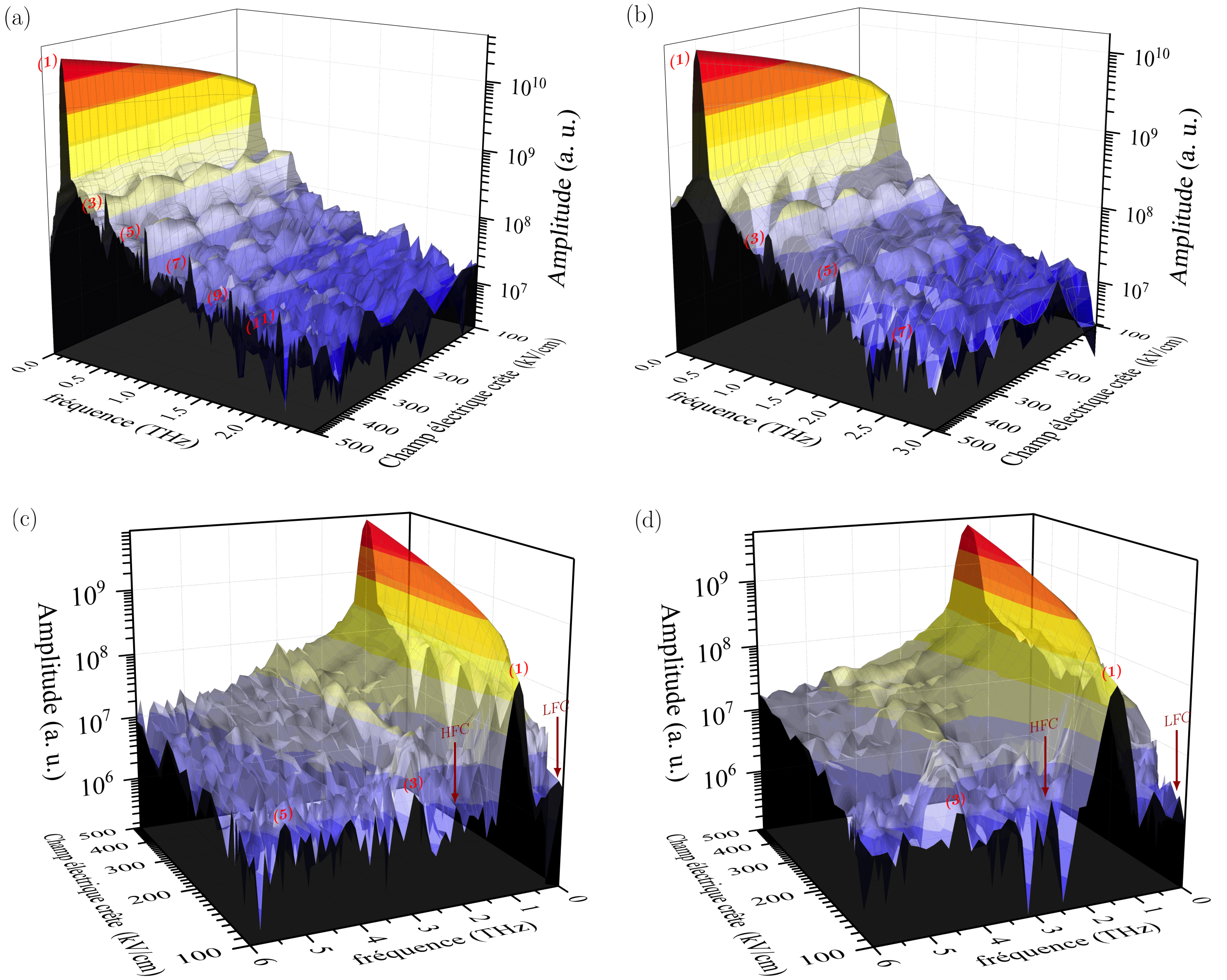

Figure 10: Simulations de HHG, LFC et HFC. Simulations de la génération d'harmoniques d'ordre supérieur dans l'échantillon d'$In_{0.57}Ga_{0.43}As$, en utilisant l'approche de Monte–Carlo de l'ensemble de bandes analytiques pour résoudre l'équation de transport de Boltzmann: spectres d'amplitude des formes d'onde THz transmises par l'$In_{0.57}Ga_{0.43}As$ échantillon en fonction des champs électriques de crête de THz, pour des fréquences fondamentales de (a) 0.2 THz, (b) 0.4 THz, (c) 1.0 THz et (d) 1.5 THz.

0.3.2 Analyse temps–fréquence pour les impulsions THz à basse fréquence

Pour mesurer avec précision dans les domaines temporel et fréquentiel, nous avons effectué une analyse temps-fréquence, qui nous permet de capturer l'ensemble du contenu temps–fréquence des formes d'onde multi–cycles transmises et de générer en même temps un spectrogramme [SR.39, SR.40]. Pour cela, nous avons appliqué le formalisme de la transformée de Gábor aux formes d'onde multi–cycles transmises pour expliquer et comprendre les HHG, LFC et HFC présentés à différentes fréquences des spectres [SR.41].

Tout d’abord, pour mieux comprendre le HHG à partir d’impulsions THz multicycles à fréquence basse (0.2 THz) et avec un champ crête incident élevé (350 kV/cm), nous analysons les populations de porteurs dans les vallées Γ, L et X. La figure 11(a) montre une réduction drastique de la population de porteurs dans la vallée Γ autour de 16 ps. À ce moment, en raison du champ d’incidence élevé, l’accélération ponderomotive est suffisamment forte pour que les porteurs acquièrent suffisamment d’énergie cinétique pour subir efficacement la diffusion intermittente des vallées Γ vers les vallées L et X [SR.13]. La HHG est principalement causée par les transitions intermittentes des porteurs de la vallée Γ vers les vallées L et X, et aussi des vallées L vers les vallées X et vice versa. Ce processus de diffusion par intervalles entre la vallée Γ et les vallées du satellite est répété ou poursuivi tout au long de l’impulsion THz.

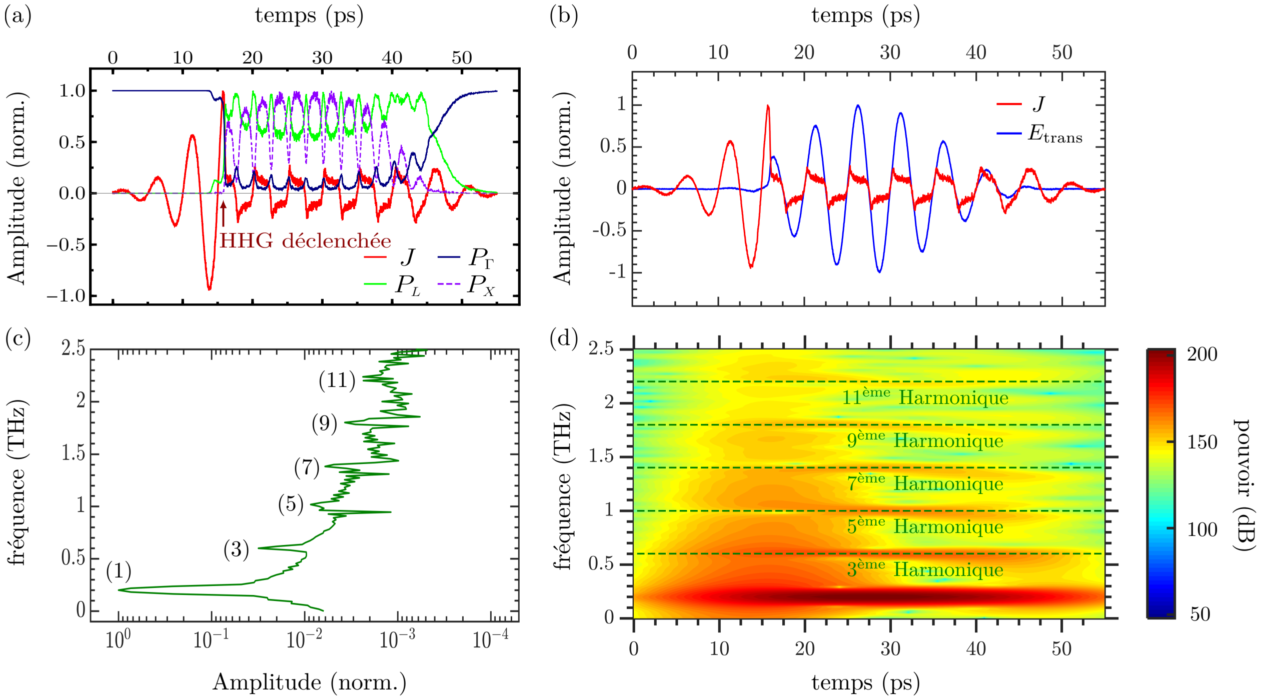

Figure 11: Analyse temps–fréquence, ou transformée de Gábor, avec une taille de fenêtre temporelle égale à $a = 0.01$, pour les champs crêtes incidents à 350 kV/cm pour une impulsion de 0.2 THz. (a) Densité de courant temporelle normalisée (ligne rouge continue), et populations de porteurs dans les vallées Γ (ligne continue bleu foncé), L (ligne continue lime) et X (ligne violette interrompue). (b) Densité de courant (ligne rouge continue) et impulsion THz multicycle transmise (ligne bleue continue). (c) Les spectres d’amplitude transmis correspondants. (d) Les HHs (lignes vertes brisées) sont indiqués pendant la durée de l’impulsion.

En outre, l’analyse temps–fréquence montre que la troisième harmonique est émise autour de l’intensité la plus élevée et que la cinquième harmonique et les harmoniques supérieures n’apparaissent qu’à un certain moment de l’impulsion THz et avec une intensité plus faible [voir la figure 11(d)] car, comme nous réduisons fortement la durée des phénomènes de recombinaison, seules les hautes fréquences proches de la fréquence de coupure $\omega_{\text{cut}}^{\text{HHG}}$ sont augmentées [SR.47].

0.3.3 Analyse temps–fréquence pour les impulsions THz à haute fréquence

Ensuite, nous calculons la population de porteurs pour l’impulsion de 1.0 THz avec un champ crête incident de 114 kV/cm. Jusqu’au pic du quatrième cycle de la densité de courant [voir la figure

12(a)], les porteurs restent dans la vallée de Γ, mais après quelques picosecondes, les électrons gagnent suffisamment d'énergie pour être diffusés de la vallée de Γ vers les vallées satellites plus élevées. Cependant, on peut clairement voir que l'intensité maximale du troisième harmonique se produit en même temps que l'intensité maximale de l'impulsion THz, précisément au moment où les populations de porteurs des vallées L et X commencent à augmenter [voir la flèche rouge de la figure 12(a)]. Cependant, les LFC (0.3 THz) et les HFC (1.7 THz), observe une émission considérablement plus forte que les pics de HH quelques picosecondes après le pic du quatrième cycle de la densité de courant [voir la figure 12(d)].

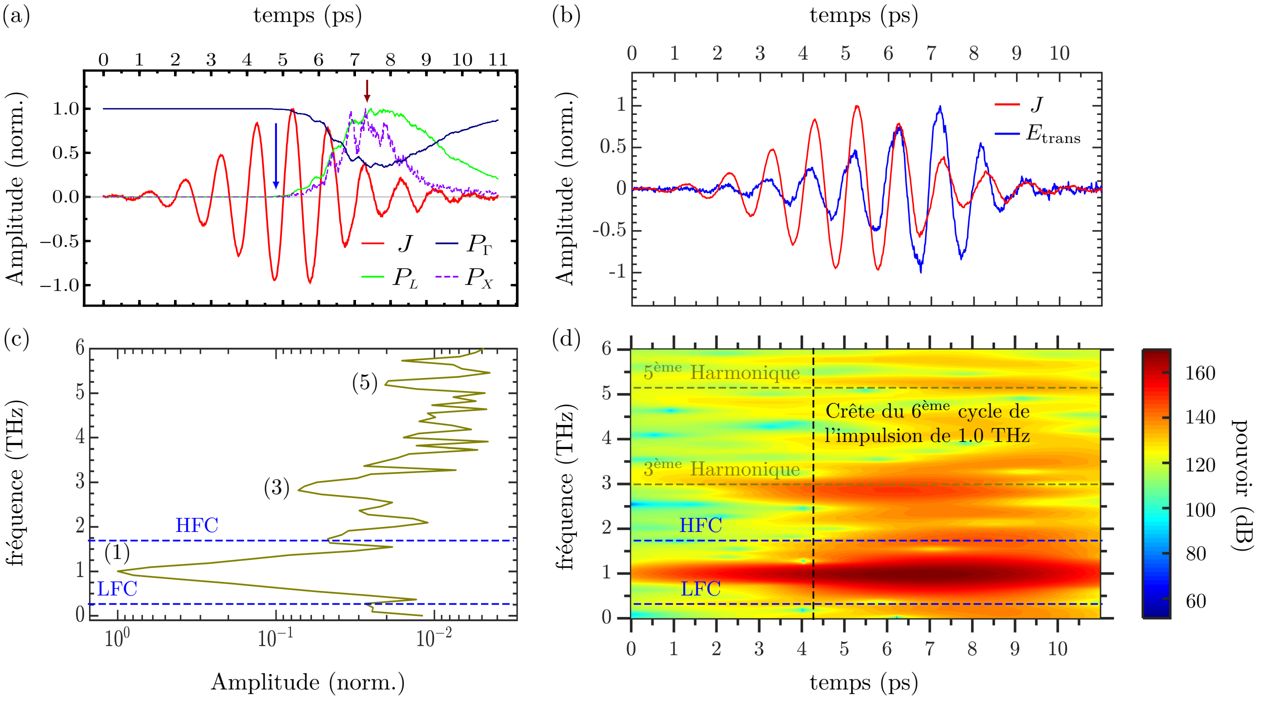

Figure 12: Analyse temps–fréquence, ou transformée de Gábor, avec une taille de fenêtre temporelle égale à $a = 0.18$, pour les champs crêtes incidents à 114 kV/cm pour une impulsion de 1.0 THz. (a) Densité de courant temporelle normalisée (ligne rouge continue), et populations de porteurs dans les vallées Γ (ligne continue bleu foncé), L (ligne continue lime) et X (ligne violette interrompue). (b) Densité de courant (ligne rouge continue) et impulsion THz multicycle transmise (ligne bleue continue). (c) Les spectres d'amplitude transmis correspondants. (d) HH (lignes vert olive brisées)est émis tout au long de l'impulsion THz et pour les LFC et HFC, l'émission est observée après le moment où le pic du quatrième cycle de l'impulsion de 1.0 THz arrive, alors que leur émission est beaucoup plus faible pour les temps précédents.

Nous effectuons des calculs supplémentaires pour le cas d'une fréquence THz relativement élevée et d'un champ crête incident faible. Pour un champ électrique crête de 100 kV/cm, (i) la variation de la population de porteur dans la vallée de Γ est faible, (ii) des composantes à basse fréquence apparaissent dans les spectres d'amplitude transmis, et (iii) des harmoniques d'ordre élevé apparaissent mais avec une très faible intensité. Lorsque nous augmentons le champ électrique crête, les composantes haute fréquence deviennent évidentes lorsque les champs électriques de crête varient de 110 à 125 kV/cm. L'effet non linéaire commence à se complexifier à partir de 140 kV/cm parce que la population des porteurs de la vallée X et L commence à augmenter rapidement pendant la durée de l'impulsion THz, et le temps de diffusion est soudainement réduit. Ainsi, pour le champ de crête incident plus élevé, le HHG a une faible intensité, et le LFC et le HFC disparaissent. Ces résultats montrent une forte corrélation entre la population de porteurs dans la vallée Γ et l'émission non linéaire de THz dans les composantes basse et haute fréquence. Cela confirme que pour qu'il y ait des effets THz non–linéaires, il faut une population suffisante de porteur dans la vallée Γ. En outre, l'émission de LFC et de HFC ne couvre pas toute la durée de l'impulsion de THz pour des champs crête entre 110–125 kV/cm, car le fait d'avoir les deux effets en même temps peut diminuer l'efficacité des deux processus.

0.3.4 Masse effective moyenne des porteurs

Ensuite, nous appliquons la transformée de Fourier rapide (FFT) à la masse effective moyenne des porteurs calculée $\langle m_i^* \rangle$ pour chaque $i = \Gamma$, L et X vallées. La figure 13 montre les composantes de fréquence auxquelles $\langle m_i^* \rangle$ varie en fonction du temps. Lorsque le champ électrique de l'impulsion THz est faible, $\langle m_i^* \rangle$ est constant, et donc les effets non linéaires de THz ne sont pas observés dans l'impulsion THz transmise. Dans ce cas, le spectre d'amplitude de $\langle m_i^* \rangle$ sera une fonction étroite centrée sur 0 THz. Cependant, lorsque le champ de THz augmente, on trouve plusieurs pics apparaissant dans les spectres d'amplitude de $\langle m_i^* \rangle$ [voir la figure 13]. Les plus plus évidents sont ceux qui entraînent la génération d'harmonique de l'impulsion THz incidente. Par exemple, dans la figure 13(b), les pics à ~0.4 THz, ~0.8 THz, ~1.2 THz, ~1.6 THz, ~2.0 THz et ~2.4 THz donne les harmoniques impairs de l'impulsion de 0.2 THz et le pic qui apparaît à ~2 THz dans la figure 13(a), donne la troisième harmonique de l'impulsion de 1.0 THz. Cette modulation en $\langle m_i^* \rangle$ donne des modulations en $J(t)$, générant ainsi les harmoniques par diffusion inter–vallée. Dans des conditions de champ faible, avant qu'un événement inélastique (*i.e.* effets inter–vallée) ne survienne, de nombreux événements de diffusion élastique (*i.e.* effets intra–vallée) se produisent auparavant [SR.21].

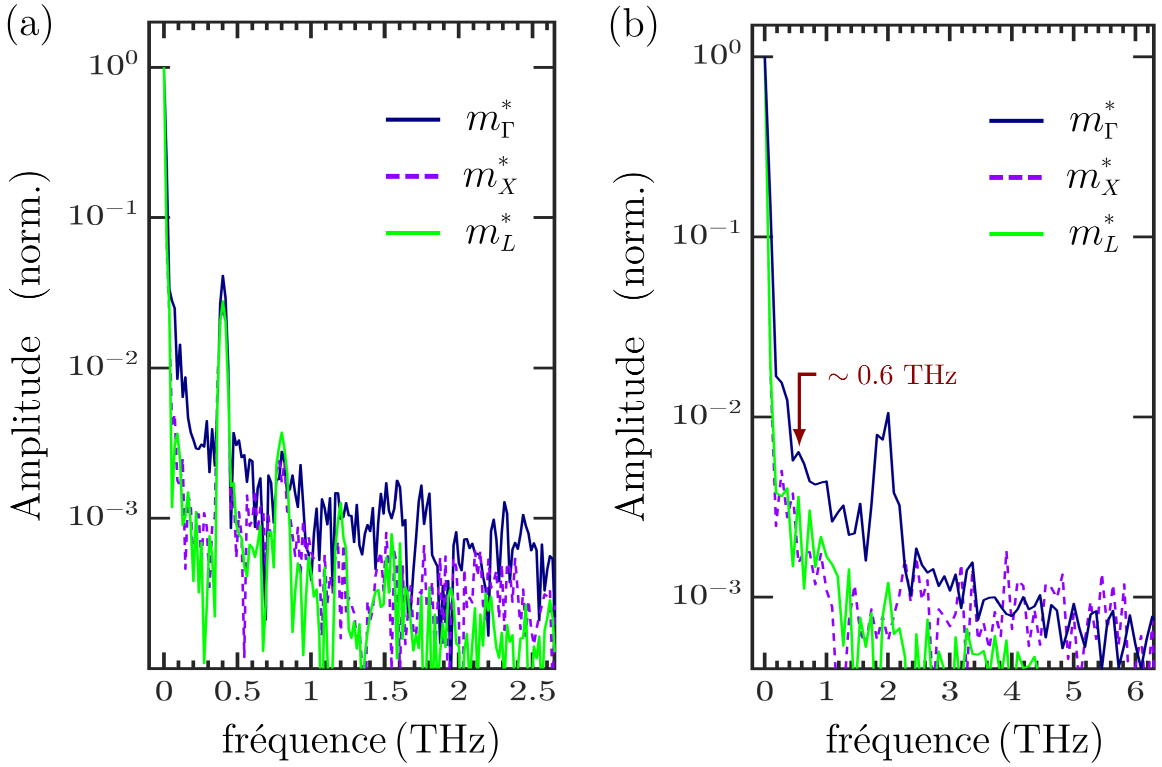

Figure 13: Spectres d'amplitude de la masse effective de chaque porteuse moyenne pour les champs de crête incidents à (a) 350 kV/cm pour 0.2 THz et (b) 114 kV/cm pour 1.0 THz.

On voit aussi dans les spectres d'amplitude de $\langle m_i^* \rangle$ d'autres pics, comme celui de la figure 3.12(b) centré à ~0.6 THz. Ce pic entraîne également la modulation de $J(t)$, ce qui donne lieu aux deux pics de la figure 12(c), l'un centré à ~1.6 THz (en ce qui concerne le HFC), et l'autre centré à ~0.4 THz (en ce qui concerne le LFC). Nous constatons que puisque ces deux pics sont larges, et en raison de la complexité de l'émission et des structures temporelles, les fréquences centrales du HFC et du LFC ne correspondent pas parfaitement. Il est important de noter que si les harmoniques d'ordre élevé de THz sont générées par des effets d'intervalle et d'intra–vallée, les LFC et HFC sont des effets purement intra–vallée, reflétant la non–parabolicité de la bande de conduction.

0.4 Conclusion

Nos résultats montrent que, pour des impulsions THz à fréquences relativement basses et à cycles multiples et des champs crêtes incidents élevés, les porteurs sont accélérés à une énergie moyenne élevée et la troncature de la densité de courant est d'abord obtenue (conduisant à des HHG discrètes). La génération de LFC et de HFC qui apparaissent dans les spectres d'amplitude transmis est due à des porteurs dans la vallée de Γ accélérés à des énergies élevées, diminuant ainsi leur mobilité, ce qui fait que le courant généré oscille à des fréquences plus basses et plus élevées. Cet effet disparaît à des intensités de THz plus élevées puisque les porteurs sont rapidement diffusés dans les vallées adjacentes [voir les figures 10(c) et 10(d)].

En outre, pour les impulsions à haute fréquence et champs faibles, la diffusion intermittente ne produit pas d'harmoniques nettes en raison de la petite plage dynamique temporelle. En outre, la densité de courant sera importante dans ce cas, ce qui peut entraîner un champ émis énorme le long de toute la forme d'onde THz. Comme les LFC et les HFC sont induits par la diffusion intra–vallée, elles sont également censés être générées avec des impulsions de pompe à basse fréquence THz. Cependant, l'efficacité relative de ce processus, lorsque l'échantillon d'InGaAs est pompé à 0.2 et 0.4 THz, est très faible du fait que le principal mécanisme de diffusion, comme nous l'avons observé dans nos résultats, est la diffusion intermittente qui est responsable de la génération de HH. Nous pensons que c'est la raison pour laquelle nous n'observons pas clairement les pics de LFC et de HFC dans nos spectres pour les impulsions THz à plusieurs cycles centrées à 0.2 et 0.4 THz.

De plus, en utilisant la transformée de Gábor, nous avons clarifié le temps d'émission des photons à différentes fréquences, permettant une meilleure compréhension de la dynamique des porteurs. Enfin, ce travail sert de guide pour les expériences utilisant d'autres semi–conducteurs dopés possibles, ainsi que le graphène [SR.14]. De plus, nos résultats montrent que la génération de LFC et de HFC est possible dans l'InGaAs, mais comme ces composantes sont beaucoup plus faibles que l'impulsion principale THz, elles nécessiteront des mesures avec un rapport signal–à–bruit plus élevé pour les identifier.

Références

[SR.1] Lee, Y. S. *Principles of Terahertz Science and Technology.* (Springer Science Business Media, New York), 1st edition (2009).

[SR.2] Zhang, X. C. and Xu, J. *Introduction to THz Wave Photonics.* (Springer, New York), 1st edition (2011).

[SR.3] Laboratory of Terahertz Spectroscopy, Prague. `https://lts.fzu.cz/en/intro.php.` (2012). [Online; Accessed: 08/01/2021].

[SR.4] Blanchard, F., Golde, D., Su, F. H., Razzari, L., Sharma, G., Morandotti, R., Ozaki, T., Reid, M., Kira, M., Koch, S. W., and Hegmann, F. A. *Phys. Rev. Lett.* **107**, 107401 (2011).

[SR.5] Hafez, H. A., Chai, X., Ibrahim, A., Mondal, S., Férachou, D., Ropagnol, X., and Ozaki, T. *J. Opt.* **18**, 093004 (2016).

[SR.6] Stone, M. R., Naftaly, M., Miles, R. E., Fletcher, J. R., and Steenson, D. P. *IEEE Trans. Microw. Theory Tech.* **52**, 2420–2429 (2004).

[SR.7] Wu, Q. and Zhang, X. C. *Appl. Phys. Lett.* **67**, 3523–3525 (1995).

[SR.8] Martin, C. A., Lovberg, J. A., Dean, W. H., and Ibrahim, E. in *Passive Millimeter–Wave Imaging Technology X* eds. Appleby, R. and Wikner, D. A. (International Society for Optics and Photonics, SPIE), Vol. 6548, pp. 39–48 (2007).

[SR.9] Yang, X., Zhao, X., Yang, K., Liu, Y., Liu, Y., Fu, W., and Luo, Y. *Trends in Biotechnol.* **34**, 810–824 (2016).

[SR.10] Akyildiz, I. F., Jornet, J. M., and Han, C. *Phys. Commun.* **12**, 16–32 (2014).

[SR.11] Sharma, G., Razzari, L., Su, F. H., Blanchard, F., Ayesheshim, A., Cocker, T. L., Titova, L. V., Bandulet, H. C., Ozaki, T., Kieffer, J. C., Morandotti, R., Reid, M., and Hegmann, F. A. *IEEE Photonics Journal* **2**, 578–592 (2010).

[SR.12] Razzari, L., Su, F. H., Sharma, G., Blanchard, F., Ayesheshim, A., Bandulet, H. C., Morandotti, R., Kieffer, J. C., Ozaki, T., Reid, M., and Hegmann, F. A. *Phys. Rev. B* **79**, 193204 (2009).

[SR.13] Chai, X., Ropagnol, X., Raeis-Zadeh, S. M., Reid, M., Safavi-Naeini, S., and Ozaki, T. *Phys. Rev. Lett.* **121**, 143901 (2018).

[SR.14] Hafez, H. A., Kovalev, S., Deinert, J. C., Mics, Z., Green, B., Awari, N., Chen, M., Germanskiy, S., Lehnert, U., Teichert, J., Wang, Z., Tielrooij, K. J., Liu, Z., Chen, Z., Naritaa, A., Müllen, K., Bonn, M., Gensch, M., and Turchinovich, D. *Nature* **561**, 507 (2018).

[SR.15] Langer, F., Baierl, S., Huttner, U., Koch, S. W., Kira, M., Huber, M. A., Mooshammer, F., Plankl, M., Peller, D., Cocker, T. L., Repp, J., and Huber, R. in *Nonlinear Optics.* (Optical Society of America), p. NW2A.5 (2017).

[SR.16] Langer, F., Hohenleutner, M., Schmid, C. P., Poellmann, C., Nagler, P., Korn, T., Schüller, C., Sherwin, M. S., Huttner, U., Steiner, J. T., Koch, S. W., Kira, M., and Huber, R. *Nature* **533**, 225 (2016).

[SR.17] Langer, F., Schmid, C. P., Schlauderer, S., M. Gmitra, J. F., Nagler, P., Schüller, C., Korn, T., Hawkins, P. G., Steiner, J. T., Huttner, U., Koch, S. W., Kira, M., and Huber, R. *Nature* **557**, 76 (2018).

[SR.18] Chai, X., Ropagnol, X., Ovchinnikov, A., Chefonov, O., Ushakov, A., Garcia-Rosas, C. M., Isgandarov, E., Agranat, M., Ozaki, T., and Savel'ev, A. *Opt. Lett.* **43**, 5463–5466 (2018).

[SR.19] Ashcroft, N. W. and Mermin, N. D. *Solid State Physics.* (Saunders College, Philadelphia, USA), 1st edition (1976).

[SR.20] Ibach, H. and Lüth, H. *Solid–State Physics: An Introduction to Principles of Materials Science.* (Springer Berlin Heidelberg, Heidelberg, Germany), 4th edition (2009).

[SR.21] Böer, H. K. W. and Pohl, U. *Semiconductor Physics.* (Springer International Publishing, Berlin, Germany), 1st edition (2018).

[SR.22] Jacoboni, C. and Reggiani, L. *Rev. Mod. Phys.* **55**, 645–705 (1983).

[SR.23] Lundstrom, M. *Fundamentals of Carrier Transport.* (Cambridge University Press, Cambridge, UK), 2nd edition (2000).

[SR.24] Lebwohl, P. and Price, P. *Solid State Commun.* **9**, 1221–1224 (1971).

[SR.25] Oh, K. H., Ong, C. K., and Tan, B. T. G. *J. Phys. Chem. Solids* **53**, 555–559 (1992).

[SR.26] Reklaitis, A. *Phys. Status Solidi B* **249**, 1566–1570 (2012).

[SR.27] Brunetti, R. and Jacoboni, C. *Transient and Stationary Properties of Hot–Carrier Diffusivity in Semiconductors.* in *Semiconductors Probed by Ultrafast Laser Spectroscopy*, ed. Alfano, R. R. (Academic Press, Inc., New York), pp. 367–412 (1984).

[SR.28] Jacoboni, C. and Lugli, P. *The Monte Carlo Method for Semiconductor Device Simulation.* (Springer–Verlag Wien, New York), 1st edition (1989).

[SR.29] Kushner, M. J. J. *Appl. Phys.* **58**, 4024–4031 (1985).

[SR.30] Thompson, B. E., Sawin, H. H., and Fisher, D. A. *J. Appl. Phys.* **63**, 2241–2251 (1988).

[SR.31] Feoktistov, V. A., Mukhovatova, A. V., Popov, A. M., and Rakhimova, T. V. *J. Phys. D: Appl. Phys.* **28**, 1346–1383 (1995).

[SR.32] Bogaerts, A. and Gijbels, R. *IEEE Trans. Plasma Sci.* **27**, 1406–1415 (1999).

[SR.33] Long, A. P., Beton, P. H., and Kelly, M. J. *J. Appl. Phys.* **62**, 1842–1849 (1987).

[SR.34] Goldberg, Y. A. and Schmidt, N. M. *Gallium Indium Arsenide* ($Ga_xIn_{1-x}As$)*.* in *Handbook Series on Semiconductor Parameters*, eds. Levinshtein, M., Rumyantsev, S., and Shur, M. (World Scientific, London) Vol. 2, pp. 62–88 (1996).

[SR.35] Vasileska, D. and Goodnick, S. M. *Mater. Sci. Eng. Rep.* **R38**, 181 (2002).

[SR.36] Al-Naib, I., Sipe, J. E., and Dignam, M. M. *Phys. Rev. B* **90**, 245423 (2014).

[SR.37] Bowlan, P., Martinez-Moreno, E., Reimann, K., Elsaesser, T., and Woerner, M. *Phys. Rev. B* **89**, 041408 (2014).

[SR.38] Schubert, O., Hohenleutner, M., Langer, F., Urbanek, B., Lange, C., Huttner, U., Golde, D., Meier, T., Kira, M., Koch, S. W., and Huber, R. *Nat. Photonics* **8**, 119 (2014).

[SR.39] Kutz, J. N. *Data–Driven Modeling Scientific Computation: Methods for Complex Systems Big Data.* (Oxford University Press, Inc., New York), 1st edition (2013).

[SR.40] Mallat, S. *A Wavelet Tour of Signal Processing: The Sparse Way.* (Academic Press, Inc., Orlando), 3rd edition (2008).

[SR.41] Tikhomirov, I., Sato, T., and Ishikawa, K. L. *Phys. Rev. Lett.* **118**, 203202 (2017).

[SR.42] Tarekegne, A. T., Iwaszczuk, K., Zalkovskij, M., Strikwerda, A. C., and Jepsen, P. U. *New J. Phys.* **17**, 043002 (2015).

[SR.43] M. Mohamed, A. Bharthuar, and U. Ravaioli, DOI: 10.4231/D38C9R505 (2015).

[SR.44] Kuehn, W., Gaal, P., Reimann, K., Woerner, M., Elsaesser, T., and Hey, R. *Phys. Rev. B* **82**, 075204 (2010).

[SR.45] Reimann, K. *Rep. Prog. Phys.* **70**, 1597–1632 (2007).

[SR.46] Kuehn, W., Gaal, P., Reimann, K., Woerner, M., Elsaesser, T., and Hey, R. *Phys. Rev. Lett.* **104**, 146602 (2010).

[SR.47] Floss, I., Lemell, C., Wachter, G., Smejkal, V., Sato, S. A., Tong, X. M., Yabana, K., and Burgdörfer, J. *Phys. Rev. A* **97**, 011401 (2018).

Table of Contents

Acknowledgements **III**

Abstract **V**

Résumé **IX**

Sommaire Récapitulatif **XI**

- 0.1 Introduction . . . XI
  - 0.1.1 Physique des semi–conducteurs . . . XII
- 0.2 Équations de transport des transporteurs . . . XIV
  - 0.2.1 L'équation de transport de Boltzmann . . . XV
  - 0.2.2 Solution numérique de l'équation de Boltzmann: approche d'ensemble Monte–Carlo . . . XVIII
- 0.3 Résultats des effets optiques non linéaires THz dans le semi–conducteur dopé n–$\mathrm{In}_{0.57}\mathrm{Ga}_{0.43}\mathrm{As}$ . . . XX
  - 0.3.1 Impulsions de THz à fréquence relativement basse et haute . . . XXI
  - 0.3.2 Analyse temps–fréquence pour les impulsions THz à basse fréquence . . . XXIII
  - 0.3.3 Analyse temps–fréquence pour les impulsions THz à haute fréquence . . . XXIV
  - 0.3.4 Masse effective moyenne des porteurs . . . XXVI
- 0.4 Conclusion . . . XXVII
- Références . . . VIII

List of Figures **XI**

List of Tables **XIII**

List of symbols and abbreviations **XV**

Publications during the M. Sc. **XVII**

Contributions to national and international conferences during the M. Sc. **XIX**

1 Introduction **1**

- 1.1 Methods for generating intense THz radiation . . . 3
  - 1.1.1 Photoconductive antenna . . . 3
  - 1.1.2 Optical rectification . . . 4
- 1.2 Methods for THz detection . . . 5
  - 1.2.1 Electro–optic sampling technique . . . 5
  - 1.2.2 Stokes–Mueller method . . . 6
- 1.3 THz time–domain spectroscopy . . . 8

1.3.1 Transmission thin–film theory . . . 10
1.3.2 Previous THz spectroscopy results of n–doped InGaAs thin films . . . 12
1.4 Intense THz–matter interaction and nonlinear THz effects . . . 16
1.4.1 High–order sideband generation . . . 16
1.4.2 High–order THz harmonic generation . . . 17
1.5 Transient carrier dynamics . . . 18
1.5.1 Semiconductor physics . . . 19
1.6 Justification, main objective and structure of the thesis . . . 20

2 Carrier–Transport Equations 23
2.1 Phonon scattering . . . 23
2.2 Intravalley scattering . . . 23
2.2.1 Intravalley acoustic phonon scattering . . . 23
2.2.2 Intravalley optical phonon scattering . . . 24
2.3 Intervallley scattering . . . 24
2.4 Carrier transport in multivalley semiconductors . . . 25
2.5 The Boltzmann transport equation . . . 26
2.6 Numerical solution of the Boltzmann equation: ensemble Monte–Carlo approach . . . 29

3 Study on the nonlinear THz optical effects in n–doped semiconductor $In_{0.57}Ga_{0.43}As$ 34
3.1 THz pulses with relatively low and high frequency . . . 37
3.2 Gábor transform formalism . . . 39
3.3 Time–frequency analysis for low–frequency THz pulses . . . 40
3.4 Time–frequency analysis for high–frequency THz pulses . . . 42
3.5 Average effective carrier mass . . . 45

4 Conclusions and outlooks 47

References 49

List of Figures

1 Le spectre de rayonnement électromagnétique XI
2 Schéma d'un système de spectroscopie THz résolue en temps. XII
3 Génération de paires électrons–trous (porteurs) dans les semi–conducteurs XIII
4 Mécanismes de diffusion dans un semi–conducteur typique XIV
5 Schéma de la structure de la bande $\mathrm{In_{0.57}Ga_{0.43}As}$ XV
6 Schéma de la méthode de Monte–Carlo XVIII
7 Esquisse de vol libre dispersé XIX
8 Incidence et transmission normales du champ électrique de THz à travers un film conducteur mince déposé sur un substrat diélectrique XX
9 Densité de courant et forme d'onde THz transmise générée par une impulsion THz à plusieurs cycles XXII
10 Simulations de HHG, LFC et HFC XXIII
11 Analyse temps–fréquence des champs de crête incidents à 350 kV/cm pour une impulsion de 0.2 THz XXIV
12 Analyse temps–fréquence des champs crêtes incidents à 114 kV/cm pour une impulsion de 1.0 THz XXV
13 Spectres d'amplitude de la masse effective de chaque porteuse moyenne pour les champs de crête incidents à (a) 350 kV/cm pour 0.2 THz et (b) 114 kV/cm pour 1.0 THz. XXVI

1.1 Spectrum of electromagnetic radiation 1
1.2 Sketch diagram of a terahertz time–domain spectroscopy system 2
1.3 THz generation from a large–aperture photoconductive antenna 3
1.4 THz generation via optical rectification 5
1.5 THz detection system using EO sampling technique 5
1.6 THz detection system using Stokes–Mueller formalism 8
1.7 Schematic diagram of a THz–TDS setup 9
1.8 Normal incidence and transmission of THz electric field through a thin conducting film layer 10
1.9 Z scan theoretical and experimental results 13
1.10 Polarization–dependent TPTP experimental results 14
1.11 Sub–cycle THz nonlinear experiments 15
1.12 Classical schematic diagram of the semi–classical three–step model 16
1.13 Experimental results of the high–order sideband generation in $\mathrm{WSe_2}$ 17
1.14 Experimental results of the high–order THz harmonic generation in a single–layer of graphene 18
1.15 Generation of electron–hole pairs (carriers) in semiconductors 19

2.1 Scattering mechanisms in a typical semiconductor 25
2.2 A schematic view of $\mathrm{In}_{0.57}\mathrm{Ga}_{0.43}\mathrm{As}$ band structure 26
2.3 Sketch diagram of the Monte–Carlo method 29
2.4 Scattered free flight sketch 32
2.5 Energy band model for $\mathrm{In}_{0.57}\mathrm{Ga}_{0.43}\mathrm{As}$ 32

3.1 Normal incidence and transmission of THz electric field through a thin conducting film deposited on a dielectric substrate 35
3.2 Schematic Monte–Carlo algorithm flow diagram 36
3.3 Current density and transmitted THz waveform generated by an incident multi–cycle THz pulse 37
3.4 Simulations of HHG, LFC and HFC 38
3.5 Example of the Gábor transform filter analysis 39
3.6 Time–frequency analysis for the incident peak fields at 350 kV/cm for 0.2 THz pulse 40
3.7 Time–frequency analysis for the incident peak fields at 350 kV/cm for 0.4 THz pulse 41
3.8 Time–frequency analysis for the incident peak fields at 114 kV/cm for 1.0 THz pulse 42
3.9 Time–frequency analysis for the incident peak fields at 125 kV/cm for 1.5 THz pulse 43
3.10 Time–frequency, LFC and HFC generation analysis for multi–cycle THz pulses . . . 44
3.11 Calculated average electron effective mass of each Γ, L and X valley as a function of the average energy and time of the THz pulse 45
3.12 Amplitude spectra of each average carrier effective mass for the incident peak fields at 350 kV/cm for 0.2 THz and 114 kV/cm for 1.0 THz. 46

List of Tables

2.1 Table of physical constants of $In_{0.57}Ga_{0.43}As$ 33

List of abbreviations and symbols

Abbreviation	**Meaning**
DOS	Density of state
EO	Electro–optic
FFT	Fast Fourier Transform
HFC	High–frequency components
HH	High–harmonic
HHG	High–order harmonic generation
HSG	High–order sideband generation
NIR	Near–infrared
LAPCA	Large aperture photoconductive antenna
LCVR	Liquid crystal variable retarder
LFC	Low–frequency components
OR	Optical rectification
PCA	Photoconductive antenna
PSA	Polarization state analyzer
THz	Terahertz
THz–TDS	Terahertz time–domain spectroscopy

Symbol	**Meaning**
α_i	Nonparabolicity factor of each valley
$\langle E_i \rangle$	Average energy of the carriers
$\mathbf{E}(\omega)$	Electric field in the frequency domain
$\mathcal{E}$	Energy
$E_{\mathrm{in.}}$	Incident THz electric field
E_g	Energy of band gap
E_{THz}	THz electric field
$E_{\mathrm{trans.}}$	Transmitted THz electric field
e	Electron charge
ϵ_0	Permittivity of free space in SI units
$f(\mathbf{r}, \mathbf{k}, t)$	Electron state probability with position $\mathbf{r}$ and wave–vector $\mathbf{k}$ is occupied at time t

$F(\omega)$	Fourier transform
$G(\tau, \omega)$	Gábor transform
g_x	Gaussian filter function
$\mathbf{G}$	Reciprocal lattice
$\Gamma_{\text{self}}\left[\mathbf{k}\left(t\right)\right]$	Self–scattering rate
$\Gamma\left[\mathbf{k}\left(t\right)\right]$	Scattering rate of an electron or hole of wave–vector **k** per unit time
$\hbar$	Plank's constant ($h/2\pi$)
$J(t)$	Current density
k or $\lvert\mathbf{k}\rvert$	Magnitude of the wave–vector
$\langle m_i^* \rangle$	Average effective carrier mass
m_1	Density of state effective mass of electrons in each valley
n_0	Refractive index
$\mathbf{P}(t)$	Electric polarization vector
$\mathcal{P}_{\text{in}}$	Probability of scattering into **k**
$\mathcal{P}_{\text{out}}$	Probability of scattering out of **k**
r_{41}	EO coefficient of the detection crystal
S_{in}	Stokes vector for right circularly polarized light
S_{THz}	Stokes vector of the transmitted THz light
$S\left(\mathbf{k}' - \mathbf{k}\right)$	Structure factor
$\sigma(t)$	Photoconductivity
t_r	Free flight time
$v_{\text{opt,gr}}$	Optical group velocity
$v_{\text{THz,phase}}$	THz phase velocity
ω	Frequency
ω_0	Angular frequency of the optical probe beam
$\chi_e^{(n)}$	n–th order electric susceptibility
Y_S	Admittance of the substrate
Y_0	Free–space admittance
$\sim$	Approximately

Publications during the M. Sc.

1. **C. M. Garcia–Rosas**, X. Chai, X. Ropagnol and T. Ozaki, “Time–frequency analysis of nonlinear terahertz signals due to hot electrons in the nonparabolic conduction bands of *n*–doped $In_{0.57}Ga_{0.43}As$ films”, submitted for publication in Physics Review Letters.

2. **C. M. Garcia–Rosas**, L. A. Medina, P. Lopez, N. Large and A. Reyes–Coronado, “Magneto–plasmonic biocompatible nanorice”, J. Nanoparticle Res. **23**, 144 (2021).

3. X. Ropagnol, Zs. Kovács, B. Gilicze, M. Zhuldybina, F. Blanchard, **C. M. Garcia–Rosas**, S. Szatmári, I.B. Földes and T. Ozaki, “Intense sub–terahertz radiation from wide–bandgap semiconductor based large–aperture photoconductive antennas pumped by UV lasers”, New J. Phys. **21**, 113042 (2019).

Contributions to national and international conferences during the M. Sc.

1. **C. M. Garcia–Rosas**, X. Chai, X. Ropagnol and T. Ozaki, "Multi–cycle nonlinear carrier dynamics of *n*–doped semiconductor $In_{0.57}Ga_{0.43}As$". In IONS OPUMA 2020, June 8th–12th, 2020. Querétaro, Mexico. [ORAL PRESENTATION]
2. **C. M. Garcia–Rosas**, X. Chai, X. Ropagnol and T. Ozaki, "Multi–cycle nonlinear carrier dynamics of *n*–doped semiconductor $In_{0.57}Ga_{0.43}As$". In Seminar for Master's Students of Energy and Material Sciences, INRS–ÉMT, 22nd April 2020. Varennes, Québec, Canada. [2nd BEST ORAL PRESENTATION]
3. **C. M. Garcia–Rosas**, X. Chai, X. Ropagnol and T. Ozaki, "Multi–cycle nonlinear carrier dynamics of *n*–doped semiconductor $In_{0.57}Ga_{0.43}As$". In Second Annual Optics and Photonics Student Conference, 26th & 27th September 2019. Toronto, Ontario, Canada. [POSTER]
4. **C. M. Garcia–Rosas**, A. Reyes–Coronado, "Study of the electromagnetic response of magneto–plasmonic nanoparticles for biomedical applications". In Institute of Physics "Gleb Wataghin" Winter Schools/International OSA Network of Students–Latin American School of Optics 2019 (IFGW Winter Schools/IONS–ELO 2019), July 22nd–26th, 2019. Campinas, Sao Paolo, Brazil. [BEST ORAL PRESENTATION AWARD]
5. **C. M. Garcia–Rosas**, X. Chai, X. Ropagnol and T. Ozaki, "Multi–cycle nonlinear carrier dynamics of *n*–doped semiconductor $In_{0.57}Ga_{0.43}As$". In Institute of Physics "Gleb Wataghin" Winter Schools/International OSA Network of Students–Latin American School of Optics 2019 (IFGW Winter Schools/IONS–ELO 2019), July 22nd–26th, 2019. Campinas, Sao Paolo, Brazil. [POSTER]
6. **C. M. Garcia–Rosas**, A. Reyes–Coronado, "Study of the electromagnetic response of magneto–plasmonic nanoparticles for biomedical applications". In International School on Plasmonics, Magnetoplasmonics and Applications (ISPMA–2019), April 29th–May 3rd, 2019. Bogota, Colombia. [BEST POSTER AWARD]

Chapter 1

Introduction

Terahertz (THz) radiation has attracted keen interest from the scientific and technological communities, due to its non–invasive, non–ionizing properties and exceptional spectroscopic and sensing abilities [1, 2]. By definition, 1 THz $= 10^{12}$ Hz and corresponds to a wavelength of 300 μm $\left(33\,\mathrm{cm}^{-1}\right)$ and a period of 1 picosecond. Via the Boltzmann constant, 1 THz has a thermal energy temperature of 48 Kelvin and a photon energy of 4.1 meV. Generally, the THz radiation frequency range lies between 0.1 and 10 THz of the electromagnetic spectrum [see Fig. 1.1] [3].

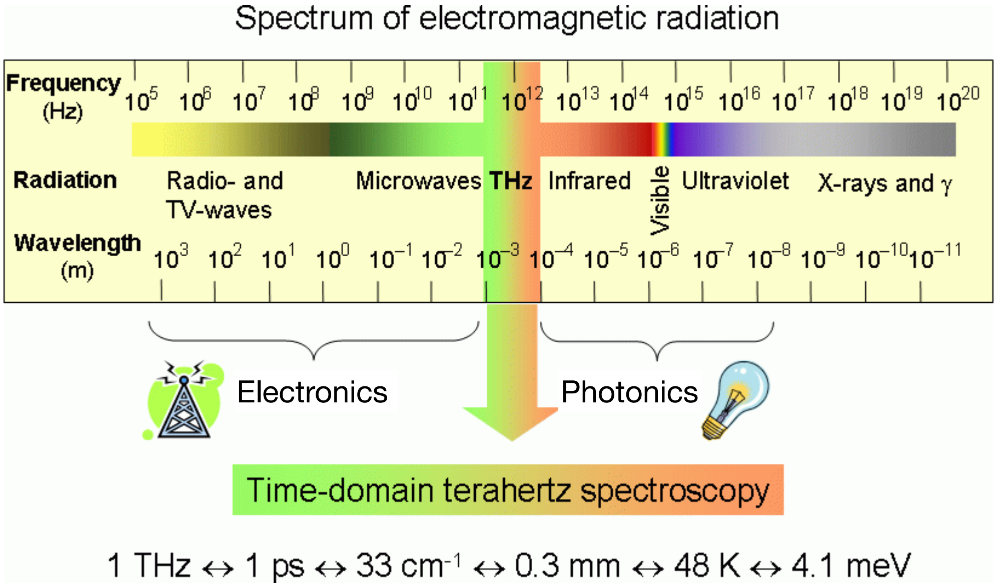
Spectrum of electromagnetic radiation
Frequency (Hz)
10^5 10^6 10^7 10^8 10^9 10^{10} 10^{11} 10^{12} 10^{13} 10^{14} 10^{15} 10^{16} 10^{17} 10^{18} 10^{19} 10^{20}
Radiation
Radio- and TV-waves
Microwaves
THz
Infrared
Visible
Ultraviolet
X-rays and γ
Wavelength (m)
10^3 10^2 10^1 10^0 10^{-1} 10^{-2} 10^{-3} 10^{-4} 10^{-5} 10^{-6} 10^{-7} 10^{-8} 10^{-9} 10^{-10} 10^{-11}
Electronics
Photonics
Time-domain terahertz spectroscopy
1 THz ↔ 1 ps ↔ 33 cm^{-1} ↔ 0.3 mm ↔ 48 K ↔ 4.1 meV

Figure 1.1: Spectrum of electromagnetic radiation [3].

On both sides of the THz gap, there are radiation sources with sufficient power in the electronic (millimeter waves, with a frequency below 0.1 THz) and photonic (infrared, with frequency above 10 THz) regimes [1, 2]. However, the lack of THz sources and detectors has left a gap in the understanding of physical phenomena at these particular frequencies. THz radiation is a new word that used to be called the far–infrared, and there have been an abundance of studies in this spectral region, from molecular spectroscopy to astronomy [4–8]. Few–cycle THz pulses and electro–optic sampling techniques have opened up various new opportunities that were challenging to access in the past. One technique to characterize or understand this type of phenomenon is the terahertz time–domain spectroscopy (THz–TDS) [1]. One unique aspect of THz spectroscopy is the coherent generation and detection combined with the pump–probe technique, which allows time–resolved THz electric field measurements [9–12]. THz–TDS is a standard method and a powerful technique for studying the dielectric properties of materials. Such systems typically possess a similar configuration, where the optical laser beam is separated into two parts: one for the THz generation and another for the THz detection, as shown in figure 1.2.

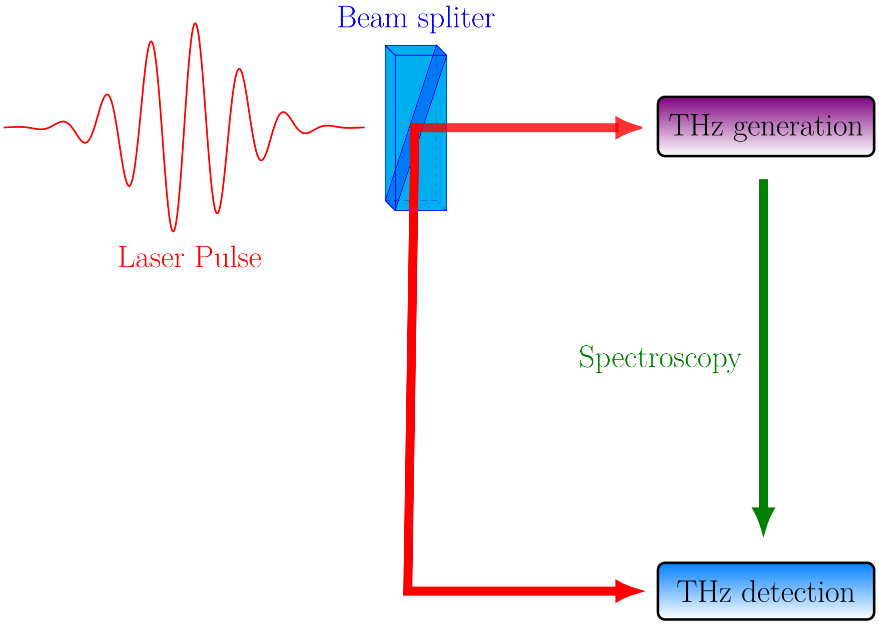

Figure 1.2: Sketch diagram of a terahertz time–domain spectroscopy system.

Because THz bridges the microwave and far–infrared regions, THz radiation creates a broad and important range of applications, such as imagining, telecommunications, biomedical diagnosis [13–15]. We can also study the nonlinear THz effects theoretically and experimentally, carrier dynamics and high–order harmonic generation of materials [16–22]. Previous works have studied the evolution of nonlinear effects and carrier dynamics during the interaction of subcycle and few–cycle THz pulses with doped semiconductors [16–18, 23].

In the following sections of this dissertation, for simplicity, we briefly describe two THz generation sources: photoconductive antenna (PCA), which is based on the acceleration of photoexcited carriers [10, 24], and optical rectification (OR), where the second–order nonlinear process takes place in a noncentrosymmetric crystal [25, 26]. Meanwhile, in section 1.2, we describe in detail the advantages and disadvantages of several THz detection methods, and a new approach based on the Stokes–Mueller formalism, which uses a polarization state analyzer after the electro–optic (EO) sampling crystal [27]. In addition, we describe the properties of semiconductor materials and the generation of transient carrier dynamics. To model and analyse the carrier transport phenomena, the Boltzmann transport equation [28–30] can be used as a general formalism to determine how physical quantities change, such as energy and momentum, but it is a complicated integro–differential equation. Nevertheless, this challenging equation can be solved numerically using the Monte–Carlo method [18, 31–37].

1.1 Methods for generating intense THz radiation

1.1.1 Photoconductive antenna

THz generation from a photoconductive antenna (PCA) arises from the photoexcited carriers being accelerated by the bias field. Two of the most unique characteristics of THz pulses generated by PCAs are their quasi–half–cycle nature, and their relatively low central frequency, which lies between 0.05 and 1 THz. To generate high–intensity THz pulses, it is necessary to increase the aperture of the PCA, and hence large aperture photoconductive antennas (LAPCAs) [see Figure 1.3(a)] has been studied and developed [38, 39]. Figure 1.3(a) shows a schematic diagram of a LAPCA THz source, with an applied bias voltage V_{bias} and corresponding bias electric field $\mathbf{E}_{\text{bias}}$. The general structure of a LAPCA consists of two parallel conducting electrodes that are deposited onto a high–resistivity semiconductor substrate [40]. When the emitter is illuminated by a femtosecond laser pulse, free carriers are generated in the substrate. By applying an external bias field between the electrodes, a photocurrent is achieved along the substrate. The generation of pulsed electromagnetic waves in the reflection and transmission directions of the PCA, in the THz frequency range, is caused by variations in the photocurrent density at the picosecond time scale.

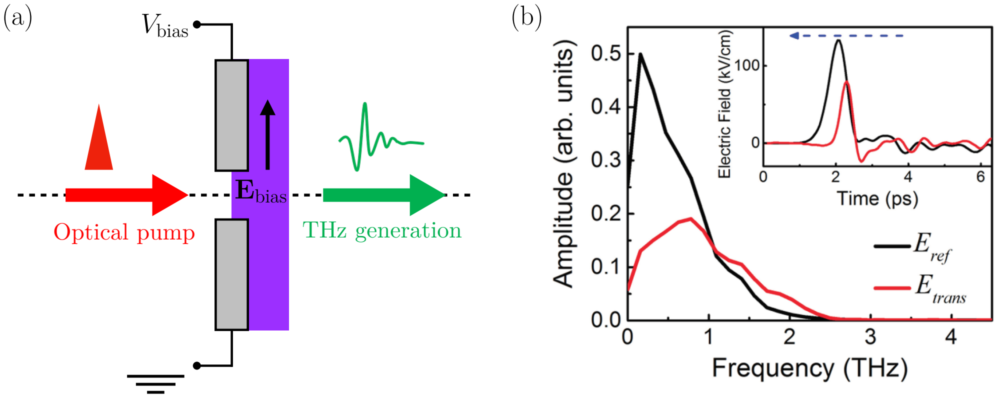

Figure 1.3: (a) Schematic diagram of the THz generation from a large–aperture PCA. The two electrodes are deposited in a high resistivity semiconductor substrate, and the applied bias voltage that goes through the substrate accelerates the photoexcited carriers. (b) Amplitude spectra of the incident (E_{ref}) and transmitted (E_{trans}) terahertz pulses, with an incident peak field of 190 kV/cm. From ~1.0 THz up to 2.5 THz, we found high–frequency generation (HFG) with spectral amplitude enhancement. Inset: corresponding incident and transmitted terahertz waveforms where propagation direction indicated by the blue arrow [18].

The THz electric field E_{THz} is proportional to the time derivative of the transient current density $J(t)$ and the bias electric field E_{bias}, that is [10, 11]:

$$E_{\text{THz}}(t) \propto \frac{dJ(t)}{dt} \propto E_{\text{bias}} \frac{d\sigma(t)}{dt},$$

where $\sigma(t)$ is the photoconductivity.

Moreover, for high–power THz sources, the interdigitated LAPCA (iLAPCA) structure is currently the most commonly used design [41, 42]. A typical THz pulse generated by an iLAPCA THz source is shown in Figure 1.3(b). Chai *et al.* performed nonlinear THz time–domain spectroscopy experiments on n–doped $\text{In}_{0.57}\text{Ga}_{0.43}\text{As}$ using a quasi–half–cycle THz pulse with a fundamental frequency of less than 0.2 THz [see Fig. 1.3(b)], demonstrating the subcycle control of THz nonlinearities and THz high–frequency generation based on intraband carrier scattering effects [18]. The interaction of intense, few–cycle THz pulses with matter and the observation of nonlinear THz effects have recently attracted considerable attention from the scientific community [16–18, 23, 43–46].

1.1.2 Optical rectification

When an intense optical beam is transmitted through a nonlinear medium (noncentrosymmetric crystal), we generate a quasi–DC (low–frequency) nonlinear polarization, namely non–zero average value. Optical rectification (OR) is a nonlinear optical phenomenon of second–order, and it is essentially a difference–frequency generation with a low frequency difference close to zero. In nonlinear optics, the electric polarization vector is given by

$$\mathbf{P}(t) = \epsilon_0 \left[\chi_e^{(1)} \mathbf{E}(t) + \chi_e^{(2)} \mathbf{E}(t)\mathbf{E}(t) + \chi_e^{(3)} \mathbf{E}(t)\mathbf{E}(t)\mathbf{E}(t) + \ldots \right],$$

where ϵ_0 is the permittivity of free space and $\chi_e^{(n)}$ is the n–th order electric susceptibility tensor of the material [25, 26]. Also, it is important to mention that the electric susceptibility tensor is not time–dependent because we are considering only instantaneous nonlinear effects. Moreover, in this case the acceleration (or deceleration) of charges are in a bound dipole form, and hence the THz generation via OR takes place in the lowest order of the nonlinear process in the noncentrosymmetric crystal [see Fig. 1.4(a)], which is the second–order nonlinear susceptibility of the material, hence

$$\mathbf{P}_{\mathrm{OR}}^{(2)} = \epsilon_0 \chi_e^{(2)} \left(\Omega; \omega_1, -\omega_2 \right) \mathbf{E} \left(\omega_1 \right) \mathbf{E}^* \left(\omega_2 \right).$$

Here, $\Omega = \omega_2 - \omega_1$ is the frequency difference between the two frequency components of the optical pump ω_1 and ω_2 [10]. The radiated THz field is proportional to the partial second time derivative of this two–order electric polarization vector

$$\mathbf{E}_{\mathrm{THz}}^{\mathrm{rad}} \propto \frac{d\mathbf{J}(t)}{dt} = \frac{\partial^2 \mathbf{P}(t)}{\partial t^2} = \frac{\partial^2 \mathbf{P}_{\mathrm{OR}}^{(2)}(t)}{\partial t^2}.$$

In order to improve the optical–to–THz conversion efficiency, nonlinear crystals with a high nonlinear coefficient at the optical pump wavelength must be employed. For example, at 800 nm, ZnTe ($r_{41} = 4.04$ pm/V) and LiNbO$_3$ ($r_{33} = 30.9$ pm/V) [10, 25] are the most commonly used nonlinear crystals. Moreover, we can perform a simple collinear experimental configuration at this particular wavelength, using either ZnTe or DAST crystal. However, since the nonlinear coefficient of the ZnTe crystal is low, only large aperture ZnTe crystals can produce high–energy THz pulses [47]. Additionally, organic crystals such as DAST, have a lower damage threshold than inorganic crystals [10, 25], despite having a higher conversion efficiency. One of the most popular inorganic crystals used in the laboratory as an intense THz source is the LiNbO$_3$ crystal. Moreover, many groups have used zinc–blende crystals such as ZnTe [47, 48] and GaP [49] as a way to generate OR THz pulses [see Fig. 1.4(b)]. For an efficient OR process, we need to determine the optimal conditions of the crystal orientation and thickness to achieve the matching between the optical group velocity and the THz phase velocity. In the OR process, the phase–matching condition is given by

$$\Delta \mathbf{k} = \mathbf{k}(\omega_{\mathrm{opt.}} + \omega_{\mathrm{THz}}) - \mathbf{k}(\omega_{\mathrm{opt.}}) - \mathbf{k}_{\mathrm{THz}}(\omega_{\mathrm{THz}}) = \mathbf{0},$$

where $\omega_{\mathrm{opt.}}$ and ω_{THz} are the optical and THz wave frequencies, respectively. Here, either $\omega_{\mathrm{opt.}}$ and $(\omega_{\mathrm{opt.}} + \omega_{\mathrm{THz}})$ lie within the spectra of the optical pulse. If we only consider the first term of a Taylor expansion over $\mathbf{k}(\omega_{\mathrm{opt.}} + \omega_{\mathrm{THz}})$, then

$$\mathbf{k}(\omega_{\mathrm{opt.}}) + \omega_{\mathrm{THz}} \frac{\partial}{\partial \omega_{\mathrm{opt.}}} \mathbf{k}(\omega_{\mathrm{opt.}}) - \mathbf{k}(\omega_{\mathrm{opt.}}) = \mathbf{k}_{\mathrm{THz}}(\omega_{\mathrm{THz}}).$$

Thus, by applying the chain rule to the last equation, the phase–matching condition in the infinitesimal limit approach [10] is given by

$$v_{\text{opt,gr}} = \frac{\omega_{\text{THz}}}{|\mathbf{k}_{\text{THz}}|} = \frac{\partial \omega_{\text{opt.}}}{\partial k_{\text{opt.}}} = v_{\text{THz, phase}}.$$

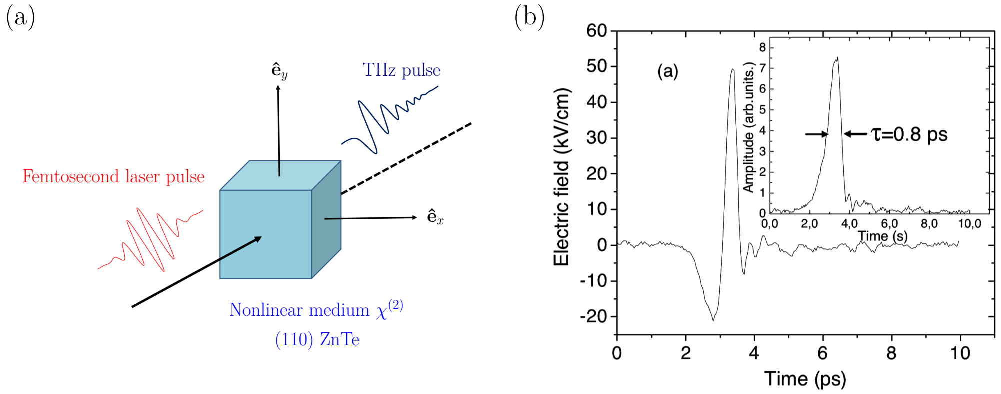

Figure 1.4: (a) Schematic diagram of the THz generation via OR using a zinc–blende crystal ZnTe. (b) THz pulse waveform obtained in a N_2–purged environment using a 20 μm thick ZnTe EO detection crystal. Inset: corresponding spectra using Hilbert transform [47].

1.2 Methods for THz detection

1.2.1 Electro–optic sampling technique

Because standard optical detectors do not have a picosecond resolution, a type of pump–probe detection technique should be used to measure the output signal with a sub–picosecond resolution. The technique is called EO sampling, where an EO sampling crystal is irradiated by the output THz signal as a pump and a weak NIR optical pulse as a probe. The widely used EO sampling technique has made THz–TDS an extremely powerful tool to investigate the linear and nonlinear properties of materials in the far–infrared spectral range [10–12]. In EO sampling, a THz field modulates the birefringence of the detection crystal, which changes the polarization state of the probe optical laser pulse [12]. The THz electric field is then retrieved by measuring this change in polarization of the probe beam using a balanced detection configuration [see Fig. 1.5] [1, 12].

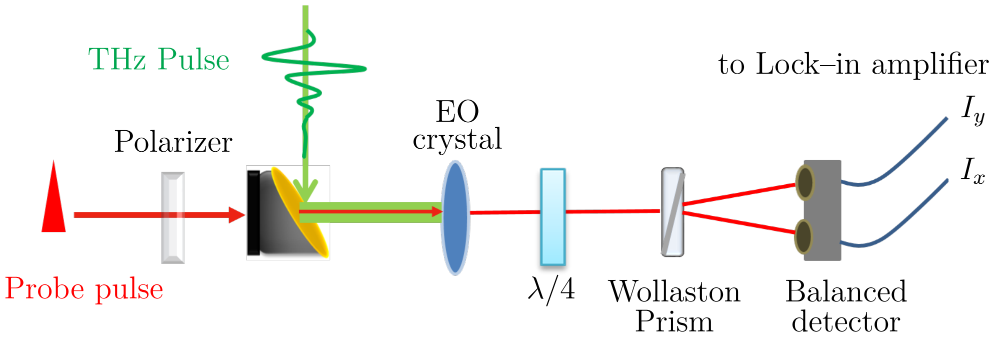

Figure 1.5: Schematic diagram of the THz detection system using EO sampling technique [1].

Recently, with the development of numerous intense THz sources [39, 50–53], various ultrafast subcycle nonlinearities have been revealed through straightforward time–domain analysis enabled by EO sampling [18, 54]. However, the conventional EO sampling technique has challenging limitations to overcome: the small–angle approximation [1, 2, 12] and the problem of over–rotation [55–57]. Thus, the resolve these two problems and be able to detect intense THz fields, we need to use either a thin detection crystal (resulting in multiple closely spaced reflection from the air–crystal interfaces) or reduce the THz beam intensity before the detection crystal with multiple attenuators [18, 54, 58]. The use of thin detector crystals reduces the dynamic range as well as the spectral resolution due to the interference reflection signals from the crystal surface. Further, since THz attenuators usually are only used for high–field measurements, it becomes challenging to make a direct spectral comparison between high–field and low–field responses. This effect becomes more challenging when performing nonlinear measurements by changing from low to high THz electric field because to obtain a better signal–to–noise ratio, THz attenuators are not used for low–field THz measurements.

On the other hand, measuring the change in the THz electric field orientation via the conventional EO sampling technique is usually complicated. In experiments in which an elliptical or circular THz polarization is induced, the detection of the two orthogonal components (E_x and E_y) is made by rotating manually a wire–grid polarizer and optimizing the orientation of the detection crystal [59–63]. Nevertheless, several measurement approaches have been developed to determine the polarization state of the THz wave adequately [64–71]. However, the disadvantage of employing a combination of half–wave plate and wire–grid polarizer lies in the fact that the linearity of EO sample technique measurements is accurate only at relatively low THz fields. From this moment onwards, we describe and show a new technique that can fully consider the complete polarization variation of the optical probe beam, express the polarization of light by implementing the general Stokes–Mueller formalism.

1.2.2 Stokes–Mueller method

The Stokes parameters describe the general state of polarization of an electromagnetic wave and its change upon interaction with an optical element (polarizer, retarder, reflector, scatterer) [72]. The Stokes parameters of a light wave are measurable quantities, defined as:

$$\begin{pmatrix} S_0 \\ S_1 \\ S_2 \\ S_3 \end{pmatrix} = \begin{pmatrix} I_{\text{tot}} \\ I_{0^\circ} - I_{90^\circ} \\ I_{45^\circ} - I_{-45^\circ} \\ I_{RCP} - I_{LCP} \end{pmatrix}, \tag{1.1}$$

where S_0 is the total intensity of light (polarized + unpolarized), S_1 describes the quantity of linear horizontal or vertical polarization, S_2 describes the amount of linear +45° or −45° (135°) polarization and S_3 describes the amount of right circular polarization (RCP) or left circular polarization (LCP) [72]. The direct measurement of the Stokes parameters can describe the different polarization states of THz waves, making it a powerful technique that allows characterizing THz pulse. This new technique based on the Stokes–Mueller formalism avoids the described small–angle approximation or over–rotation limitations due to its ultra–high dynamic range, and additionally, we can determine, as a function of space and time, both polarization direction and amplitude of the THz field.

As we described before, the Stokes parameters can fully define the polarization state of light, and what represents the polarization properties of the medium or an optical element is the 4×4

Mueller matrix, which basically gives the relation between the incident and transmitted Stokes vectors [72, 73]. For the THz detection system, the detector crystal can be treated as a rotating waveplate controlled by the THz electric field [1, 2, 74]. By measuring the Stokes parameters of the probe beam, we can therefore obtain the THz field and polarization information. Indeed, three of the four components are enough to obtain an intense elliptically polarized pulse. Figure 1.6 shows the schematic diagram of the detection system in which the optical probe beam is circularly polarized. A right circularly polarized probe beam can be described by the following Stokes vector [72, 73]

$$S_{\text{in}} = \begin{pmatrix} 1 \\ 0 \\ 0 \\ 1 \end{pmatrix}. \tag{1.2}$$

Then, the nonlinear detection crystal can be considered as a rotated waveplate [see Fig. 1.6], where Mueller matrix for the rotated retarder is given by the Mueller matrix for rotation though $-\theta$, times the Mueller matrix for a retarder with phase shift ϕ, times Mueller matrix for rotation, this is [75]

$$\mathbb{M}_{\text{EO}} = \mathbb{M}_{\text{R}}(-2\theta) \cdot \mathbb{M}_{\phi} \cdot \mathbb{M}_{\text{R}}(2\theta) \tag{1.3}$$

hence

$$\mathbb{M}_{\text{EO}} = \begin{pmatrix} 1 & 0 & 0 & 0 \\ 0 & \cos^2 2\theta + \cos\phi \sin^2 2\theta & (1-\cos\phi)\sin 2\theta \cos 2\theta & \sin\phi \sin 2\theta \\ 0 & (1-\cos\phi)\sin 2\theta\cos 2\theta & \sin^2 2\theta + \cos\phi\cos^2 2\theta & -\sin\phi\cos 2\theta \\ 1 & -\sin\phi\sin 2\theta & \sin\phi\cos 2\theta & \cos\phi \end{pmatrix}, \tag{1.4}$$

where θ is the rotation angle of the induced refractive–index axes due to the variation of THz polarization orientation α and ϕ is the phase retardation induced by the THz field, hence the Stokes vector of the transmitted light is obtained by the product of matrices (1.2) and (1.4), this is

$$S_{\text{THz}} = \begin{pmatrix} S_0 \\ S_1 \\ S_2 \\ S_3 \end{pmatrix} = \begin{pmatrix} 1 \\ \sin\phi\sin 2\theta \\ -\sin\phi\cos 2\theta \\ \cos\phi \end{pmatrix} = \mathbb{M}_{\text{EO}} \cdot S_{\text{in}}. \tag{1.5}$$

We can set along the x–axis laboratory reference the [–110] direction of the (110)–orientated ZnTe crystal [see Fig. 1.6], and hence the delay phase ϕ for a (110) zinc blend nonlinear crystal, such as ZnTe, is denoted by [1]

$$\phi = \frac{\omega_0 d}{2c} n_0^3 r_{41} E_{\text{THz}} \sqrt{1 + 3\cos^2\alpha} \tag{1.6}$$

ω_0 is the angular frequency of the optical probe beam, d is the thickness of the detection crystal, c is the speed of light, α is the angle between the THz electric field vector and the [–110] of the ZnTe crystal, n_0 is the refractive index, and r_{41} is the EO coefficient of the detection crystal. Furthermore, the equation to obtain orientation θ of the refractive–index axis is

$$\cos 2\theta = \frac{\sin\alpha}{\sqrt{1 + 3\cos^2\alpha}}. \tag{1.7}$$

By now, S_{THz} has four parameters that allow one to find the value of the THz electric field E_{THz} and its polarization orientation by solving equations (1.6) and (1.7). Experimentally, such measurements can be accomplished by using the technique of Stokes–Mueller polarimetry [73, 76–78]. To balance the detection, a polarization state analyzer (PSA) was settled, which has two liquid

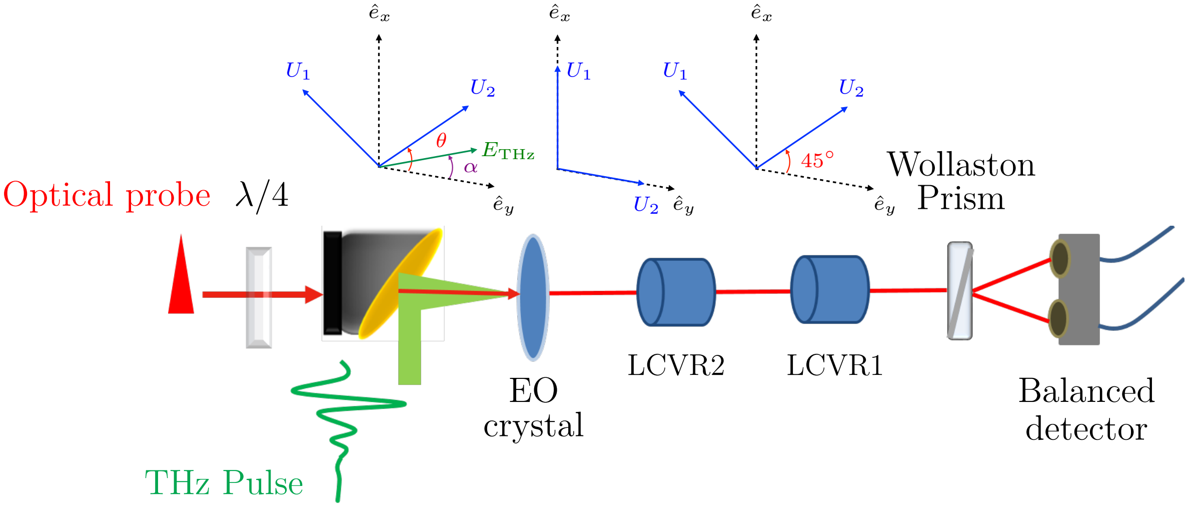

Figure 1.6: Sketch diagram of the THz detection system with a polarization state analyzer (PCA), composed of two liquid crystal variable retarders and one Wollaston prims. The θ angle specifies the principal axis U_1 and U_2 [27].

crystal variable retarders and one Wollaston prism. However, we need to detect four measurements, considering that only the total intensity S_0 is observable in the Stokes vector and a 4 × 4 Mueller matrix will be formed by the PSA, where each row comes from the first rows of each of the four different Mueller matrices [73, 79, 80]. The phase delays, as well as the orientations of the liquid crystal variable retarder (LCVR), are known, the S_{THz} can be obtained directly from a matrix inversion using the following equation:

$$S_{\text{detection}} = \begin{pmatrix} I_0 \\ I_1 \\ I_2 \\ I_3 \end{pmatrix} = \mathbb{M}_{\text{measure}} \cdot S_{\text{THz}} \qquad \Rightarrow \qquad S_{\text{THz}} = \mathbb{M}^{-1}_{\text{measure}} \cdot S_{\text{detection}}. \tag{1.8}$$

One important aspect that we have to consider is that we have to minimize the condition number of this matrix so that the matrix inverse is accurate and not be affected significantly by any experimental error. Hence, we need two LCVRs to generate four independent Stokes vectors that can form a regular tetrahedron on the Poincaré sphere [79, 80]. In fact, we can input any angle between the orientations of the principal axis U_1 and U_2, but for simplicity and to relax the calibration procedure, we choose them to be 45° and 0°. The combination of the four phase delays for LCVR1 and LCVR2, should give the minimum condition number equal to $\sqrt{2}$, to separate them in the Poincare sphere as independently as possible. To generate the measurement matrix $\mathbb{M}_{\text{measure}}$, the four groups of phase delays we use for LCVR1 and LCVR2 are (91.4°, 92.3°), (-20°, 108°), (207.6°, 126°) and (63.3°, –19.6°) [27]. Using this powerful novel technique comprised of LCVRs, it is possible to measure the complete polarization of the probe beam without optical elements or any mechanical rotation.

1.3 THz time–domain spectroscopy

As mentioned at the begging of this chapter, THz–TDS is an extremely powerful and convenient technique for studying a material's dielectric properties. Figure 1.7 shows a common THz–TDS setup diagram with a ZnTe nonlinear crystal source. As shown in the diagram, the optical laser beam is divided by two after the beam splitter: one beam is used for the THz generation and another one for the THz detection. In Section 1.1 and Section 1.2, we discussed different methods for THz generation and detection, respectively. Here, one or two off–axis mirrors are settled to collect the generated THz beam and focus it on the studied sample. Then, to keep collected and focused the THz beam in the detection crystal, a second set of off–axis mirrors is used. Nonlinear THz measurements can be performed by tuning the incidence THz intensity with a pair of wire–grid polarizers or vary the bias voltage on an iLAPCA THz source.

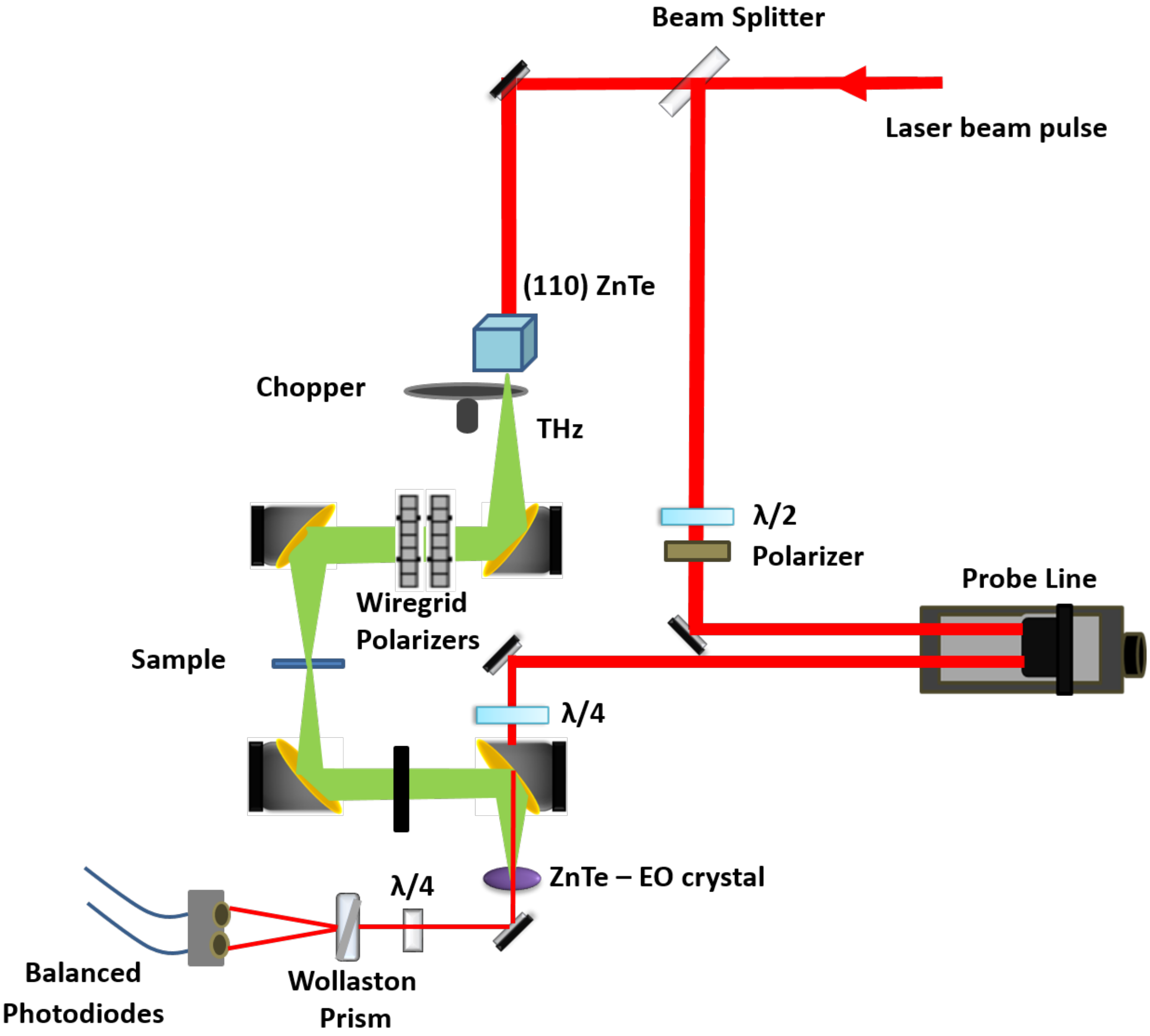
Beam Splitter
Laser beam pulse
(110) ZnTe
Chopper
THz
λ/2
Polarizer
Probe Line
Wiregrid
Polarizers
Sample
λ/4
ZnTe – EO crystal
λ/4
Balanced
Photodiodes
Wollaston
Prism

Figure 1.7: Schematic diagram of a THz–TDS setup.

For studying a sample using the THz–TDS technique, we need to measure (i) the reference waveform measured in air $E_{\text{in.}}(t)$ or with a substrate of known dielectric properties $E_{\text{ref.}}(t)$ and (ii) the transmitted waveform, which is measured after transmission through the entered sample. In this work, we will only focus on the substrate/thin–film/air configuration, where a thin–film conducting layer is deposited on a semi–insulating substrate.

1.3.1 Transmission thin–film theory

In this section, we will find the general expression that describes an incident electric field that is transmitted though sample that has a thin–film conducting layer deposited on a substrate. For this, it is necessary to use the Fresnel's equations which denote the relationship between the amplitudes of the incident, reflected and transmitted waves. Reference [81] and [82] fully detail the derivation of the amplitude reflection and transmission coefficients which are going to be used in section in order to find the transmitted electric field.

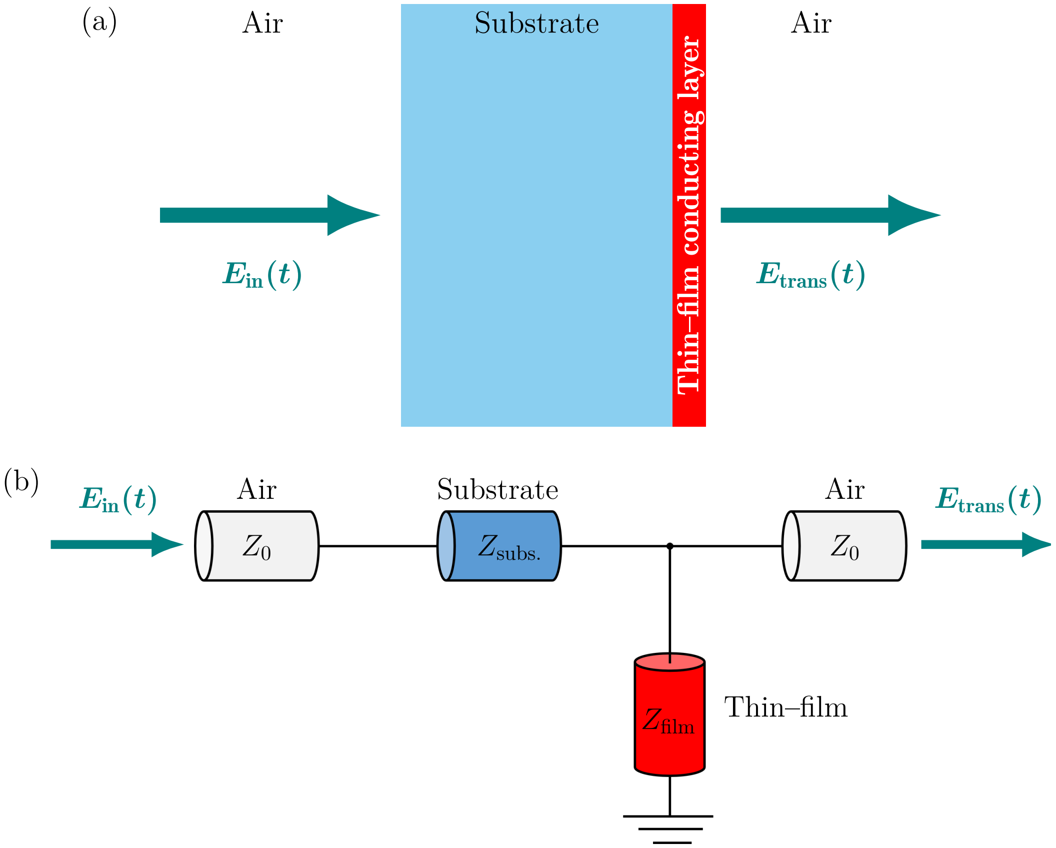

Figure 1.8: Normal incidence and transmission of THz electric field through a thin conducting film layer. (a) Substrate / thin–film / air configuration diagram. (b) Sketch of an impedance diagram where Z_0, $Z_{\text{subs.}}$ and Z_{film} represent the impedance of the free–space, substrate and thin–film, respectively.

The general expression for impedance Z is defined as the ratio between the magnitude of $\mathbf{E}$ and $\mathbf{H}$ field vectors, this is

$$Z = \frac{|\mathbf{E}|}{|\mathbf{H}|} = \sqrt{\frac{\mu\mu_0}{\epsilon\epsilon_0}} = \mu\mu_0 \frac{1}{\sqrt{\epsilon\mu\epsilon_0\mu_0}} = \mu\mu_0 \frac{c}{n},$$

where c is the speed of light, n is the index of refraction, ϵ is the dielectric function of the material, μ is the magnetic permeability of the material, and ϵ_0 and μ_0 are the permittivity and permeability constants in free–space, respectively. The admittance Y is denoted as the inverse of the impedance

$$Y = \frac{1}{Z},$$

where the free–space admittance is given by

$$Y_0 = \frac{1}{Z_0} = \sqrt{\frac{\epsilon_0}{\mu_0}} = \frac{1}{377\,\Omega}.$$

where Z_0 is the free–space impedance. When an incident magnetic field is perpendicular to the plane of incidence and parallel to the interface, the boundary conditions set the tangential components of the magnetic field to be continuous [72, 81, 82]. Using the Fresnel's equations of transmission of light by two films, the amplitude transmission coefficient from the light propagating from medium 1 to 2 is given by

$$t_{\parallel,1\to2} = \left(\frac{E_{0,1t}}{E_{0,1i}}\right)_{\parallel} = \frac{2n_1\cos\theta_1}{n_1\cos\theta_2 + n_2\cos\theta_1},$$

and at normal incidence,

$$t_{\parallel,1\to2} = \frac{2n_1}{n_1+n_2}. \tag{1.9}$$

where n_1 and n_2 are the index of refraction of the first and second medium, respectively. Then, the corresponding Fresnel amplitude coefficients for transmission are

$$t_{\parallel,2\to3} = \frac{2n_2}{n_2+n_3}. \tag{1.10}$$

for the propagation of light from medium 2 to 3, where n_3 is the index of refraction of the third medium. For all the cases, we are considering that the material is dielectric so that $\mu_1 \approx \mu_2 \approx \mu_3$, hence from the definition of impedance we have that

$$n = \frac{Z_0}{Z_{\text{medium}}},$$

therefore

$$\tilde{t}_{\parallel,1\to2} = \frac{2\frac{Z_0}{Z_1}}{\frac{Z_0}{Z_1}+\frac{Z_0}{Z_2}} = \frac{2Z_2}{Z_1+Z_2} = \frac{2Y_1}{Y_1+Y_2}, \tag{1.11}$$

$$\tilde{t}_{\parallel,2\to3} = \frac{2\frac{Z_0}{Z_2}}{\frac{Z_0}{Z_2}+\frac{Z_0}{Z_3}} = \frac{2Z_3}{Z_2+Z_3} = \frac{2Y_2}{Y_2+Y_3}. \tag{1.12}$$

A thin–film's impedance is inversely proportional to its material conductivity and thickness [1], thus

$$Z_{\text{film}} = \frac{1}{\sigma d}, \tag{1.13}$$

where d is the thickness of the thin–film layer and $\sigma = \sigma_1 + i\sigma_2$ is the bulk conductivity. Figure 1.8(a) shows that the incident electric field first irradiates the substrate side with impedance $Z_{\text{subs.}}$ and then the thin–film layer with impedance Z_{film}. The substrate/thin–film/air configuration can be thought as a circuit system [see Fig. 1.8(b)], where the load impedance is formed by adding the film and the free–space impedance in parallel, hence

$$\frac{1}{Z_{\text{load}}} = \frac{1}{Z_{\text{film}}} + \frac{1}{Z_0}. \tag{1.14}$$

In this equivalent circuit system, the amplitude transmission coefficient from medium 1 to 2 is given by

$$\tilde{t}_{\parallel,1\to2} = \frac{2Z_{\text{subs.}}}{Z_0 + Z_{\text{subs.}}} = \frac{\frac{2Z_0}{N}}{Z_0 + \frac{Z_0}{N}} = \frac{2}{N+1},$$

where N is the index of refraction of the substrate. Then, from medium 2 to 3 we have that

$$\begin{aligned}
\tilde{t}_{\parallel,2\to3} &= \frac{2Z_{\text{load}}}{Z_{\text{subs.}} + Z_{\text{load}}} \\
&= \frac{2\dfrac{Z_0 Z_{\text{film}}}{Z_{\text{film}} + Z_0}}{Z_{\text{subs.}} + \dfrac{Z_0 Z_{\text{film}}}{Z_{\text{film}} + Z_0}} \\
&= \frac{2Z_0 Z_{\text{film}}}{Z_{\text{film}} Z_{\text{subs.}} + Z_0 Z_{\text{subs.}} + Z_0 Z_{\text{film}}} \\
&= \frac{2Z_{\text{film}}}{\dfrac{Z_{\text{film}}}{N} + Z_{\text{subs.}} + Z_{\text{film}}} \\
&= \frac{\dfrac{2N}{\sigma d}}{\dfrac{1}{\sigma d} + Z_0 + \dfrac{N}{\sigma d}} \\
&= \frac{\dfrac{2N}{\sigma d}}{1 + \dfrac{\sigma d}{Y_0} + N} \\
&= \frac{2Y_0 N}{Y_0 + Y_0 N + \sigma d}.
\end{aligned}$$

Hence, the electric field that passes through the substrate and then to the thin–film and finally on air, is

$$\mathbf{E}_{\text{trans.}} = \tilde{t}_{\parallel,1\to2}\tilde{t}_{\parallel,2\to3}\mathbf{E}_{\text{in.}} = \left(\frac{2}{N+1}\right)\left(\frac{2Y_0 N}{Y_0 + Y_0 N + \sigma d}\right)\mathbf{E}_{\text{in.}}. \tag{1.15}$$

From Drude model we know that $\mathbf{J} = \sigma\mathbf{E}$ [28, 29], hence we can rewrite eq. (1.15) as

$$\mathbf{E}_{\text{trans.}} = \frac{1}{Y_0 + Y_S}\left[\frac{4Y_S}{N+1}\mathbf{E}_{\text{in.}} - \mathbf{J}d\right], \tag{1.16}$$

where $Y_S = NY_0$ is the admittance of the substrate. The equation (1.16) is known as the thin–film transmission equation. In Chapter 3, we will apply this equation to study the response of a classical n–doped semiconductor $\text{In}_{0.57}\text{Ga}_{0.43}\text{As}$ thin–film when it is pumped by multi–cycle THz pulse.

1.3.2 Previous THz spectroscopy results of n–doped InGaAs thin films

Although ultrafast nonlinear processes have been widely researched in the visible and NIR region [83], one spectral region of the electromagnetic spectrum that has remained largely unexplored is the THz regime, due to a lack of sources capable to provide high–energy and few–cycle THz pulses

[84]. However, these sources are commonly becoming more available [1, 2, 47, 85, 86], allowing the scientific community to investigate unique and fascinating aspects of THz radiation–matter interaction. In this section, we will summarize relevant nonlinear THz experiments performed using an intense THz source. We will describe the nonlinear bleaching of absorption effect induced by intense THz pulses, the high–frequency THz generation from the fast current truncation induced by an intense half–cycle THz pulse, and the effective–mass anisotropy of energetic electrons in an isotropic, nonparabolic conduction band of n–doped InGaAs thin films.

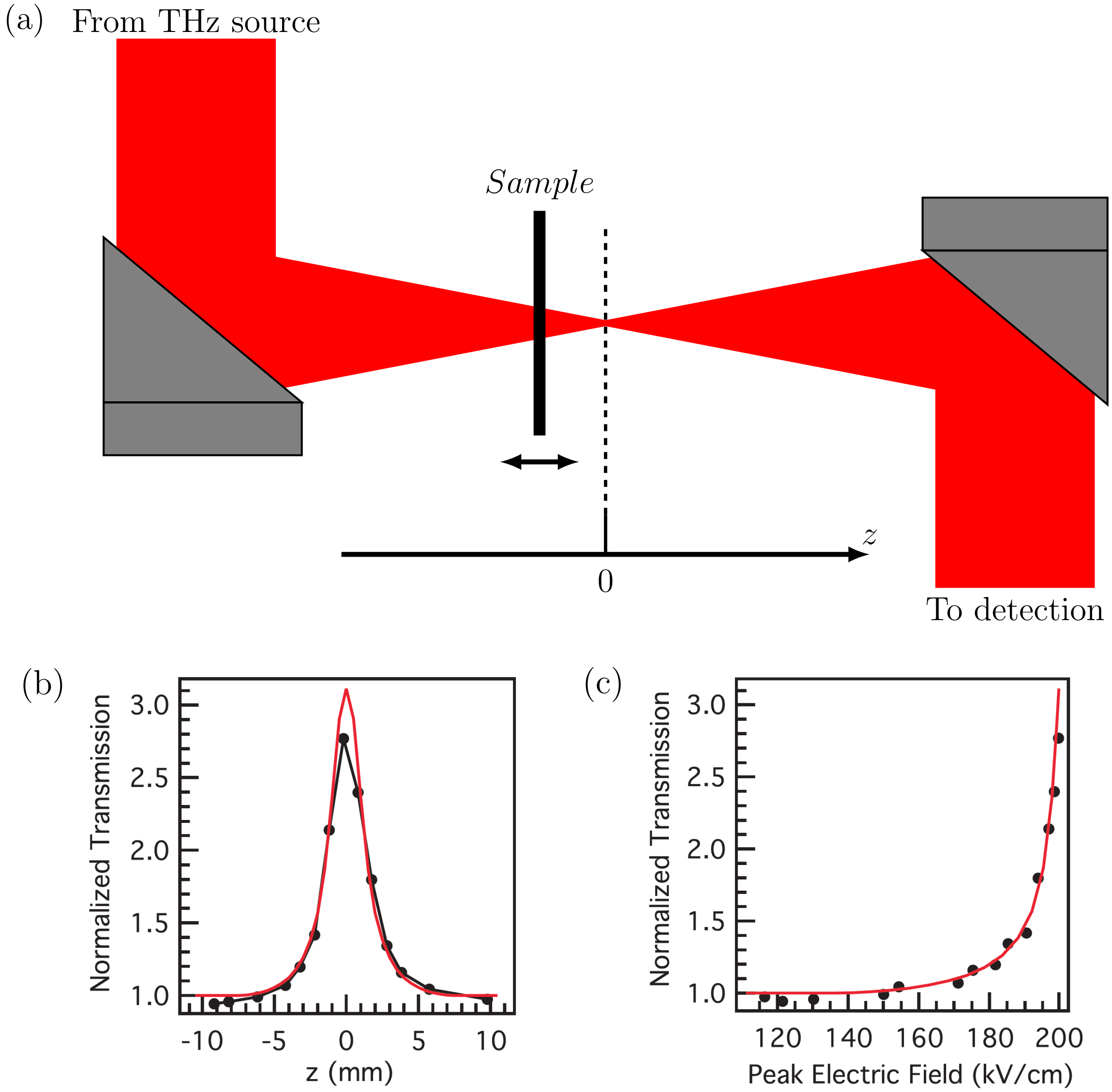

Figure 1.9: Z scan theoretical and experimental results. (a) Schematic diagram of the Z scan experimental setup. (b) Calculated (solid red line) and measured (solid black line) normalized electric field differential transmission as a function of time for different z positions along the scan. (c) Incident electric field dependence of the normalized energy transmission. Courtesy of L. Razzari [17].

The nonlinear bleaching of absorption effect induced by an intense few–cycle THz pulse in an n–doped semiconductor, was studied by Razzari *et al.* (2009) using the common open–aperture Z scan technique, which is a nonlinear optical method for characterizing and investigating nonlinearities [17]. This method involves scanning the sample in transmission mode [see Fig. 1.9(a)], where a powerful laser beam is focused and transmitted through a sample, revealing nonlinear transmission properties. Here, the authors used a sample where an n–type $In_{0.53}Ga_{0.47}As$ epilayer was grown on a 0.5–mm–thick semi–insulating InP substrate. The thickness of the thin-film conducting layer was 500 nm, with a doping concentration of approximately 2×10^{18} cm^{-3}. Moreover, a simple mathematical approach based on the Drudel model was used in order to fit and explain the experimental results. Figure 1.9(b) describes the rapid transmission change along the Z scan and by plotting the normalized transmission as a function of the estimated incident field strengths along the Z scan, Razzari *et al.* demonstrate that a highly nonlinear process is happening [see Fig. 1.9(c)]. The authors conclude that these theoretical and experimental results, for both the Z scan and THz–TDS, prove that the intervalley scattering mechanism is responsible for the observed nonlinear effects.

A current experimental technique that probes the nonlinear carrier dynamics induced by intense few–cycle THz pulses in semiconductors, is the THz–pump–THz–probe (TPTP) technique [87–89]. Blanchard *et al.* developed a polarization–dependent TPTP experiment [9], where initially a strong THz–pump pulse will accelerate the electrons in the x direction and then another weaker polarized THz pulse will be probed in either x (colinear, CL) or y (cross–linear, XL) direction [see Fig. 1.10(a)]. Here, the $In_{0.53}Ga_{0.47}As$ sample that was used is identical to the one that was previous studied by Razzari *et al.* [17].

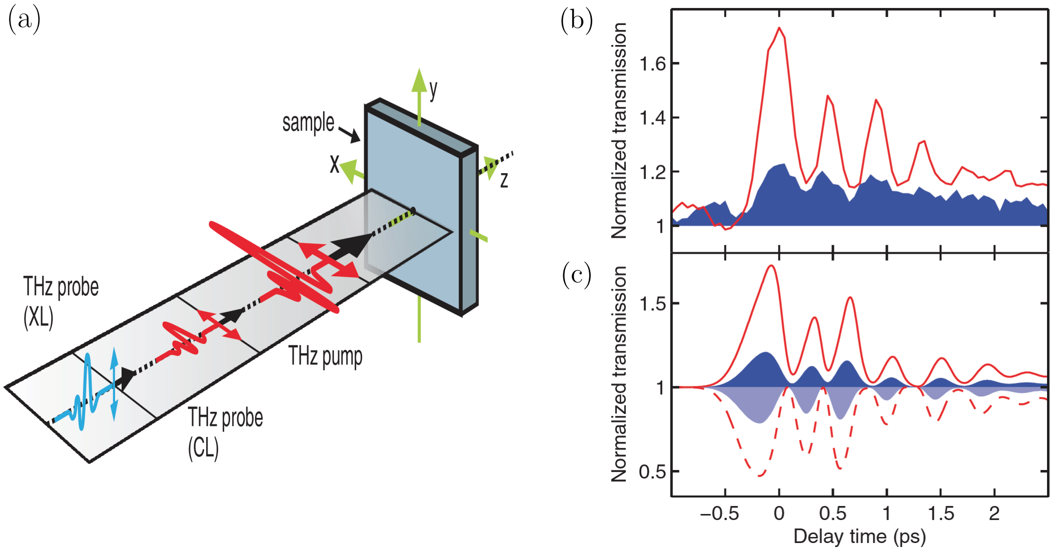

Figure 1.10: (a) Polarization–dependent TPTP configuration. The normalized peak transmission of the THz–probe pulse as a function of the pump–probe delay time were (b) experimentally measured and (c) theoretically calculated. The findings for CL and XL TPTP configurations are represented by solid red lines and blue shaded regions, respectively. In (c), the dashed red line and light–blue shaded region show the calculations where the radiative back–coupling effects are omitted. Courtesy of F. Blanchard [9].

The measured and calculated transmission change for XL polarizations of the pump and probe beams is shown in figures 1.10(b) and 1.10(c) with a blue shaded area, respectively, and the red line represents the same measurements for CL polarizations. The computed transmission change shows that the CL case has a considerably greater amplitude oscillation than the XL case, revealing that the TPTP method can indeed analyze the mass anisotropy. This new technique allows the authors to demonstrate the effective–mass anisotropy of energetic electrons in an isotropic and nonparabolic conduction band of n–doped InGaAs thin–films.

It has been shown that by using an iLAPCA for THz generation, it is possible to reach the regime of sub–cycle THz nonlinear optics [38, 90, 91]. Chai *et al.* performed nonlinear THz–TDS experiments in the same n–doped InGaAs thin film [18], using a quasi–half–cycle THz pulse with a fundamental frequency of less than 0.2 THz [see Fig. 1.11(a)], demonstrating the high–frequency THz generation from the fast current truncation induced by an intense half–cycle THz pulse [see Fig. 1.11(b)]. The authors attribute this drastic current decrease to strong intervalley scattering effects. Moreover, Chai and co–workers show that it is possible to monitor the evolution of the nonlinear carrier dynamics during a quasi–single–cycle pulse by adding an additional half–cycle terahertz pulse with opposite polarity [see Fig. 1.11(c)].

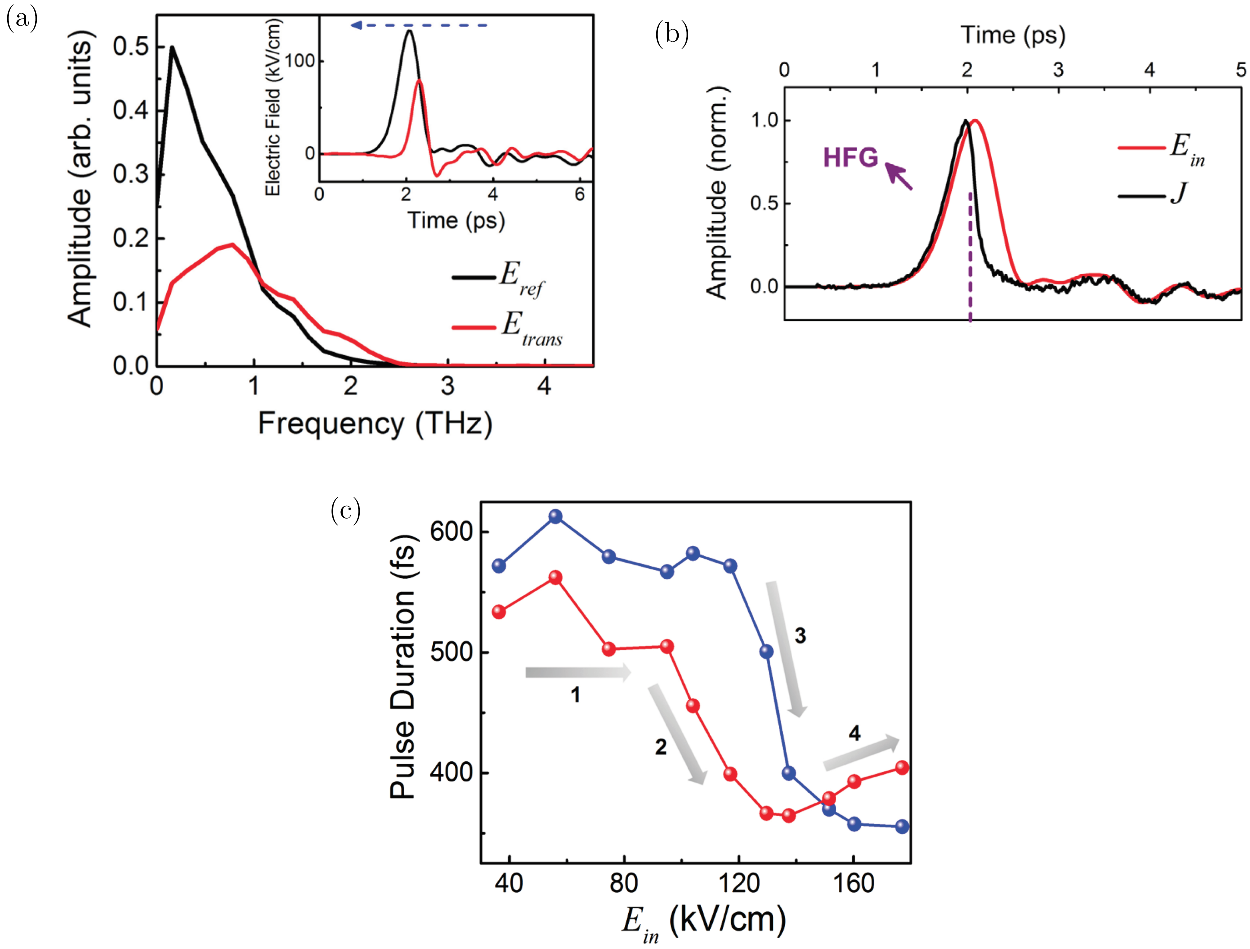

Figure 1.11: Sub–cycle THz nonlinear experiments. (a) Amplitude spectra of the incident (E_{ref}) and transmitted (E_{trans}) terahertz pulses, with an incident peak field of 190 kV/cm. Inset: corresponding incident and transmitted terahertz waveforms where propagation direction indicated by the blue arrow. (b) Incident terahertz waveform and the calculated current density with the field strength of 190 kV/cm. From ~1.0 THz up to 2.5 THz, we found high–frequency generation (HFG) with spectral amplitude enhancement. (c) Field dependence of half–cycle durations. Four field regions can be identified, representing: 1, the linear regime; 2, current truncation on the negative polarity; 3, current truncation on the positive polarity; and 4, pulse broadening of the negative polarity. The dotted blue (red) line represents the incident field strength of positive (negative) polarity. Courtesy of X. Chai [18].

1.4 Intense THz–matter interaction and nonlinear THz effects

Owing to the rapid advancements in intense terahertz (THz) radiation sources, there have recently been significant breakthroughs in our understanding of intense THz–matter interactions and nonlinear THz effects [16–18, 23, 44–46]. For example, several theoretical and experimental studies have shown efficient THz frequency multiplication, such as high–order sideband generation (HSG) [21, 22] and high–order THz harmonic generation [19–22, 54, 92, 93] using intense multi–cycle THz pulses transmitted through various materials. These materials include bulk crystals, such as gallium selenide (interpreted via dynamical Bloch oscillations) [20, 54], tungsten diselenide (modelled by THz–driven electron–hole collisions) [21, 22] and graphene (explained via the interplay between the interband and intraband motion of the carriers and hot Dirac fermion dynamics) [19, 92, 93].

1.4.1 High–order sideband generation

One extremely nonlinear optical effect in the THz regime is the high–order sideband generation (HSG), where two light frequencies are used: near–infrared (NIR) light, which is relatively weak, and THz light, which is very strong. Many new frequencies are created when these two frequencies are combined in a high–mobility semiconductor material. These new frequencies, known as sidebands, are spaced twice the THz frequency and around the original NIR laser frequency, or $\nu_{\text{sideband}} = \nu_{\text{NIR}} + 2n\nu_{\text{THz}}$, where n is the number of the spectral components. The theory that explains the HSG is the semi–classical three–step model, originally proposed by Corkum in the context of high–order harmonic generation (HHG) in atoms [94]. The NIR laser, which is tuned to the material's band gap, first creates a bound electron–hole pair. Simultaneously, an extremely strong THz electric field should be applied to warp the electron's Coulomb potential to the point that the electron tunnels away from the hole. Then, within the strong THz field, the electron and hole freely accelerate away from and then back towards each other. Third, the particles recollide again, but this time with more kinetic energy. The sidebands are generated when the particles annihilate and emit a photon with more energy than the initial NIR photon [see Fig. 1.12].

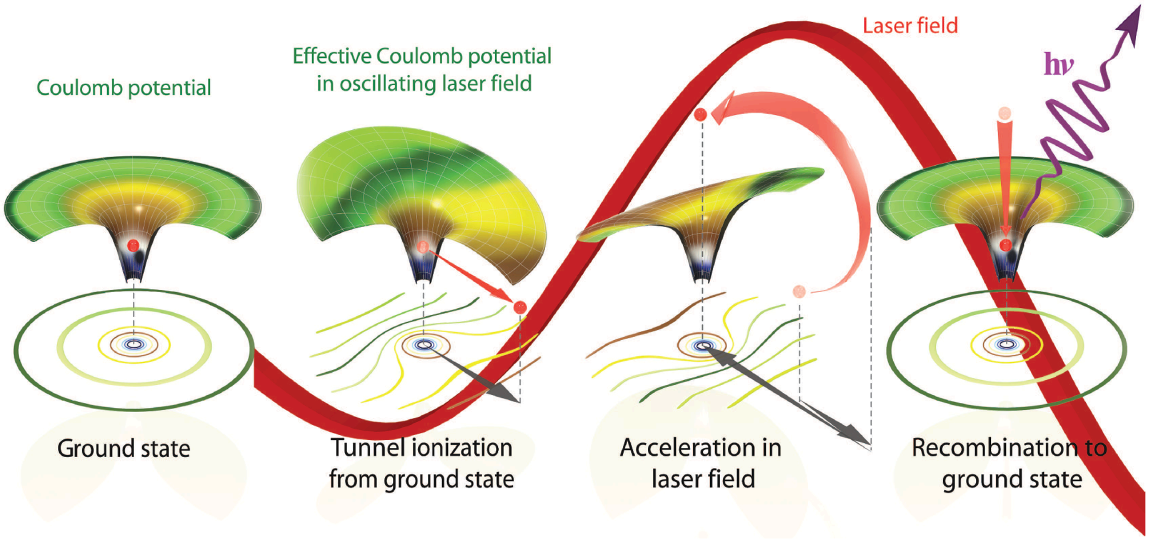
Coulomb potential
Effective Coulomb potential in oscillating laser field
Laser field
hν
Ground state
Tunnel ionization from ground state
Acceleration in laser field
Recombination to ground state

Figure 1.12: Classical schematic diagram of the semi–classical three–step model. The electric field of an intense laser extracts an electron from an atom through tunnel ionization. The laser field then accelerates the electron, with a small fraction of the electron returning back to the ground state of the same atom, liberating its excess energy as a high–energy photon. Figure courtesy of T. Popmintchev *et al.* [95].

Langer *et al.* have observed in WSe_2 that the recolliding electrons and holes emit light via multiple HSG [21, 22]. In this experiment, they used a 100–femtosecond near–infrared excitation pulse (titanium–sapphire laser amplifier with a repetition rate of 3 kHz, pulse energy of 5.5 mJ, pulse duration of 33 fs, and with a wavelength centered at 805 nm) and a high–intensity THz pulse with MV/cm peak electric fields. Moreover, these authors show that quasiparticle collisions can be realized in the time domain, and the generation of ultrabroad sideband emission results as a consequence of coherent electron–hole pairs excited, accelerated, and collided in WSe_2 [see Fig. 1.13].

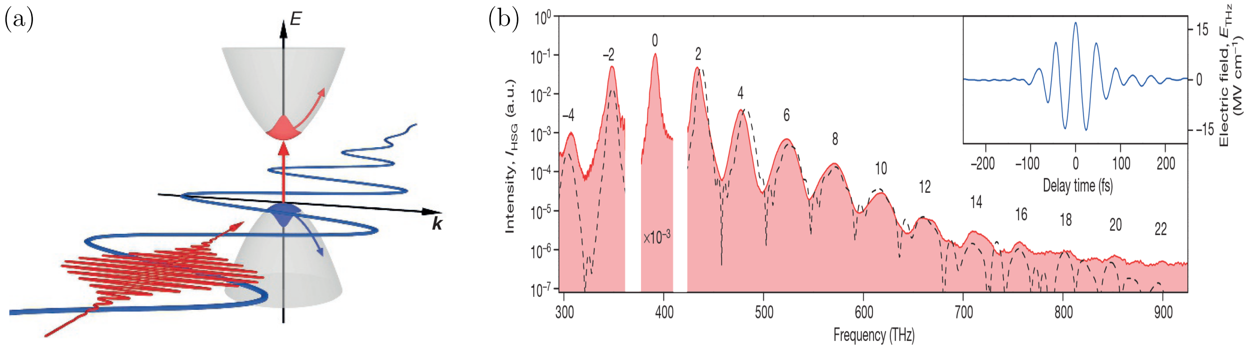

Figure 1.13: (a) Schematic of the experiment in reciprocal space: an interband excitation pulse (red waveform) creates an excitonic polarization in WSe_2 (red, vertical arrow), while a strong multi–THz field (blue waveform) simultaneously accelerates the wave packets of the electron and hole (curved arrows) within their respective bands (grey shaded parabolas). (b) Measured intensity spectrum (red) of high–order sidebands from WSe_2. The black dashed curve shows the calculated intensity spectrum I_{HSG} a.u., arbitrary units. Inset: the driving waveform with a fundamental frequency of 23 THz and external peak field strength of E_{THz} = 17 kV/cm. Figure courtesy of L. Langer *et al.* [21].

1.4.2 High–order THz harmonic generation

As mentioned in the previous section, Corkum proposed a quasistatic model (later named the three–step model) where the ponderomotive energy determines the maximum energy of the electrons responsible for harmonic emission. Hence the high–frequency cutoff of the harmonic radiation depends on the ponderomotive energy. Also, he mentions that the nature of high–harmonic generation is captured by the quasistatic model because the magnitude of the high harmonics agrees within less than an order of magnitude of the calculated harmonic spectrum of the absolute value of the dipole moment squared [94].

Moreover, Hafez *et al.* have reported the generation of THz harmonics via hot Dirac fermion dynamics in a single–layer of graphene, driven by multi–cycle intense THz pulses with peak field strengths of only 100 kV/cm ~ 1 MV/cm [19]. Here, they report the generation of THz harmonics up to the seventh order in a single–layer of graphene, at room temperature and under ambient conditions, using terahertz fields of only a few tens of kilovolts per centimeter and with field conversion efficiencies of more than 10^{-3}, 10^{-4}, and 10^{-5}, for the third, fifth, and seventh terahertz harmonics, respectively [see Fig 1.14]. In addition to the HHG, we can observe new spectral peaks in the transmitted THz spectra with frequencies slightly above and below the fundamental frequency of 0.3 THz [see Fig 1.14(a)]. Nevertheless, as we have seen in the visible and near–infrared regimes, nonlinear effects give rise to a multitude of fascinating phenomena, many of which could still be hiding in experimental data.

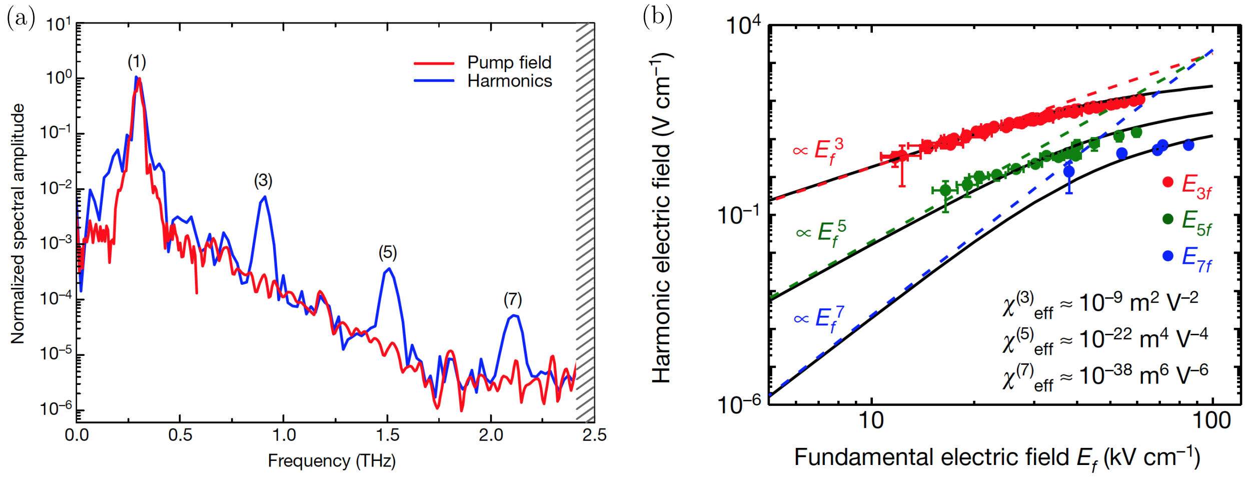

Figure 1.14: (a) The individual higher harmonics were Fourier–filtered from the complete nonlinear signal containing all the generated harmonics at once, where the fundamental pump wave is centered at a frequency of 0.3 THz. (b) Dependence of the generated harmonic field strength on the fundamental pump field strength. Figure courtesy of H. Hassan *et al.* [19].

1.5 Transient carrier dynamics

The absence of an electron in space, known as a hole, can be considered as a positively charged particle that moves across a crystal structure [28–30]. Thus, the excitation of an electron into the conduction band results in an electron in the conduction band and a hole in the valence band. Both electron and hole are known as carriers (electron–hole pair) [see Fig. 1.15]. When a phonon field, external electromagnetic or electric field is applied to a semiconductor, free carriers can be generated, resulting in photo– or semi–conductivity. However, the generation of carriers can also be achieved by high–energy particles, such as fast electrons or ions.

There are three different types of carrier generation processes, where each process requires energy provided by one of the following forms: thermally (via a phonon field), optically (via an electromagnetic field) and electrically (via an electric field). However, the carriers can also have a recombination process. Each of the two types of recombination processes releases energy in one of the following ways: thermal energy (via nonradiative recombination) and luminescence (via radiative recombination). Hence to determine the density of carriers in semiconductors, we have to consider the difference between the generation rate g_n and the recombination rate r_n, and the divergence of the current density, which represents the net influx of carriers from surrounding regions, thus

$$\frac{dn(\mathbf{r})}{dt} = g_n - r_n + \frac{1}{e}\frac{\partial \mathbf{j}_n}{\partial \mathbf{r}}.$$

In this work, we will detail and focus on the carrier generation process where an external electric field is applied to a semiconductor. On the one hand, in the presence of low electric fields (~ 10^3 V/cm), the Frenkel–Poole effect [1] results in the generation of carriers due to the field–enhanced thermal disorder between Coulomb–attractive centers. On the other hand, impact ionization from deep centers or band–to–band impact ionization occurs at high electric fields (~ 10^6 V/cm) [30, 96].

Additionally, the calculation of conductivity or the current density of a semiconductor can be carried out using the Boltzmann transport equation, accounting for both the valence and conduction

Figure 1.15: Generation of electron–hole pairs (carriers) in semiconductors. The red and white circles represent the electrons and holes, respectively.

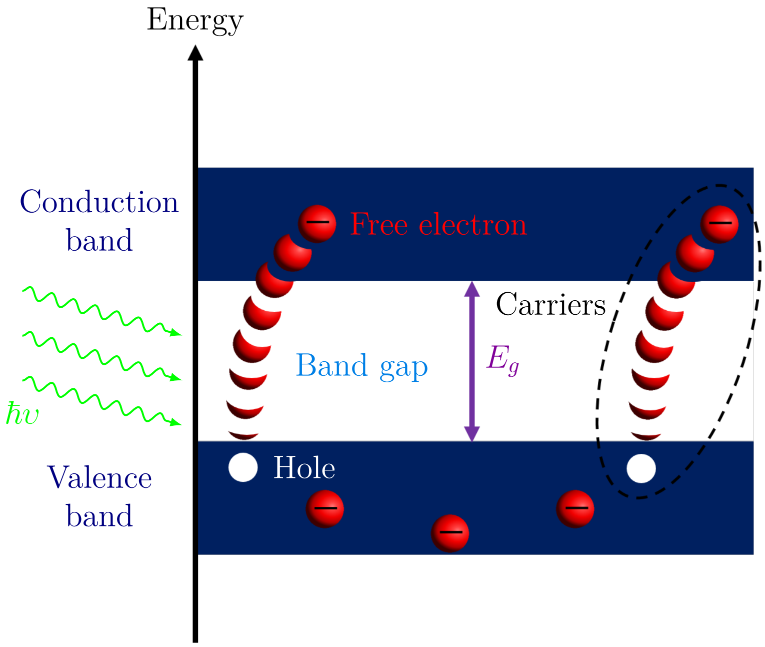

band contributions. The Boltzmann transport equation is a general kinetic equation that provides a precise basis for the characterization of both energy and space distribution functions [28–30]. First, we need to find an equation of motion for a phase space distribution function in the presence of an applied force to the electrons. With this, we can characterize the behavior of the particles to long–range collective forces. Then, to describe the carrier transport, we consider the contribution of the approximated short–range collisional forces. In the end, we will know how the Fermi sea shifts in response to those forces, and we will be able to calculate quantities like the current density. However, the Boltzmann transport equation is a complicated integro–differential equation that cannot be solved easily, and thus we implement an analytical–band ensemble Monte–Carlo approach to solve it numerically [18, 31–37]. The ensemble Monte–Carlo method is a statistical numerical method used to derive physical information from simulated experiments. With this method we can simulate random processes by modeling the distribution functions of particles by tracking the actual movement of each particle. Multiple authors have published in scientific articles different types of Monte–Carlo methods to solve specific transport problems [97–100]. In the following chapter we will discuss and show the relevant and important points of the Monte–Carlo method that we implement to study and understand transient carrier dynamics and nonlinear THz effects.

1.5.1 Semiconductor physics

Materials with full bands, separated by an energy or band gap (E_g) from empty bands, are known as semiconductors or insulators. In semiconductors, the chemical potential lies within the energy gap separating the full from empty states. Materials with a smaller energy gap are considered as semiconductors, and those with larger ones are generally insulators. Moreover, a semiconductor has an electrical conductivity between a metal and an insulator. The properties of semiconductors depend strongly on the energy gap (typically in the range of ~eV), temperature and impurities [28–30].

Historically, the first property of a semiconductor in the literature was reported by Seebeck for lead sulfide in 1822 [101] and then by Faraday in 1833, for silver sulfide [102]. Nevertheless, the term “semiconductor” was introduced in 1911 by Königsberger and Weiss [103], but according to the author G. Busch [104], Alessandro Volta used for the first time the term “semiconducting” in 1782 [105]. In 1851, Hittorf published a paper with an extensive quantitative analysis on the semi–logarithmic dependence of the electric conductivity σ of Ag_2S and Cu_2S on 1/T (where T is the temperature) [106]. Moreover, in 1874 Braun discovered the semiconductor point–contact effect by doing a point of contact between metal sulfides and certain crystal materials, creating a rectification effect [107]. Based on this observation, the first application of semiconductors in a device was demonstrated at the beginning of the twentieth century: the cat's whisker detector. In 1947 at Bell Labs, William Schockley, John Bardeen, and Walter Brattain created the first transistor by sandwiching two diodes together, and this invention could be considered the birth of modern electronics [108].

Semiconductors are hugely useful for device applications because they have two kinds of charge carriers with opposite signs and the densities of the charge carriers can be tuned by doping, including spatial variations in dopant concentration. Thus, we can take advantage of this with inhomogeneous semiconductors, where N_A^- and N_D^+ vary with position[1]. The simplest example of this is the so–called $p-n$ junction, where n–type (donor doped) and p–type (acceptor doped) regions are in close proximity [28, 29]. With an incredibly wide variety of uses, including high–speed networking, computing, and artificial intelligence, semiconductors have become a fundamental component of modern society's technology [109–111].

1.6 Justification, main objective and structure of the thesis

The interaction of intense, few–cycle THz pulses with matter and the observation of nonlinear THz effects have recently attracted considerable attention from the scientific community [16–18, 23, 43–46]. Such studies greatly benefit from a unique aspect of THz spectroscopy, that is, coherent generation and detection combined with the pump–probe technique, which allows time–resolved THz electric field measurements [1, 2, 9].

The study of transient carrier dynamics and nonlinear terahertz effects induced by an intense multi–cycle terahertz pulse in an n–doped semiconductor $In_{0.57}Ga_{0.43}As$ is the main objective of this dissertation. The general idea is to simulate and implement an analytical–band ensemble Monte–Carlo approach to solve the Boltzmann transport equation. A necessary task would be to demonstrate and explain the mechanisms of high–order harmonic (HH) emission and the generation of low– and high–frequency components (LFC & HFC) beside the central frequency of intense THz pulses in the n–doped semiconductor. Another related task would be to clarify the spectro–temporal structure of HHs and show that both inter– and intra–valley effects lead to their generation, while LFC & HFC are due to purely intravalley effects. Thus, as evidenced with nonlinear optics such nonlinear THz effects could have numerous potential applications, such as in the reconstruction of the band structure [112, 113], being of significant interest to the broad scientific community in physics, chemistry and material science [114–117].

This dissertation is divided as follows: in Chapter 2, we mention the principal scattering mechanism in a semiconductor. We also discuss the background theory and derivation behind the Boltzmann transport equation. We have emphasized that in our model, the equation needs to be solved numerically, and thus we present and detail the Monte–Carlo method used in this dissertation. In this Chapter, we also explain the numerical method process applied to the governing equations in order to compute the distribution functions, drift velocity and current density. Chapter 3 shows the simulation results of the transient carrier dynamics and the nonlinear THz effects induced by an intense multi–cycle THz pulse. For a multi–cycle pulse, we generate a distorted biphasic truncated exponential current with the driving THz fields, leading to discrete HHG in the transmitted intensity spectra. For incident THz pulses with relatively high frequency ≥ 1 THz, we reveal the generation of LFC & HFC in the spectra. Additionally, we study the time emission of these components at different frequencies using the Gábor transform, showing that the LFC & HFC are due to intravalley effects. The thesis concludes with Chapter 4, reviewing the main outcome contributions of the dissertation.

---

[1] N_A^- and N_D^+ are the number of ionized acceptors (negatively charged cores) and donors (positively charged cores), respectively.

At the beginning of this document, a list of abbreviations and symbols is included, defining the convention used in this work.

Chapter 2

Carrier–Transport Equations

The electrons and holes in the conduction and valence bands have a quasi–free movement in space and energy and can obtain energy from an external field. The carrier transport in semiconductors with crystal or lattice defects (impurities) and lattice vibrations (phonons), is subject to scattering with a mean free path λ between scattering events [30]. The interaction of the electrons that interplay with the lattice imperfections, such as impurities, optical or acoustic phonons, photon emissions, etc., is denominated as a scattering event. Every scattering event that occurs changes the carrier momentum and motion. Nevertheless, few scattering events, such as inelastic scattering, optical phonons and intervalley scattering, can drastically change the energy of the carrier. Typically, after the carrier has received sufficient energy from the field to permit inelastic scattering, multiple elastic scattering events are followed by one inelastic event [30, 32, 37].

2.1 Phonon scattering

Phonons are lattice vibrations as photons are to electromagnetic waves. They represent the quantized excitation of the lattice motion. Indeed, the number of phonons rises at higher temperatures and thus increases the scattering rate, reducing its mobility. The scattering of either optical and acoustic phonons can be absorptive or emissive.

2.2 Intravalley scattering

Intravalley scattering is a process where the initial and final state of a carrier is inside the same valley. Semiconductors have both phonon and impurity scattering, where just long–wavelength phonons (acoustic phonons) are involved, which are those with wave–vectors near the center of the Brillouin zone [32, 118].

2.2.1 Intravalley acoustic phonon scattering

An approximate value of the velocity of acoustic phonons with wave–vectors near the zone center is $\omega/\beta = v_s$, where β is the magnitude of the momentum vector of the phonon and v_s is the speed of sound. Since for a thermal average carrier, the thermal velocity is $v_{\text{th}} \approx 10^7$ cm/s and $v_s \approx 10^5$ cm/s, then

$$\hbar\beta_{\max} \approx 2k,$$

for a general acoustic phonon scattering event, where k is the magnitude of the wave–vector. This tells us that acoustic phonon scattering is nearly elastic. To measure the magnitude of $\beta_{\max}$, we need to compare it with the approximate half–width of the Brillouin zone π/a, this is

$$\frac{\beta_{\text{max}}}{\frac{\pi}{a}} = \frac{2m^* v_{\text{th}}}{\hbar\frac{\pi}{a}} \approx \frac{1}{4},$$

where the effective mass is equal to the free electron rest mass and $a = 5$Å. Hence, we can conclude that acoustic phonon scattering involves phonons with wave–vectors near the center of the Brillouin zone [32].

2.2.2 Intravalley optical phonon scattering

For optical phonons, the dispersion relation can be approximated as $\omega(\beta) = \omega_0$, where ω_0 is constant. The energy of optical phonons is generally tens of meV, which is reasonably comparable with the thermal energy, and thus they can hardly be considered as elastic. The maximum wave–vector of an optical phonon is

$$\hbar\beta_{\text{max}} = k\left[1 + \sqrt{1 \pm \frac{\hbar\omega_0}{E(k)}}\right],$$

and when we compute typical values in this last equation [32], we obtain that optical phonons near the center of the Brillouin zone contribute to intravalley scattering.

2.3 Intervallley scattering

Intervalley scattering involves the excitation of carriers directly into the satellite valleys, which can be either optical or acoustic phonons. Usually, the phonon momentum is large and nearly constant, and hence the intervalley phonon energy $\hbar\omega_{ij}$ can also be assumed as constant. The large changes in the momentum imply phonons with wave–vectors near the zone boundary [32, 118].

To model intervalley scattering, the crystal momentum needs to be conserved, which requires that the wave–vector $\mathbf{k} \approx \Delta\mathbf{q}$, where $\mathbf{q}$ is the vector that joins the two minimums of the valley. Then we can assume an interaction potential given by

$$U_{\text{Inter.}} = D_{ij}u(x,t),$$

where $u(x,t)$ is a displacement function and D_{ij} is the intervalley deformation potential and characterizes the strength of the scattering from the initial valley i to the final valley j. Then the energy conservation also includes accounting for the difference in initial and final energy from the valley, giving the total scattering rate for optical deformation potential as

$$W\left(\mathbf{k},\mathbf{k}'\right) = \frac{\pi D_{ij}^2 Z_j}{\rho\omega_{ij}V}\left[\delta\left(E' - E + \Delta E_{ji} + \hbar\omega_{ij}\right)\right](N_i + 1)\left[\delta\left(E' - E + \Delta E_{ji} - \hbar\omega_{ij}\right)\right]N_i\,,$$

where V is the volume of the crystal, Z_j is the number of final valleys available for scattering, ρ is the mass density, N_i is the occupation, and E_{ji} is the energy difference between the bottom of the conduction band in the final and initial valleys [32]

$$\Delta E_{ji} = E_{\text{min.},j} - E_{\text{min.},i}.$$

2.4 Carrier transport in multivalley semiconductors

We list in figure 2.1 the essential scattering mechanisms in a semiconductor that should be considered in a typical computational algorithm that uses the method of repeated random sampling to perform numerical estimations of unknown parameters [30, 32, 37]. The scattering mechanisms are generally divided into: (i) scattering caused by crystal or lattice defects (elastic scattering event), (ii) lattice scattering between electrons/holes and lattice vibrations or phonons (inelastic scattering event) and (iii) scattering between the particles themselves (either inelastic or elastic scattering event) [37].

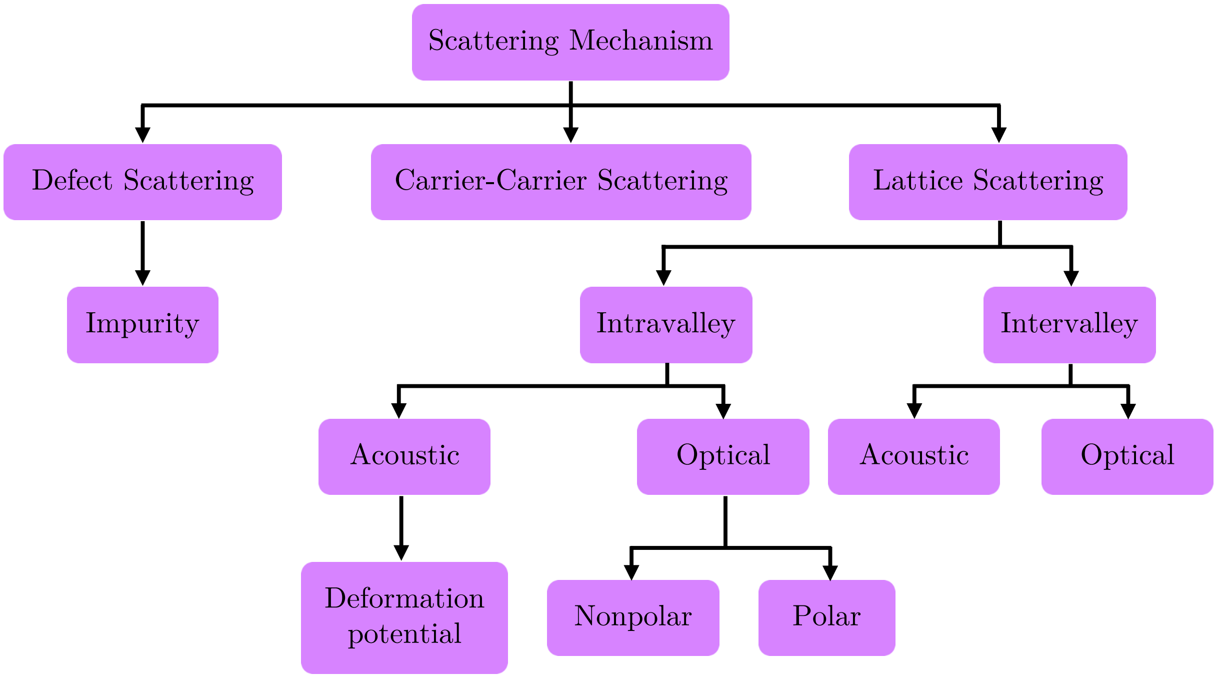

Figure 2.1: Scattering mechanisms in a typical semiconductor.

Direct and indirect band gap semiconductor materials possess multi–satellites valleys with minima at the conduction band edge in different crystallographic directions. As mentioned before, when the scattering of the carriers occurs within one of these satellite valleys, we have intravalley scattering, and when there is scattering from one satellite valley to another, intervalley scattering happens. As an example, figure 2.2 shows the band structure of $In_{0.57}Ga_{0.43}As$, where the lowest satellite valley is the Γ valley. The possible scattering effects that can occur, such as intra– and inter–valley scatterings, are illustrated. The energy separation between the bottom of the Γ valley and the L valley is $\Delta_{\Gamma L} = E_L - E_g = 0.55$ eV, and that between the Γ valley and the X valley is $\Delta_{\Gamma X} = E_X - E_g = 0.67$ eV [119].

To describe the transient carrier dynamics, we need to assume that most of the scattering events are elastic, and all the individual types of collisions must be taken into account. Then, the constant and energy–independent scattering time that exists between the scattering events has to be refined. In semiconductors, a distorted carrier distribution can be approximated by a Boltzmann distribution function within the bands, supposing that the carrier temperature is elevated above the lattice temperature [30]. However, for highly doped semiconductors (doping concentration of ~ 2×10^{24} cm^{-3}), it is important to consider a *Fermi–Dirac* distribution since it considers *Pauli*'s exclusion principle, and *Maxwell–Boltzmann* distribution does not. Therefore, the *Maxwell–Boltzmann* distribution is only valid in the lowly doped (n or p doped) case [30, 32].

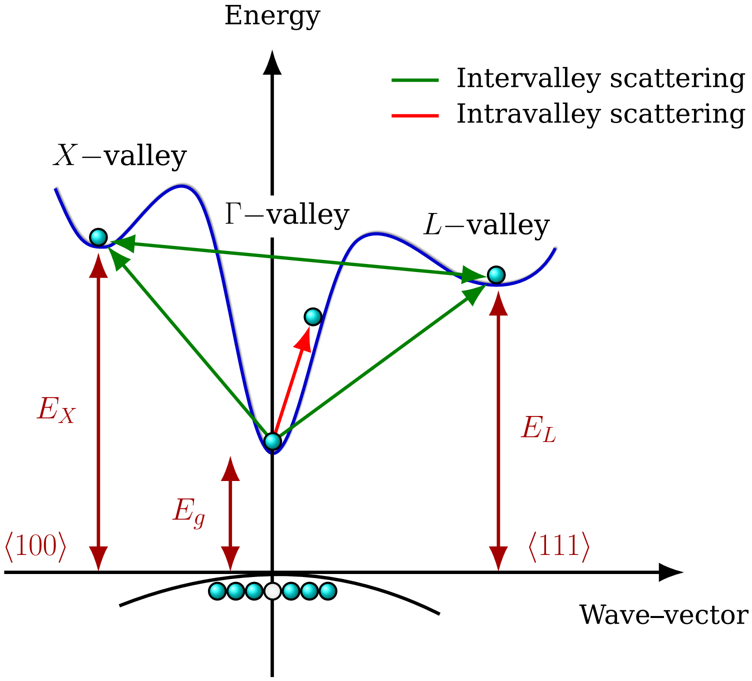

Figure 2.2: A schematic view of In$_{0.57}$Ga$_{0.43}$As band structure [120].

2.5 The Boltzmann transport equation

The Boltzmann transport equation is a general equation that can be used to include and describe the effects of the lattice potential. Here, we need to consider the situations where the applied forces (like an electric field) vary slowly in space, which implies that they are essentially constant over the region of interest. Further, the spatial scales should be large enough to consider the electrons as wavepackets with well–defined positions and wave–vectors. Hence, to examine the probability that a wavepacket at a position $\mathbf{r}$, wave–vector $\mathbf{k}$ and time t is occupied, we define

$$f(x, y, z, k_x, k_y, k_z, t) \coloneqq f(\mathbf{r}, \mathbf{k}, t), \tag{2.1}$$

as the probability that an electron state with position $\mathbf{r}$ and wave–vector $\mathbf{k}$ is occupied at time t. This function is a phase space description of the electron distribution, for example in thermal equilibrium the *Fermi–Dirac* distribution is given by

$$f(\mathbf{r}, \mathbf{k}, t) = f_0(\mathbf{k}) = \frac{1}{e^{\frac{\epsilon(\mathbf{k}) - \epsilon_F}{k_B T}} + 1}.$$

where ϵ_F is the Fermi energy (in semiconductor physics, we often denote the chemical potential μ by ϵ_F). However, the *Maxwell–Boltzmann* distribution is a common approximation of the *Fermi–Dirac* distribution function, where

$$f(\mathbf{r}, \mathbf{k}, t) = f_0(\mathbf{k}) = A e^{\frac{\epsilon_F - \epsilon(\mathbf{k})}{k_B T}}.$$

In fact, what we need to find is an equation of motion for $f(\mathbf{r}, \mathbf{k}, t)$ in the presence of a force applied to the electrons because this will tell us how the Fermi sea shifts in response to forces, and also will allow us to calculate parameters like current density.

Under an applied force $\mathbf{F}$, the wave–vector can be described by the correspondence principle

$$\frac{d\left(\hbar\mathbf{k}\right)}{dt} = \mathbf{F}, \tag{2.2}$$

and the first derivative of position with respect to time gives us the electron's velocity, where for free electrons[1]

$$\frac{d\mathbf{r}}{dt} = \mathbf{v} = \frac{\hbar\mathbf{k}}{m}. \tag{2.3}$$

Hence, in the absence of collisions, an electron at position $\left(\mathbf{r},\mathbf{k}\right)$ and at time t must have been at $\mathbf{r}-\mathbf{v}dt$, $\mathbf{k}-\hbar^{-1}\mathbf{F}dt$ a time dt earlier. Thus, if *no collisions* happen, the equation of motion for $f\left(\mathbf{r},\mathbf{k},t\right)$ is given by

$$f\left(\mathbf{r},\mathbf{k},t\right) = f\left(\mathbf{r}-\mathbf{v}dt,\mathbf{k}-\frac{1}{\hbar}\mathbf{F}dt,t-dt\right),$$

thus, collisions will add a correction to this relation, and the correction will get bigger as dt grows, then

$$f\left(\mathbf{r},\mathbf{k},t\right) = f\left(\mathbf{r}-\mathbf{v}dt,\mathbf{k}-\frac{1}{\hbar}\mathbf{F}dt,t-dt\right) + \left(\frac{\delta f}{\delta t}\right)_{\text{scatt.}} dt.$$

However, if we only consider the first term of a Taylor expansion

$$f\left(\mathbf{r},\mathbf{k},t\right) \approx f\left(\mathbf{r},\mathbf{k},t-dt\right) - \mathbf{v}dt\cdot\nabla_{\mathbf{r}}f - \frac{1}{\hbar}\mathbf{F}dt\cdot\nabla_{\mathbf{k}}f + \left(\frac{\delta f}{\delta t}\right)_{\text{scatt.}} dt,$$

therefore

$$\left(\frac{\delta f}{\delta t}\right)_{\text{scatt.}} = \frac{f\left(\mathbf{r},\mathbf{k},t\right)-f\left(\mathbf{r},\mathbf{k},t-dt\right)}{dt} + \mathbf{v}\cdot\nabla_{\mathbf{r}}f + \frac{1}{\hbar}\mathbf{F}\cdot\nabla_{\mathbf{k}}f$$

or

Boltzmann transport equation

$$\left(\frac{\delta f}{\delta t}\right)_{\text{scatt.}} = \frac{\partial f}{\partial t} + \frac{1}{\hbar}\nabla_{\mathbf{k}}\mathcal{E}\left(\mathbf{k}\right)\cdot\nabla_{\mathbf{r}}f + \frac{-e\mathbf{E}}{\hbar}\cdot\nabla_{\mathbf{k}}f. \tag{2.4}$$

This last equation is known as the *Boltzmann transport equation* [28, 29]. Here, $\left(\frac{\delta f}{\delta t}\right)_{\text{scatt.}} dt$ is the probability of scattering into $\left(\mathbf{r},\mathbf{k}\right)$ minus the probability of scattering out of $\left(\mathbf{r},\mathbf{k}\right)$. In other words, it is the change in the probability of occupying $\left(\mathbf{r},\mathbf{k}\right)$ due to collisions during time dt. For example, suppose that we consider the scattering off of impurities or defects in a crystal, then the Hamiltonian can be written as [121]

$$\mathcal{H} = \mathcal{H}_0 + V_{\text{dir.}}\left(\mathbf{r}\right),$$

where $\mathcal{H}_0$ is the perfect crystal Hamiltonian (one–electron Hamiltonian) and $V_{\text{dir.}}$ is the extra potential energy landscape due to impurities (defect potential). This will cause scattering from a state $|\mathbf{k}\rangle$ (incident particle) to $|\mathbf{k}'\rangle$ (scattered particle) at a rate

---

[1] In a more general case $\mathbf{v} = \frac{1}{\hbar}\nabla_{\mathbf{k}}\mathcal{E}\left(\mathbf{k}\right)$, where $\mathcal{E}$ is the energy and $\nabla_{\mathbf{k}}$ is the gradient operator in $\mathbf{k}$–space: $\nabla_{\mathbf{k}}\mathcal{E} = \partial\mathcal{E}_x/\partial k_x + \partial\mathcal{E}_y/\partial k_y + \partial\mathcal{E}_z/\partial k_y$.

Fermi Golden Rule

$$\Gamma_{\mathbf{k}\to\mathbf{k}'} = \frac{2\pi}{\hbar}\left|\langle\mathbf{k}'|\,\widehat{V}_{\text{dir.}}\,|\mathbf{k}\rangle\right|^2 \delta\left(\mathcal{E}_{\mathbf{k}'} - \mathcal{E}_{\mathbf{k}}\right) \equiv W_{\mathbf{k}'\mathbf{k}}. \tag{2.5}$$

First, $\delta\left(\mathcal{E}_{\mathbf{k}'} - \mathcal{E}_{\mathbf{k}}\right)$ tells us that the energy is conserved and

$$\begin{aligned}
\langle\mathbf{k}'|\,\widehat{V}_{\text{dir.}}\,|\mathbf{k}\rangle &= \int \phi^*_{\mathbf{k}'}(\mathbf{r})V_{\text{dir.}}(\mathbf{r})\phi_{\mathbf{k}}(\mathbf{r})\,d^3\mathbf{r} \\
&= \left(\frac{1}{\sqrt{\text{Volume}}}\right)^2 \int e^{-i(\mathbf{k}'-\mathbf{k})\cdot\mathbf{r}}\,V_{\text{dir.}}(\mathbf{r})\,d^3\mathbf{r} \\
&\propto \sum_{\mathbf{R}} e^{-i(\mathbf{k}'-\mathbf{k})\cdot\mathbf{R}}\cdot\left[\int_{\text{unit cell}} e^{-i(\mathbf{k}'-\mathbf{k})\cdot\mathbf{r}}\,V_{\text{dir.}}(\mathbf{r})\,d^3\mathbf{r}\right],
\end{aligned}$$

where Volume refers to all space, $\phi_{\mathbf{k}}$ is the wave function and $\mathbf{R}$ is the Bravais lattice. Hence, this implies that for both classical and quantum scattering, the scattered amplitude involves the product of two terms

$$\text{Amplitude} \propto \sum_{\mathbf{G}} \delta\left(\mathbf{k}' - \mathbf{k} - \mathbf{G}\right)\cdot\left[\int_{\text{unit cell}} e^{-i(\mathbf{k}'-\mathbf{k})\cdot\mathbf{r}}\,V_{\text{dir.}}(\mathbf{r})\,d^3\mathbf{r}\right].$$

Thus, the scattered amplitude only depends on the lattice, since $\mathbf{G}$ is the reciprocal lattice, and the structure factor $S\left(\mathbf{k}' - \mathbf{k}\right)$. Therefore, we could think of $W_{\mathbf{k}'\mathbf{k}}$ as a scattering rate from other sources like phonons, for what follows that $W_{\mathbf{k}'\mathbf{k}}$ is general [28, 29].

Because $W_{\mathbf{k}'\mathbf{k}}$ is a general expression that helps us determine the scattering rate of phonons, we need to determine the change in the probability of occupying a position and wave–vector due to the collisions during certain time dt. On the one hand, the probability of scattering out of $\mathbf{k}$ in time dt can be defined as

$$\mathcal{P}_{\text{out}} = f\left(\mathbf{r},\mathbf{k},t\right)\sum_{\mathbf{k}'} W_{\mathbf{k}',\mathbf{k}}\,dt\left[1 - f\left(\mathbf{r},\mathbf{k}',t\right)\right],$$

where $f\left(\mathbf{r},\mathbf{k},t\right)$ is the probability that $\mathbf{k}$ is occupied and $1 - f\left(\mathbf{r},\mathbf{k}',t\right)$ is the probability that $\mathbf{k}'$ is unoccupied. On the other hand, the probability of scattering into $\mathbf{k}$ is, similarly

$$\mathcal{P}_{\text{in}} = \left[1 - f\left(\mathbf{r},\mathbf{k},t\right)\right]\sum_{\mathbf{k}'} W_{\mathbf{k},\mathbf{k}'}\,dt f\left(\mathbf{r},\mathbf{k}',t\right),$$

hence

$$\begin{aligned}
\left(\frac{\delta f}{\delta t}\right)_{\text{scatt.}} &= \frac{1}{dt}\left(\mathcal{P}_{\text{in}} - \mathcal{P}_{\text{out}}\right) \\
&= \sum_{\mathbf{k}'}\left[1 - f\left(\mathbf{r},\mathbf{k},t\right)\right]W_{\mathbf{k},\mathbf{k}'} f\left(\mathbf{r},\mathbf{k}',t\right) - f\left(\mathbf{r},\mathbf{k},t\right)W_{\mathbf{k}',\mathbf{k}}\left[1 - f\left(\mathbf{r},\mathbf{k}',t\right)\right] \\
&= \frac{V}{(2\pi)^3}\int d^3\mathbf{k}'\left\{\left[1 - f\left(\mathbf{r},\mathbf{k},t\right)\right]W_{\mathbf{k},\mathbf{k}'} f\left(\mathbf{r},\mathbf{k}',t\right) - f\left(\mathbf{r},\mathbf{k},t\right)W_{\mathbf{k}',\mathbf{k}}\left[1 - f\left(\mathbf{r},\mathbf{k}',t\right)\right]\right\}.
\end{aligned}$$

Here, V is the crystal volume [30]. This last collision integral represents the left–hand side of the Boltzmann transport equation [see eq. (2.4)] and is the important part for the carrier transport because it describes the response or contribution of the approximated short–range collisional forces that give the *friction* for the carrier transport. However, even if we know $W_{\mathbf{k}',\mathbf{k}}$, this has turned the Boltzmann equation into a complicated integro–differential equation for $f\left(\mathbf{r},\mathbf{k},t\right)$. Therefore, in order to solve this integro–differential equation numerically, it is necessary to use a computational method. In this work, we carried out the study numerically by using the Monte–Carlo method.

2.6 Numerical solution of the Boltzmann equation: ensemble Monte–Carlo approach

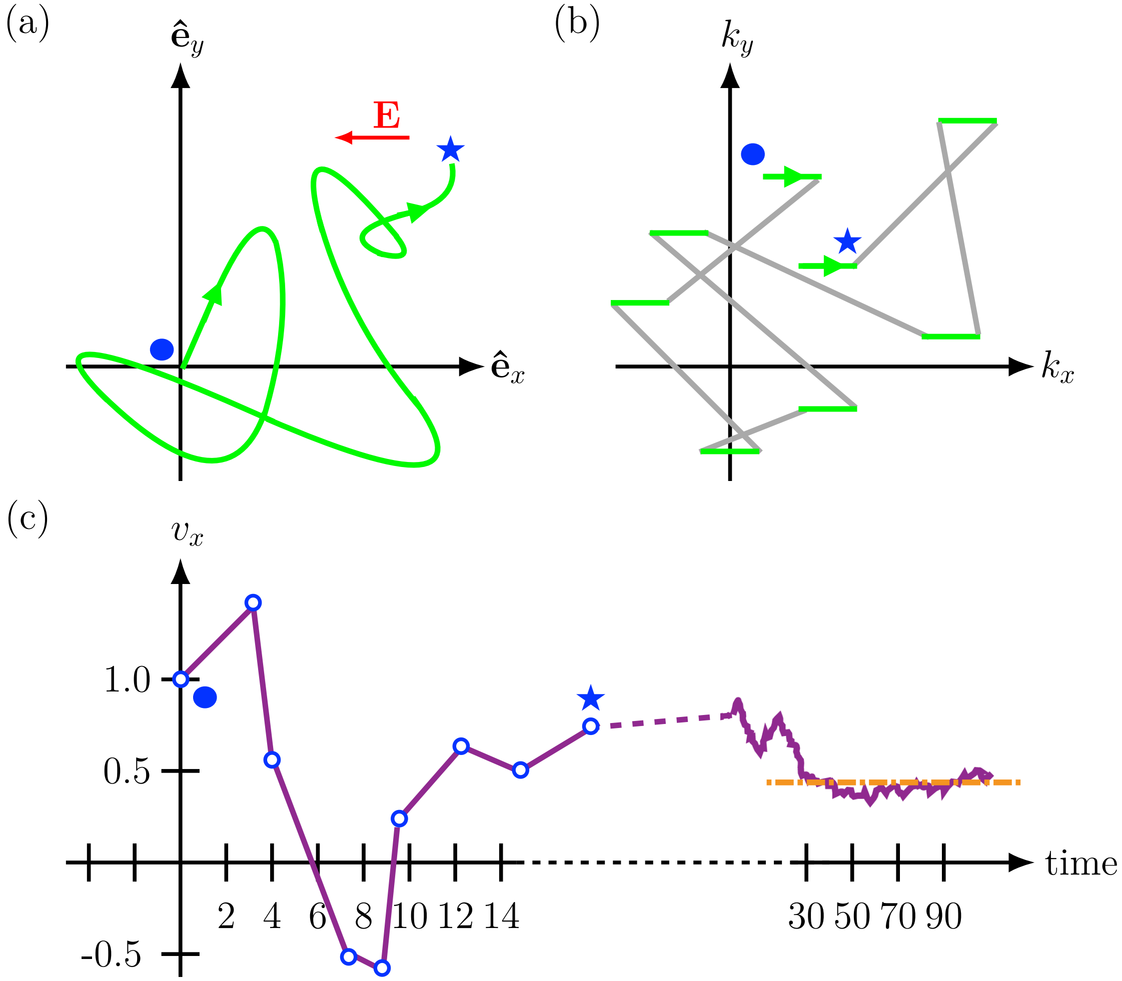

Figure 2.3: Sketch diagram of the Monte–Carlo method; for simplicity the method is depicted in two–dimensions. (a) Simulation of the sampling electron path under the influence of an external electric field E oriented in the x direction. (b) The same trajectory as in (a) but in momentum space. (c) Average carrier velocity over all steps starting from step 1 up to the running step number as a function of simulation time. The special icons in the three figures indicate the starting (•) and ending ($\star$) point of the path [36].

To model the transient carrier dynamics under the influence of an applied electric field and typical scattering mechanisms, we used a complete numerical approach: the ensemble Monte–Carlo model. For solving the Boltzmann transport equation, the Monte–Carlo method considers that the scattering process (acoustic, Coulomb and polar optical phonon scattering, intra– and inter–valley scattering, etc.) and the final states are stochastically selected [31, 32].

One of the advantages of the Monte–Carlo method is that we can extract derived physical information from simulated experiments, and it is a powerful technique for the discussion of stationary [31] or transient [33–35] transport effects in semiconductors. This numerical method has become a common technique to analyze and simulate the nonequilibrium carrier transport under heterogeneous conditions in semiconductor materials.

Figure 2.3 shows the basis of the Monte–Carlo method. Figure 2.3(a) shows the simulation of the sampling electron path under the influence of an external electric field **E** oriented in the x direction. The eight fragments of parabolas correspond to the eight free flights. The same trajectory of the electron but in momentum space is shown in figure 2.3(b). The heavy segments (green lines) are due to the effect of the field during free flights, while light lines (gray lines) represent the momentum changes in each scattering process [36]. The average carrier velocity at an n–th point over all previous $(n-1)$ paths is computed in figure 2.3(c). By considering a larger time–step as a function of simulation time, we can obtain an accurate drift velocity, as represented in figure 2.3(c) by the horizontal dot–dashed orange lines.

In the Monte–Carlo method, we assume that the semi–classical dynamics of particle motion consist of the generation of random free flight times by instantaneous and memoryless scattering events, which change the energy and momentum of the particle after each scattering event. In addition, the probability of an electron scattering in a short time interval dt is written as $\Gamma\left[\mathbf{k}\left(t\right)\right]dt$, where $\Gamma\left[\mathbf{k}\left(t\right)\right]$ is the scattering rate of an electron or hole of the wave vector **k** per unit time [31, 37]. For modeling the time-dependent electron dynamics, where the electric and magnetic fields are time independent, and acceleration is by external forces, the time evolution of **k** between collisions is given by

$$\mathbf{k}(t) = \mathbf{k}(0) - \frac{e\left(\mathbf{E} + \mathbf{v} \times \mathbf{B}\right)t}{\hbar},$$

where **E** and **B** are the electric and magnetic fields, respectively, and **v** is the velocity of the electron. Here, within each time interval of free flight, Bloch's theorem describes the momentum of each electron:

Bloch's theorem

$$\hbar\frac{d\mathbf{k}}{dt} = -e\mathbf{E}, \tag{2.6}$$

where the real space velocity is given by

$$v = \frac{1}{\hbar}\frac{d\mathcal{E}_{\mathbf{k}}}{dk}, \tag{2.7}$$

and $\mathcal{E}_{\mathbf{k}}$ is the energy. The probability of an electron that experiences a collision at time $t = 0$ and has not yet undergone another collision after a time t is [37]

$$\mathcal{P}_n(t) = e^{-\int_0^t \Gamma\left[\mathbf{k}\left(t'\right)\right]dt'},$$

hence when the electron suffers the next collision, the probability of scattering in time interval dt after a free flight of time t is given by

$$\mathcal{P}(t)dt = \Gamma\left[\mathbf{k}\left(t\right)\right]\mathcal{P}_n(t)dt = \Gamma\left[\mathbf{k}\left(t\right)\right]e^{-\int_0^t \Gamma\left[\mathbf{k}\left(t'\right)\right]dt'}dt. \tag{2.8}$$

The idea is to sample random flight times from this exponential probability density function with non–uniform distribution of free flight times, using typical random numbers uniformly distributed over the interval $[0,1]$. Integrating Eq. (2.8) and considering that τ_0^{-1} is the maximum value of $\Gamma\left[\mathbf{k}\left(t\right)\right]$ in the region of **k** space of interest, then for a constant $\Gamma\left[\mathbf{k}\left(t\right)\right] = \tau_0^{-1}$ value, the random flight times tested from $\mathcal{P}(t)$ are

$$\begin{aligned} r = \mathcal{P}(t_r) &= \int_0^{t=t_r} \mathcal{P}(t) dt \\ &= \int_0^{t=t_r} \Gamma\left[\mathbf{k}\left(t\right)\right] e^{-\int_0^t \Gamma\left[\mathbf{k}\left(t'\right)\right] dt'} dt \\ &= \frac{1}{\tau_0} \int_0^{t=t_r} e^{-\frac{1}{\tau_0}\int_0^t dt'} dt \\ &= \frac{1}{\tau_0} \int_0^{t=t_r} e^{-\frac{t}{\tau_0}} dt \\ &= 1 - e^{-\frac{t_r}{\tau_0}}, \end{aligned}$$

where $\tau_0 > 0$, r is a uniformly distributed random number, and t_r is the wanted free flight time, then

$$t_r = -\tau_0 \ln\left(1 - r\right).$$

However, because r is uniformly randomly distributed between 0 and 1, r and $1 - r$ are the same, hence

$$t_r = -\tau_0 \ln\left(r\right). \tag{2.9}$$

Until this point, we have an equation that describes the generation of random free flight time after each scattering event and results in a random walking process similar to the function of the underlying particle distribution. Finally, we need to specify the type of scattering mechanism (impurity, acoustic phonon, photon emission, etc.), including self–scattering, which determines the free flight and the final energy and momentum of the particle(s) after scattering. Self–scattering is a fictitious scattering process that does not affect the momentum or the energy of the particle and allow us to change the energy–dependent total scattering rate out of state $\mathbf{k}$ (for all scattering processes) into an energy–independent term by defining

$$\Gamma_{\text{self}}(\mathbf{k}) = \Gamma(\mathbf{k}) - \frac{1}{\tau(\mathbf{k})},$$

then, the total scattering rate is equal to self–scattering plus real scattering

$$\Gamma = \Gamma_{\text{self}}\left[n, \mathbf{k}\right] + \Gamma_1\left[n, \mathbf{k}\right] + \Gamma_2\left[n, \mathbf{k}\right] + \ldots + \Gamma_N\left[n, \mathbf{k}\right].$$

Here, n is the band index of the particle, and $\mathbf{k}$ is the wave–vector at the end of the free flight [37, 122].

To perform a transient simulation, a synchronous ensemble of particles is essential, in which the presented algorithm is repeated for each particle in the ensemble that represents the system of interest until the simulation is accomplished. The sketch model of the scattered free flight is illustrated in figure 2.4. In the free–flight duration time axis, N is the total number of particles in the simulation, while in the sampling time axis, t_s is the total simulation time, and Δt represents the time step at which the motion of all the particles is synchronized [32, 122]. Moreover, t_i is the free–flight duration time for the i–th particle, and each red cross illustrated in figure 2.4 represents random and instantaneous collisions or scattering events that may or may not happen during one time step.

Figure 2.4: Scattered free flight sketch where the motion of all N particles is synchronized at Δt. The red crosses ($\times$) denote each scattering event.

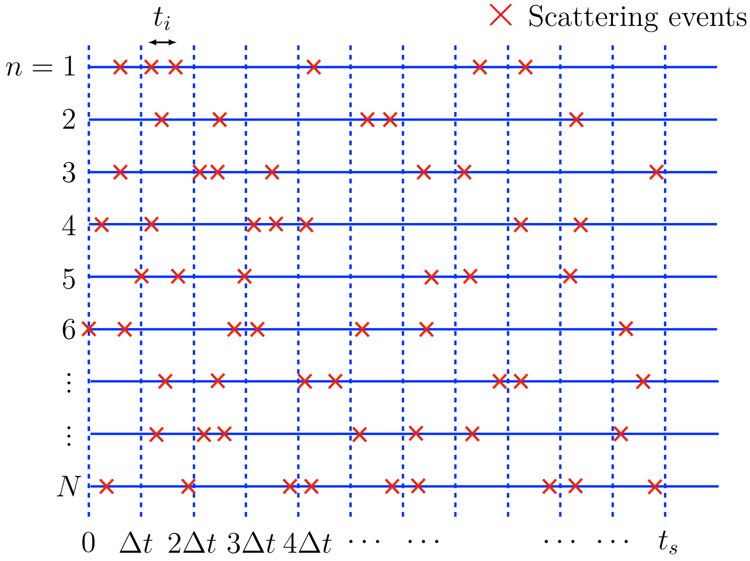
t_i
× Scattering events
$n = 1$
2
3
4
5
6
⋮
⋮
N
0
Δt
$2\Delta t$
$3\Delta t$
$4\Delta t$
$\cdots$
$\cdots$
$\cdots$
$\cdots$
t_s

In summary, in the ensemble Monte–Carlo approach, only until the end of the time step, each carrier is simulated and then the next particle in the ensemble is treated. The motion of each particle in the ensemble is simulated independently from other particles at each time step, and at the same time, the nonlinear effects and scattering mechanism are updated.

Finally, for the conduction band of $In_{0.57}Ga_{0.43}As$, we have considered a model with three non–parabolic spherical valleys: four equivalent L valleys and three equivalent X valleys. Also, the conduction bands are separated between each other, as shown in Fig. 2.5. The main physical constants used in the simulations are summarized in Table 2.1.

Figure 2.5: Energy band model for $In_{0.57}Ga_{0.43}As$, the L–valley and X–valley are at the families of directions $\langle 111 \rangle$ and $\langle 100 \rangle$, respectively.

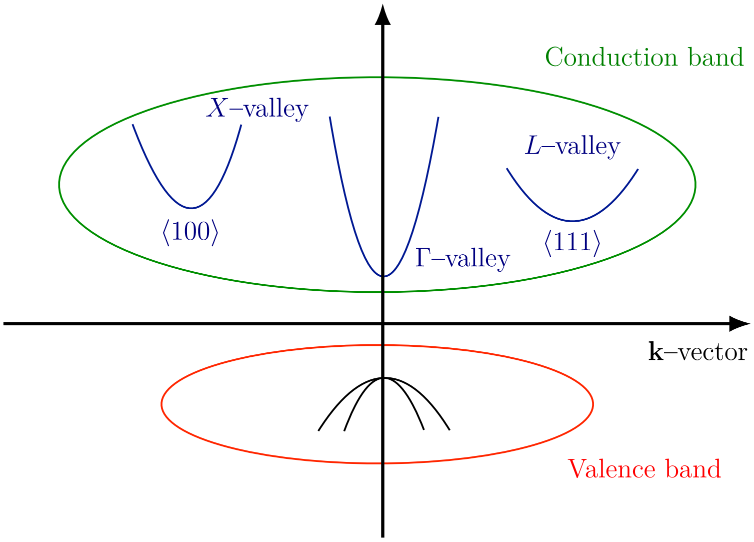
Conduction band
X–valley
$\langle 100 \rangle$
Γ–valley
L–valley
$\langle 111 \rangle$
k–vector
Valence band

Physical constant	Γ valley	L valley	X valley
Number of valleys	1	4	3
Effective mass ratio	0.041	0.26	0.54
Nonparabolicty factor $\left(\mathrm{eV}^{-1}\right)$	1.167	0.59	0.65
Longitudinal polar optic phonon energy (eV)	0.0345	0.0345	0.0345
Transverse polar optic phonon energy (eV)	0.0312	0.0312	0.0312
Acoustic phonon deformation potential (eV/cm)	9.2	9.2	9.2
Intervalley deformation potential (eV/cm)			
From Γ	0.0	7.0×10^8	7.0×10^8
From L	7.0×10^8	7.0×10^8	5.0×10^8
From X	7.0×10^8	5.0×10^8	5.8×10^8
Intervalley phonon energy (eV)			
From Γ	0.0	2.276×10^{-2}	2.384×10^{-2}
From L	2.384×10^{-2}	2.312×10^{-2}	2.696×10^{-2}
From X	2.276×10^{-2}	2.696×10^{-2}	2.276×10^{-2}
Low–frequency dielectric constant 13.88			
High–frequency dielectric constant 11.34			

Table 2.1: Table of physical constants of $In_{0.57}Ga_{0.43}As$ [17, 119].

Chapter 3

Study on the nonlinear THz optical effects in n–doped semiconductor $\text{In}_{0.57}\text{Ga}_{0.43}\text{As}$

This chapter is written based on:
Carlos Miguel Garcia–Rosas, Xin Chai, Xavier Ropagnol and Tsuneyuki Ozaki, "Time–frequency analysis of nonlinear terahertz signals due to hot electrons in the nonparabolic conduction bands of n–doped $\text{In}_{0.57}\text{Ga}_{0.43}\text{As}$ films", submitted for publication in Physics Review Letters.
With the Reuse and Permission License from American Physical Society.

To further deepen our understanding of nonlinear THz effects, we perform in the present work a systematic time–frequency study of the response of a classical n–doped semiconductor $\text{In}_{0.57}\text{Ga}_{0.43}\text{As}$ thin film when pumped by multi–cycle THz pulse with central frequencies from 0.2 to 1.5 THz, and incident peak electric fields ranging from 100 kV/cm up to 500 kV/cm. We show that high–order harmonic generation (HHG) is strongly dependent on the peak field strength but also on the central frequency of the incoming pulse. Indeed, we put in evidence that HHG is mainly generated by intervalley scattering. By applying the Gábor transform formalism [123–125], we also show that the emission due to HHG starts only when the photocurrent has a distorted biphasic truncated exponential form, which is evident for low THz frequency. On the other hand, HHG for higher THz frequencies is not as prominent because the truncation of the current generated by the THz pulse becomes comparable to the half–cycle of the THz pulse. In addition to HHG, we observe the generation of new spectral components above and below the fundamental frequency of the THz pulse. We call these new waves, which are in higher and lower frequencies than the central frequency of the main pulse, high–frequency components (HFC) and low–frequency components (LFC).

We use a time–frequency analysis based on the Gábor transform to study the transmitted electric field, putting in evidence for the first time that these HFC and LFC are generated only through intravalley scattering effects. It is important to note that similar LFC and HFC besides the fundamental frequency has been observed in recent reports on intense THz–matter interactions, such as those detected in the high–order harmonic spectra from graphene [19]. Given that nonparabolicity of the conduction band is the cause for these LFC and HFC, we expect them to be generated in many semiconductors (including graphene), potentially providing a new method to experimentally study their band structure.

Figure 3.1: Normal incidence and transmission of THz electric field through a thin conducting film deposited on a dielectric substrate: substrate / thin–film / air configuration.

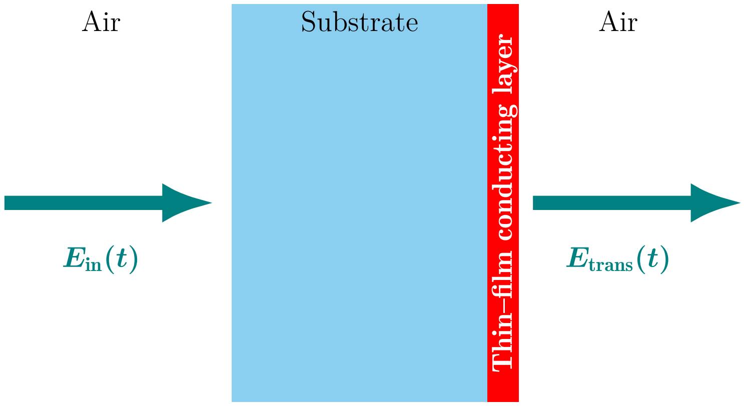

To understand the nonlinear carrier dynamics and the wave generation induced by the response of the InGaAs layer to multi–cycle THz pulses, we performed a theoretical analysis in the time domain by using the thin–film equation [9, 16, 18, 93], considering that the sample could be idealized as a thin conducting sheet with thickness d on an insulating substrate with refractive index N [16]. In our study, the sample is a 500–nm–thick n–type $\text{In}_{0.57}\text{Ga}_{0.43}\text{As}$ (100) epilayer with a doping concentration of 2×10^{18} cm^{-3} [18]. If the THz pulse irradiates the sample from the InP substrate side (substrate / thin–film / air configuration, see Fig. 3.1) [126], the thin–film equation is given by the expression

Thin–film equation

$$E_{\text{trans.}}(t) = \frac{1}{Y_0 + Y_S}\left[\frac{4Y_S}{N+1}E_{\text{in.}}(t) - J(t)\,d\right]. \tag{3.1}$$

Here, $E_{\text{trans.}}(t)$ and $E_{\text{in.}}(t)$ are the transmitted and incident THz field, respectively, $Y_0 = (377\,\Omega)^{-1}$ is the free–space admittance, and $Y_S = NY_0$ is the admittance of the substrate, in which $N = 3.1$ is the refractive index of InP at THz frequencies [9]. We implement an analytical–band ensemble Monte–Carlo approach to solve the Boltzmann transport equation [see Eq. (2.4)] [31, 119, 122, 127] for modeling the transient carrier dynamics of the sample. To detail the different scattering effects in our simulations, we consider the typical scattering mechanism in a compound semiconductor such as acoustic, Coulomb and polar optical phonon scattering, as well as intra– and inter–valley scattering [31, 32]. Through these simulations, we obtain the carrier dynamics in the Γ, L and X valleys of the conduction band and the current density $J(t)$ is directly determined by the average drift velocity [41, 93, 128, 129], where

$$\begin{aligned} J &= n\,(n_\Gamma v_\Gamma + n_L v_L + n_X v_X)\,e \\ &= n\,\langle v_\Gamma\rangle\,e + n\,\langle v_L\rangle\,e + n\,\langle v_X\rangle\,e. \end{aligned}$$

Here, e is the electron charge, n is the doping concentration, and $\langle v_i\rangle = n_i v_i$ ($i = \Gamma, L, X$) is the average drift velocity of each valley, where n_i and v_i are the individual valley occupation and drift velocity, respectively, which were also calculated from the bulk Monte–Carlo code. Figure 3.2 shows the flow diagram that summarizes the bulk ensemble Monte–Carlo algorithm [32] described in Section 2.6, where the thin–film equation is included in order to obtain the final transmitted electric THz field.

To model the carrier dynamics in the nonparabolic conduction bands, we need to analyze how the mass of the carriers changes as a function of the energy. One approach to defining the non-

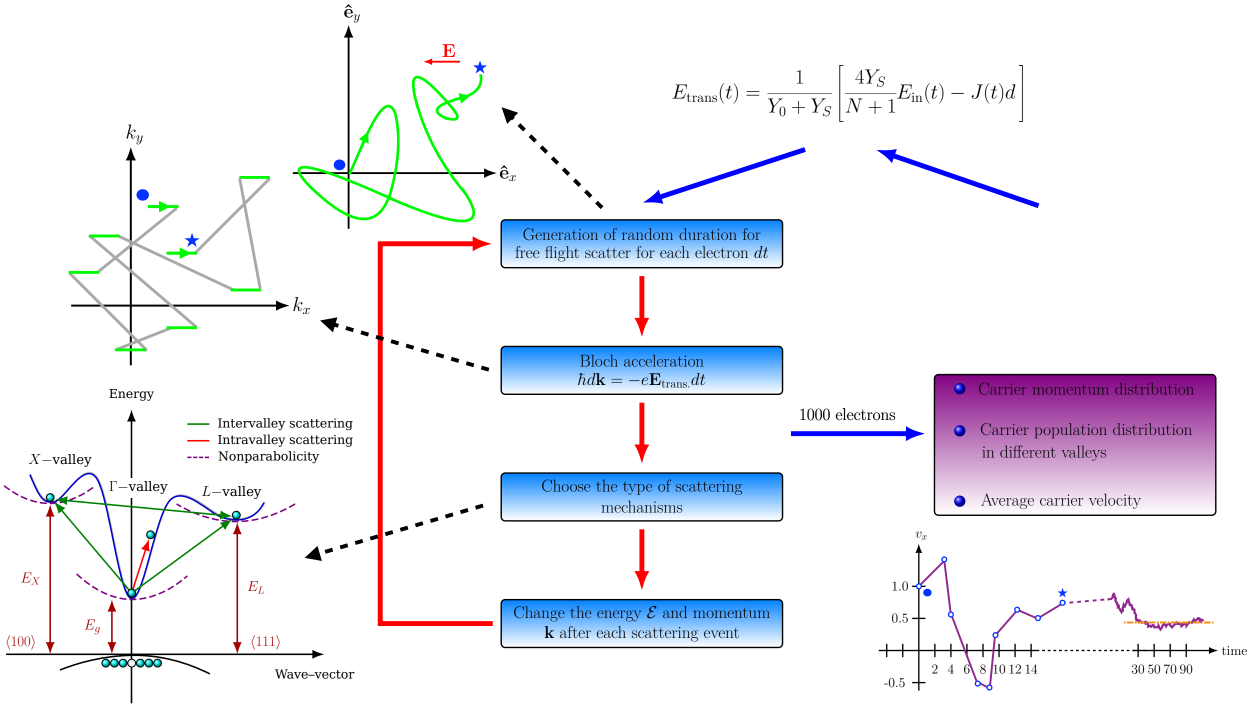
$\hat{e}_y$
E
$\hat{e}_x$
$E_{\mathrm{trans}}(t) = \frac{1}{Y_0 + Y_S}\left[\frac{4Y_S}{N+1}E_{\mathrm{in}}(t) - J(t)d\right]$
k_y
k_x
Generation of random duration for free flight scatter for each electron dt
Bloch acceleration $\hbar d\mathbf{k} = -e\mathbf{E}_{\mathrm{trans.}}dt$
Choose the type of scattering mechanisms
Change the energy $\mathcal{E}$ and momentum $\mathbf{k}$ after each scattering event
1000 electrons
Carrier momentum distribution
Carrier population distribution in different valleys
Average carrier velocity
Energy
Intervalley scattering
Intravalley scattering
Nonparabolicity
$X-$valley
$\Gamma-$valley
$L-$valley
E_X
E_L
E_g
⟨100⟩
⟨111⟩
Wave–vector
v_x
1.0
0.5
-0.5
2 4 6 8 10 12 14
30 50 70 90
time

Figure 3.2: Schematic Monte–Carlo algorithm flow diagram. Initially, we input in the Monte–Carlo code the thin–film transmission equation, and by Bloch's theorem and an iterative process, we are able to find the average drift velocity of each valley and compute the current density. Then, we obtain the transmitted electric field by subtracting the incident electric field the calculated from the current density.

parabolic band dispersions is by considering the second–order k^2 ellipsoidal energy surfaces. Here, we approximate the electron kinetic energy of the nonparabolic conduction band of the InGaAs semiconductor by using the simplified one–dimensional Kane's approximation [130–133], thus

$$\frac{\hbar^2 k^2}{2m_1} = \gamma(\mathcal{E}) = \mathcal{E} + \alpha_i \mathcal{E}^2. \tag{3.2}$$

Here, k is the magnitude of the wave vector, α_i and $m_1 = m_i m_0$ ($i = \Gamma$, X and L) are the nonparabolicity factor and the density of state (DOS) effective mass of electrons in each valley, respectively [134]. By differentiating Eq. (3.2) with respect to k, we obtain the effective carrier mass of each valley [131–133]

$$m_i^* = \hbar^2 k \left(\frac{d\mathcal{E}_i}{dk}\right)^{-1} = m_1\left(1 + 2\alpha_i \mathcal{E}_i\right). \tag{3.3}$$

Hence, the effective carrier mass linearly depends on the energy and α_i and m_i are already known physical constants [119, 132].

In the following sections, we first performed simulations on the nonlinear THz effects induced by intense multi–cycle THz radiation in an n–doped $In_{0.57}Ga_{0.43}As$. In the simulations, we consider a temperature of 300 K and use the physical constants of $In_{0.57}Ga_{0.43}As$ sample reported by Long *et al.* and Razzari *et al.* [17, 119].

3.1 THz pulses with relatively low and high frequency

Figure 3.3 shows the incident and transmitted THz waveform for THz pulses with central frequencies of 0.2 THz, 0.4 THz, 1.0 THz and 1.5 THz. The incident peak electric fields used here are 350 kV/cm for 0.2 THz and 0.4 THz pulses, 114 kV/cm for 1.0 THz pulse and 125 kV/cm for 1.5 THz pulse. We have to clarify that even though we calculate incident peak electric fields ranging from 100 kV/cm up to 500 kV/cm, the given specific peak electric fields show and represent clearly the following phenomenon. For THz pulses with 0.2 and 0.4 THz, we found that the distorted current density shows a sharp truncation [see Figs. 3.3(a) and 3.3(b)]. On the other hand, for the THz pulses with 1.0 and 1.5 THz, it is challenging to observe clear current truncations faster than the duration of the half–cycle of the original incident THz waveform [see Figs. 3.3(c) and 3.3(d)].

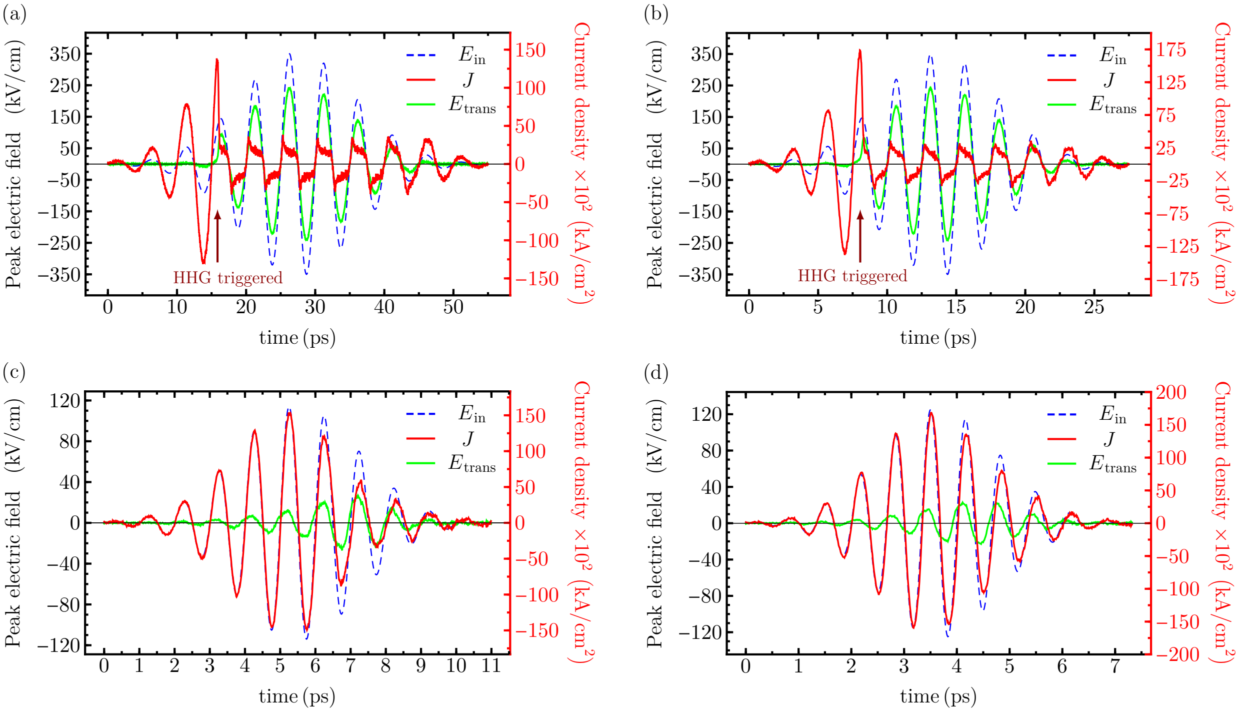

Figure 3.3: Current density (solid red line) and transmitted THz waveform (solid green line) generated by a multi–cycle THz pulse (blue dashed line) centered at (a) 0.2 THz, (b) 0.4 THz, (c) 1.0 THz and (d) 1.5 THz. The incident peak fields used here are 350 kV/cm for (a) 0.2 THz and (b) 0.4 THz pulses, (c) 114 kV/cm for 1.0 THz pulse and (d) 125 kV/cm for 1.5 THz pulse.

For relatively low–frequency multi–cycle pulses and high incident peak fields, the direct consequence of the distorted current phases with the driving THz fields is the clear high–harmonic (HH) peaks in the transmitted intensity spectra (up to the 11th and 7th harmonic for 0.2 THz and 0.4 THz pulses, respectively) [see Figs. 3.4(a) and 3.4(b)]. This is the result of the drastic change in the carrier effective mass in the amplitude of the electric field of the half–cycle of the original incident THz waveform. On the other hand, for relatively high frequency and low incident peak fields, the changes in the frequency are less clear due to the absence of clear current truncations. However, we can still barely observe high–order harmonic generation (HHG) in the intensity spectra (up to the 5th order when pumping by the 1.0 THz pulses and up to the 3rd order when pumped by the 1.5 THz pulses) [see Figs. 3.4(c) and 3.4(d)]. In addition, we can also observe some small peaks that are located at 0.3 THz and 1.7 THz when the sample is pumped by the 1.0 THz pulses. These new frequencies, which do not correspond to any harmonic order, are named LFC and HFC [see Fig. 3.8(c)].

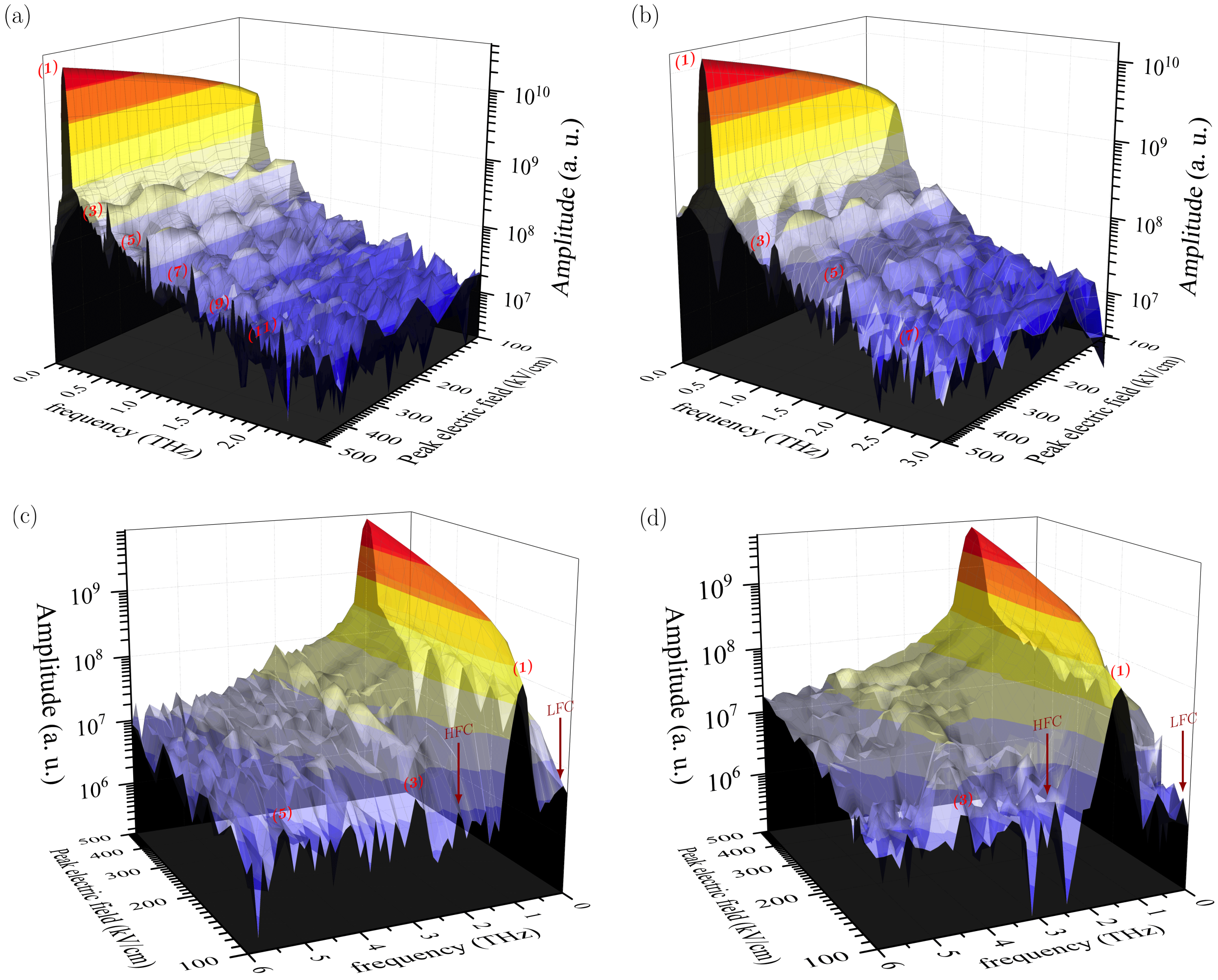

Figure 3.4: Simulations of HHG, LFC and HFC. Simulations of higher–order harmonic generation in $In_{0.57}Ga_{0.43}As$ sample, using the analytical–band ensemble Monte–Carlo approach to solve the Boltzmann transport equation: amplitude spectra of the transmitted THz waveforms through the $In_{0.57}Ga_{0.43}As$ sample as a function of the THz peak electric fields, for fundamental frequencies of (a) 0.2 THz, (b) 0.4 THz, (c) 1.0 THz and (d) 1.5 THz.

For an ideal square wave, the harmonic order of the Fourier decomposition would extend to infinity. In our case, the intensity and order of the HHG depend on the modulation of the photocurrent. The stronger and faster are the truncations of the photocurrent, the higher are the HH order. As a result, the HHG is easier to see using a relatively low–frequency source, resulting in a better temporal truncation contrast in the current density due to the drastic change of the carrier population of the satellite valleys [see Fig. 3.4(a)]. Moreover, for relatively high–frequency THz pulses at similar field strengths, it is difficult to have sharper truncations, and therefore the harmonics [such as the 5th harmonic of the 1.0 THz pulse in figure 3.4(c)] are less evident. However, under these conditions, we observe new frequencies located just above and below the fundamental frequency of the main pulse. These HFC and LFC are evident when we pump the InGaAs thin film with relatively high–frequency multi–cycle THz pulses. Surprisingly, the HHG intensity decrease by increasing the intensity of the pump pulse and the LFC and HFC vanished [see Figs. 3.4(c), 3.4(d) and 3.10]. Here, the carrier population of the X and L valleys rapidly increases but the temporal resolution where the intra– and inter–valley scattering can happen is lower compared with the low–frequency THz pulses. Therefore, even though the intensity of the pump pulse is increased, the intra– and inter–valley scattering effects will be reduced and nonlinear effects will start to get complex.

3.2 Gábor transform formalism

To measure an input time signal with accuracy in both the time and frequency domains, we performed a time–frequency analysis, which allows us to capture the entire time–frequency content of the transmitted multi–cycle THz waveforms and at the same time generate a spectrogram [123, 124]. For this, we applied the Gábor transform formalism to the transmitted multi–cycle THz waveforms to explain and understand the HHG, LFC and HFC exhibited at different frequencies of the spectra [125].

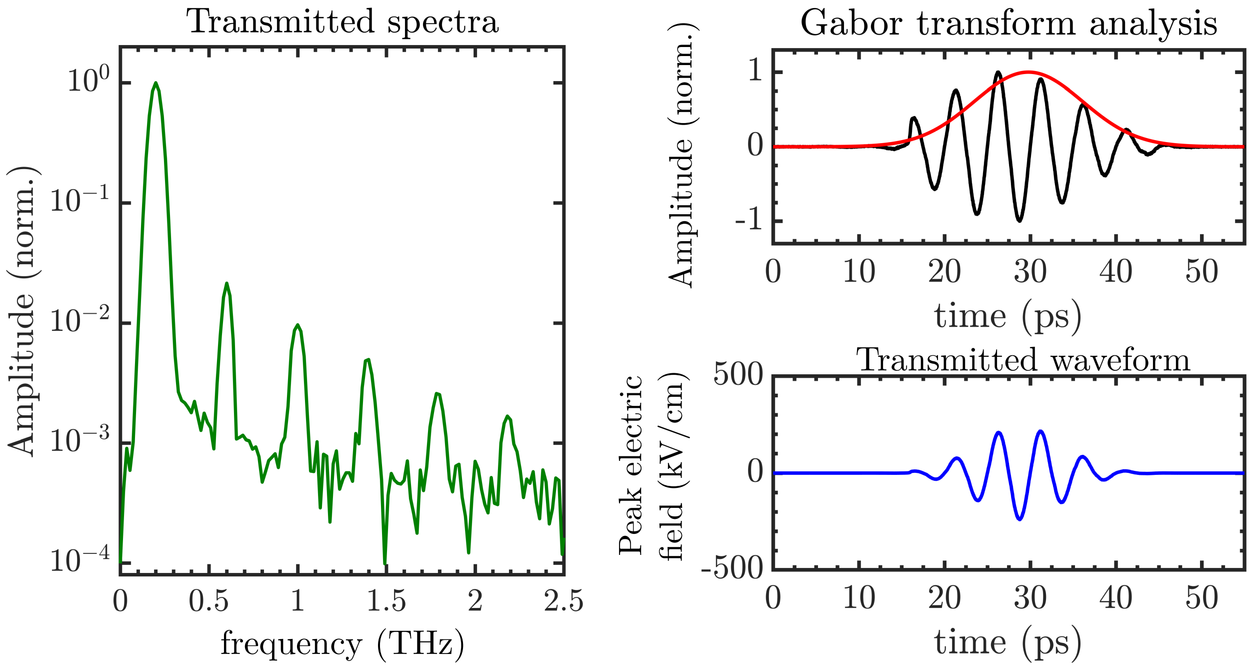

Figure 3.5: Example of the Gábor transform filter analysis. Top right figure: Input time signal $f(t)$ (black line) and the Gábor time filter $g_x(t)$ (red line) for a Gaussian filter. Bottom right figure: product of the $f(t)$ and $g_x(t)$ functions. Left figure: corresponding Fourier transform spectra.

Let $F(\omega)$ be the Fourier transform, where

$$F(\omega) = \frac{1}{\sqrt{2\pi}} \int_{-\infty}^{\infty} f(t) e^{-i\omega t} dt. \tag{3.4}$$

We can denote a Gaussian filter function as g_x. To construct the Gábor transform, we need to multiply the Gaussian filter function with the original time signal $f(t)$, so we can select a special windowed section of the signal. To obtain the local frequency information in time, we need to apply a Fourier transform to the windowed section. Thus, the Gábor transform of a signal $f(t)$ is defined as

Gábor transform

$$G_x(\tau,\omega) = \frac{1}{\sqrt{2\pi}}\int_{-\infty}^{\infty} f(t) g_x e^{-i\omega t} dt = \frac{1}{\sqrt{2\pi}}\int_{-\infty}^{\infty} f(t) e^{-a(t-\tau)^2} e^{-i\omega t} dt, \tag{3.5}$$

where the real parameter τ is used to translate the *time–frequency window* [123, 124] and a is the temporal window size or time filter parameter, which controls the width of the Gaussian function.

Figure 3.5 shows the Gábor transform formalism applied to an input signal and the windowed Fourier transform that draws out the local frequencies of a local time window. The key for generating a good spectrogram, is to use different filter widths (broader or narrower window). We can then determine an upright resolution time–frequency spectrogram, but we need to consider that a better resolution in the frequency domain we obtain, reduces the accuracy resolution in the time domain (and vice–versa), due to the Heisenberg uncertainty principle [123]. Thus, we have to be careful in selecting the time filter parameter to avoid over estimations of physical and mathematical results.

3.3 Time–frequency analysis for low–frequency THz pulses

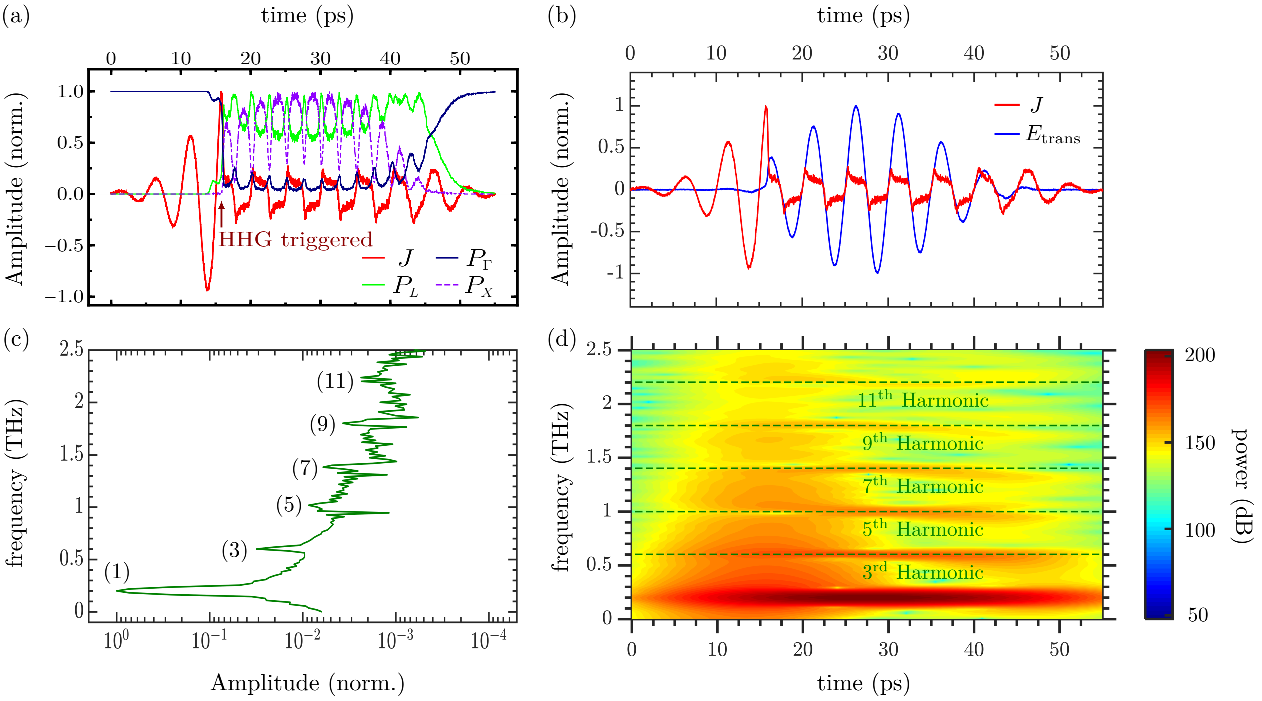

Figure 3.6: Time–frequency analysis, or Gábor transform, with a temporal window size equal to $a = 0.01$, for the incident peak fields at 350 kV/cm for 0.2 THz pulse. (a) Normalized temporal current density (solid red line), and carrier populations in the Γ (dark blue solid line), L (solid lime line) and X (broken violet line) valleys. (b) Current density (solid red line) and transmitted multi–cycle THz pulse (solid blue line). (c) The corresponding transmitted amplitude spectra. (d) HHs (broken green lines) are shown during the time of the pulse.

First, to better understand the HHG from relatively low–frequency multi–cycle THz pulses (0.2 THz) and high incident peak field (350 kV/cm), we analyze the carrier populations in the Γ, L and X valleys. Figure 3.6(a) shows a drastic reduction in the carrier population of the Γ valley around 16 ps. At that moment, because of the high incident field, the ponderomotive acceleration is strong enough that the carriers gain sufficient kinetic energy to efficiently undergo intervalley scattering from the Γ to the L and X valleys [18]. The HHG is mainly caused by the intervalley transitions of the carriers from the Γ valley to L and X valleys, and also from L valleys to X valleys and vice versa. This intervalley scattering process between the Γ valley and the satellite valleys is repeated or continued throughout the THz pulse.

Furthermore, the time–frequency analysis shows that the third harmonic is emitted around the highest intensity and the fifth and higher harmonics only appear at a certain time of the THz pulse and with weaker intensity [see Fig. 3.6(d)] because as we strongly reduce the number of contributing recombination times, merely the high frequencies near the central cutoff frequency $\omega_{\text{cut}}^{\text{HHG}}$ become enhanced [135].

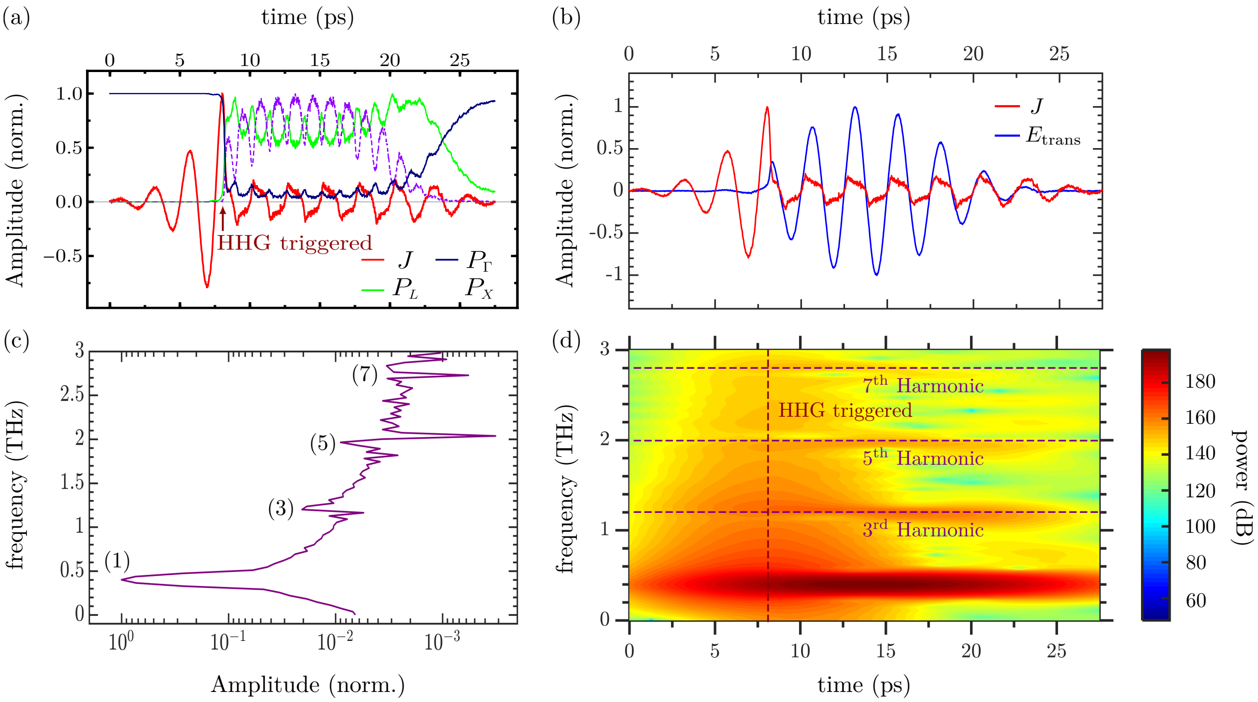

Figure 3.7: Time–frequency analysis, or Gábor transform, with a temporal window size equal to $a = 0.035$, for the incident peak fields at 350 kV/cm for 0.4 THz pulse. (a) Normalized temporal current density (solid red line), and carrier populations in the Γ (dark blue solid line), L (solid lime line) and X (broken violet line) valleys. (b) Current density (solid red line) and transmitted multi–cycle THz pulse (solid blue line). (c) The corresponding transmitted amplitude spectra. (d) HHs (broken purple lines) are shown during the time of the pulse.

At relatively high THz fields (350 kV/cm), the 0.4 THz pulse shows a distorted current density with truncations in the multi–cycle pulse [see Fig. 3.7(a)], so at this point, the intervalley scattering effects between the Γ, L and X valleys occur due to strong ponderomotive acceleration [18]. Again, the intervalley transitions of the carriers from the valley to L and X valleys, and from the L valleys to X valleys or vice versa, generate the triggered HHG. Additionally, in the time–frequency analysis, the third harmonic emission exists in a significant part of the duration of the 0.4 THz pulse and is exhibited close to the highest intensity [see Fig. 3.7(d)]. Also, the fifth harmonic is generated with weak intensity, ranging from ~ 2.5 ps up to ~ 24 ps.

3.4 Time–frequency analysis for high–frequency THz pulses

In this section, we compute the carrier population for the 1.0 THz pulse with an incident peak field at 114 kV/cm. Up until the peak of the fourth cycle of the current density [see the blue arrow of Fig. 3.8(a)], the carriers remain in the Γ valley, but after a few picoseconds, electrons gain enough energy to be scattered from the Γ valley to the higher satellite valleys. However, we can clearly see that the maximum intensity of the third harmonic is occurring at the same time as the maximum intensity of the THz pulse, precisely when the carrier populations of the L and X valleys achieve a maximum [see the red arrow of Fig. 3.8(a)]. If we look at the LFC (0.3 THz) and HFC (1.7 THz), considerably strong emission compared to the HH peaks is observed few picoseconds after the peak of the sixth cycle of the current density [see Fig. 3.8(d)].

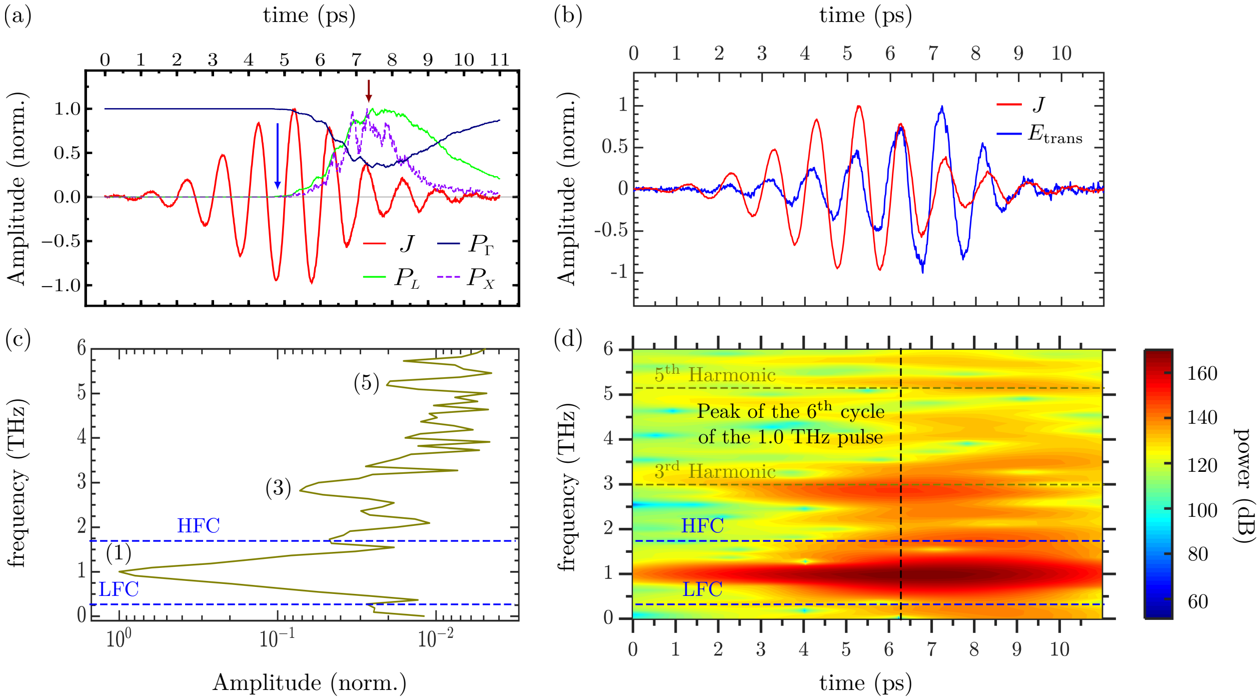

Figure 3.8: Time–frequency analysis, or Gábor transform, with a temporal window size equal to $a = 0.18$, for the incident peak fields at 114 kV/cm for 1.0 THz pulse. (a) Normalized temporal current density (solid red line), and carrier populations in the Γ (dark blue solid line), L (solid lime line) and X (broken violet line) valleys. (b) Current density (solid red line) and transmitted multi–cycle THz pulse (solid blue line). (c) The corresponding transmitted amplitude spectra. (d) HH (broken green olive lines) is emitted throughout the THz pulse, and for the LFC and HFC, the emission is observed after the time when the peak of the fourth cycle in the 1.0 THz pulse arrives, while their emission is much lower for earlier times.

Figure 3.9(a) shows an enhancement of carriers in the L and X valleys starting just after the fifth peak of the current density of the 1.5 THz pulse arrives. At this time, the carriers in the valley are highly energetic, and the LFC and HFC are generated in the transmitted amplitude spectra due to the intravalley scattering of the carriers. This effect is purely due to the intravalley scattering, reflecting the nonparabolicity of the conduction band. The generation of LHC and HFC occurs when the carrier population of the L and X valleys increases, but in this case, the emission of the LFC and HFC are not as strong as in the 1.0 THz pulse [see Fig. 3.9(d)].

We perform additional calculations for the case of relatively high THz frequency (1.0 THz) and low incident peak field. For a peak electric field of 100 kV/cm, (i) the change in the carrier population in the Γ valley is small [see Fig. 3.10(a)], (ii) low–frequency components appear in the transmitted amplitude spectra [see Fig. 3.10(b)], and (iii) high–order harmonics become apparent but with very low intensity [see Fig. 3.10(d)]. When we increase the peak electric field, the high–frequency components become evident when the peak electric fields are 110–125 kV/cm [see Figs. 3.10(e) and 3.10(f)].

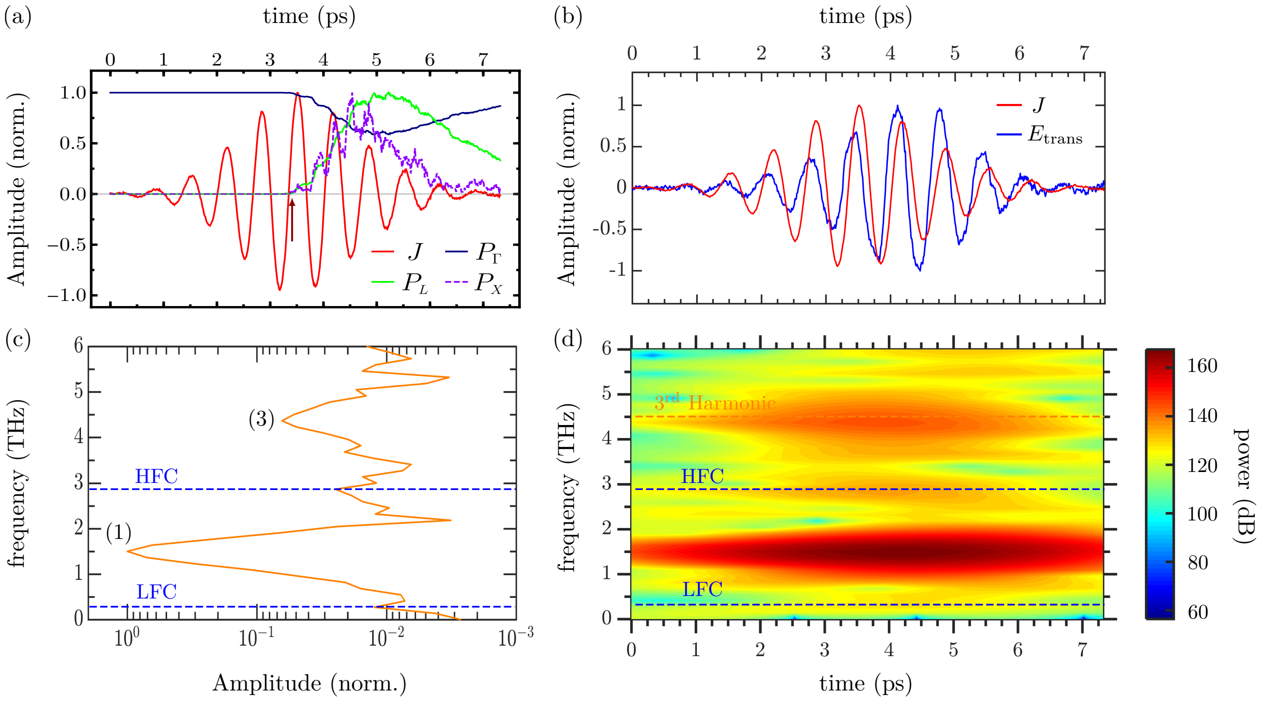

Figure 3.9: Time–frequency analysis, or Gábor transform, with a temporal window size equal to $a = 0.24$, for the incident peak fields at 125 kV/cm for 1.5 THz pulse. (a) Normalized temporal current density (solid red line), and carrier populations in the Γ (dark blue solid line), *L* (solid lime line) and *X* (broken violet line). (b) Current density (solid red line) and transmitted multi–cycle THz pulse (solid blue line). (c) The corresponding transmitted amplitude spectra. (d) HH (broken orange lines) is emitted throughout the THz pulse, and for the LFC and HFC (broken blue lines), the emission is observed when the peak of the fifth cycle in the 1.5 THz pulse arrives (see red arrow).

To analyze the generation of the low– and high–frequency components for relatively high frequencies and low incident peak fields, we compute the transmitted amplitude spectra for the incident peak fields ranging from 110 kV/cm up to 140 kV/cm for 1.0 THz and 1.5 THz pulses. Figure 3.10(e)–(h) shows the evolution of the LFC and HFC at different peak fields, exhibiting clearly the LFC and HFC from ~110 kV/cm up to ~125 kV/cm for 1.0 THz pulses [see Figs. 3.10(e) and 3.10(f)] and from ~115 kV/cm up to ~135 kV/cm for 1.5 THz pulses [see Figs. 3.10(g) and 3.10(h)]. For the case of 1.0 THz pulses, as we increase the electric field strength, the nonlinear effect starts to become complex over 140 kV/cm because the carrier population of the *X* and *L* valley begins to increase rapidly within the duration of the THz pulse, and the scattering time is suddenly reduced. Hence, for the higher incident peak field, the HHG has a weak intensity, and the LFC and HFC vanish. These results show a strong correlation between the carrier population in the Γ valley and the nonlinear THz emission in both low– and high–frequency components. This confirms that for nonlinear THz effects to occur, we need a sufficient population of carriers in the Γ valley. Also, the emission of the LFC and HFC do not span the whole duration of the THz pulse for 110–125 kV/cm peak fields [see Figs. 3.10(e) and 3.10(f)] because having both effects at the same time may decrease the efficiency of both intra– and inter–valley scattering processes.

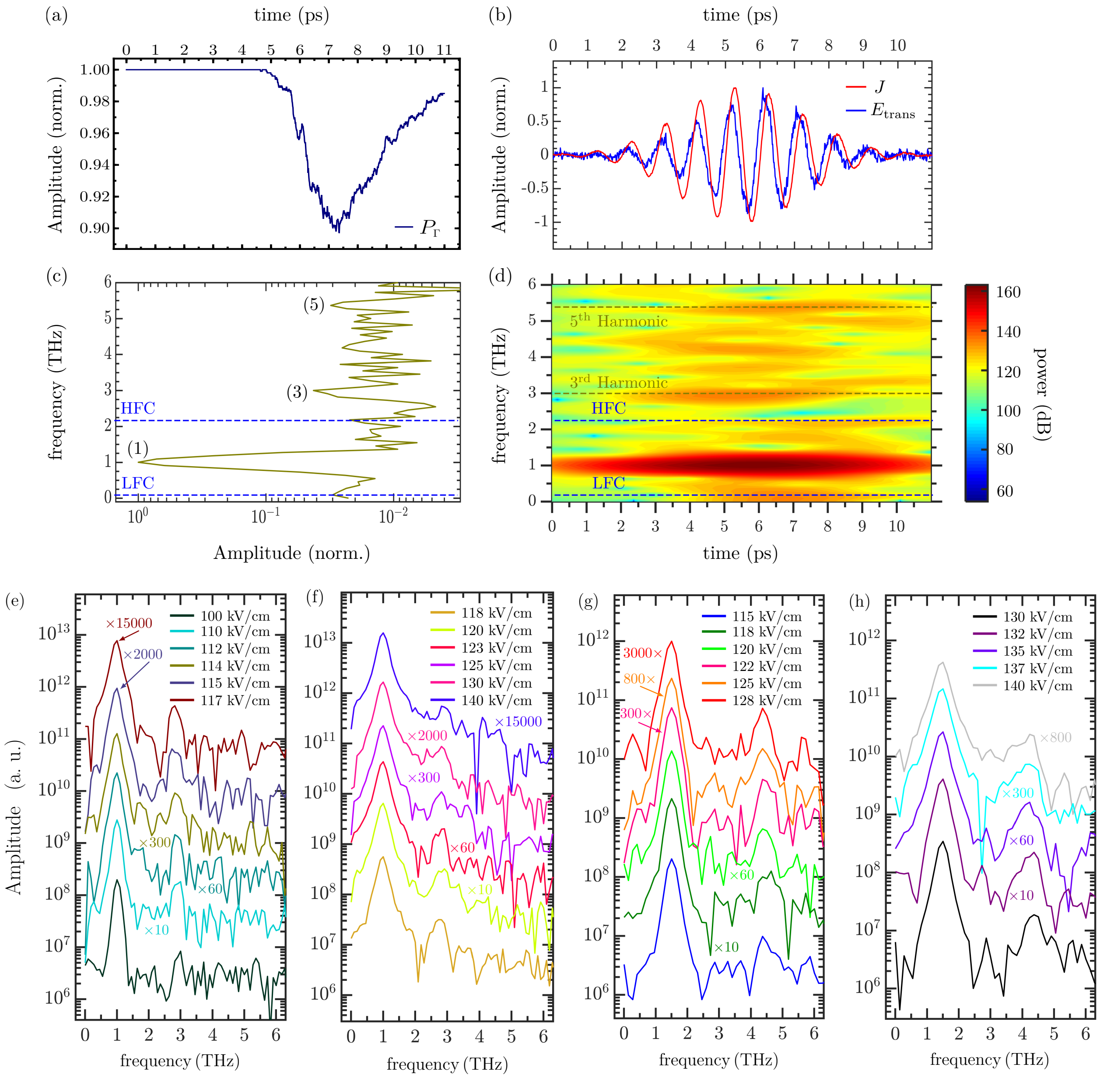

Figure 3.10: Time–frequency analysis, or Gábor transform, with a temporal window size equal to $a = 0.18$, for the incident peak fields at 100 kV/cm for 1.0 THz pulse. (a) Carrier population in the Γ (dark blue solid line) valley. (b) Current density (solid red line) and transmitted multi–cycle THz pulse (solid blue line). (c) The corresponding transmitted amplitude spectra. (d) HHs (broken green olive lines) and LFC and HFC (broken blue lines) are emitted throughout the THz pulse. LFC and HFC generation analysis for multi–cycle THz pulses. Transmitted amplitude spectra for incident peak fields ranging from 110 kV/cm up to 140 kV/cm for 1.0 THz pulse [figures (e) and (f)] and 115 kV/cm up to 140 kV/cm for 1.5 THz pulse [figures (g) and (h)]. Some of the spectra were multiplied by a factor for better visualization.

3.5 Average effective carrier mass

Next, we study the origin of the LFC and HFC. For this, first, we calculate with the Monte–Carlo code the average energy of the carriers $\langle E_i \rangle$ (for each $i = \Gamma$, L, X valleys) as a function of time and using Eq. (3.3), and we can obtain the average carrier effective mass $\langle m_i^* \rangle$ (for each $i = \Gamma$, L, X valleys) as well as a function of time. Figure 3.11 shows $\langle m_i^* \rangle$ and $\langle E_i \rangle$ as a function of time for (a) 0.2 THz pulses at an incident peak field of 350 kV/cm and (b) 1.0 THz pulses at 114 kV/cm. Since $\langle m_X^* \rangle$ is larger than $\langle m_\Gamma^* \rangle$ and $\langle m_L^* \rangle$, it takes more time for carriers in the X valley to be scattered [136, 137]. On the other hand, carriers in the Γ valley have more mobility and thus are more frequently scattered to the satellite valleys [see Fig. 3.11(b)].

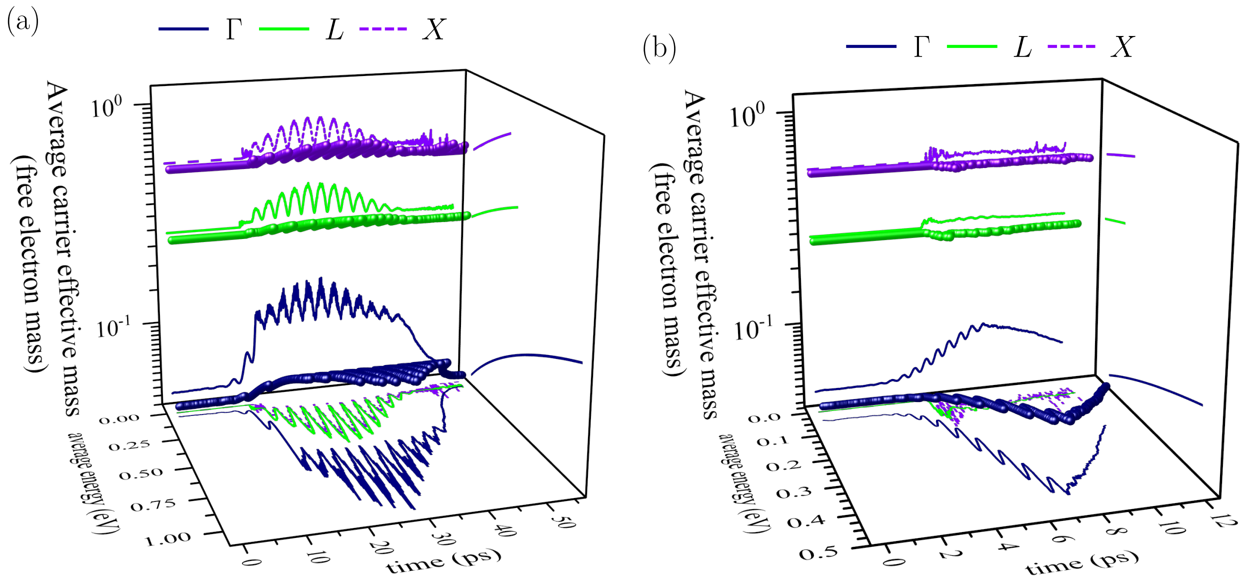

Figure 3.11: (a) and (b) Calculated average electron effective mass of each Γ (dark blue solid line), L (solid lime line) and X (broken violet line) valley as a function of the average energy and time of the THz pulse, where the incident peak field is centered at (a) 350 kV/cm for 0.2 THz and (b) 114 kV/cm for 1.0 THz.

Then, we apply a fast Fourier Transform (FFT) to the calculated $\langle m_i^* \rangle$ to observe the oscillation that the $\langle m_i^* \rangle$ has when it is irradiated by a THz field and associate the frequency components that result in the amplitude spectra of $\langle m_i^* \rangle$ with the odd harmonics of the 0.2 THz and 1.0 THz pulses. When the electric field of the THz pulse is weak, $\langle m_i^* \rangle$ is constant, and thus nonlinear THz effects are not observed in the current density and transmitted THz pulse. In this case, the amplitude spectrum of $\langle m_i^* \rangle$ will be a narrow function centered at 0 THz and the current density oscillates as the driving THz frequency. However, when the THz field is increased [see Fig. 3.11], we find several peaks appearing in the amplitude spectra of $\langle m_i^* \rangle$ [see Fig. 3.12] and as a consequence, a distorted biphasic truncated exponential current density [see Fig. 3.3(a)]. The most evident peaks that appear in the amplitude spectra of $\langle m_i^* \rangle$ are those that result in the harmonic generation of the incident THz pulse. For example, in figure 3.12(b), the peak centered at 2 THz in the amplitude spectra of $\langle m_i^* \rangle$ results in the third harmonic of the 1.0 THz pulse because $\langle m_i^* \rangle$ has a $2\,\omega_{\mathrm{THz}}$ component, hence the current density is modulated by $2\,\omega_{\mathrm{THz}}$ and it will have a $3\,\omega_{\mathrm{THz}}$ component (this is $\omega_{\mathrm{THz}} + 2\,\omega_{\mathrm{THz}}$). This modulation in $\langle m_i^* \rangle$ results in modulations in $J(t)$, thus generating the harmonics via intervalley scattering. Moreover, under the same criteria, the peaks at ~0.4 THz, ~0.8 THz, ~1.2 THz, ~1.6 THz, and ~2.0 THz of figure 3.12(a), result in the odd harmonics of the 0.2 THz pulse, because $\langle m_i^* \rangle$ has $0.4\,\omega_{\mathrm{THz}}$, $0.8\,\omega_{\mathrm{THz}}$, $1.2\,\omega_{\mathrm{THz}}$, $1.6\,\omega_{\mathrm{THz}}$, and $2.0\,\omega_{\mathrm{THz}}$ components, thus the current density will have $0.6\,\omega_{\mathrm{THz}}$, $1.0\,\omega_{\mathrm{THz}}$, $1.4\,\omega_{\mathrm{THz}}$, $1.8\,\omega_{\mathrm{THz}}$, and $2.2\,\omega_{\mathrm{THz}}$ components.

We also find another peak in the amplitude spectra of $\langle m_i^* \rangle$ of the 1.0 THz pulse centered at ~0.6 THz [see Fig. 3.12(b)]. If the current density is modulated by $a\,\omega_{\mathrm{THz}}$, where for this case $a < 1$, then it will have $(1 \pm a)\,\omega_{\mathrm{THz}}$ components, which are the low– and high–frequency components located at ~0.4THz and ~1.6 THz, respectively, shown in figure 3.8(d). We have to note that since these two peaks are broad, and due to the complicated temporal emission and structures, the central frequencies of the HFC and LFC do not perfectly match. It is important to note that while THz high–order harmonics are generated by both intervalley and intravalley effects, and the LFC and HFC are purely intravalley effects, reflecting the nonparabolicity of the conduction band.

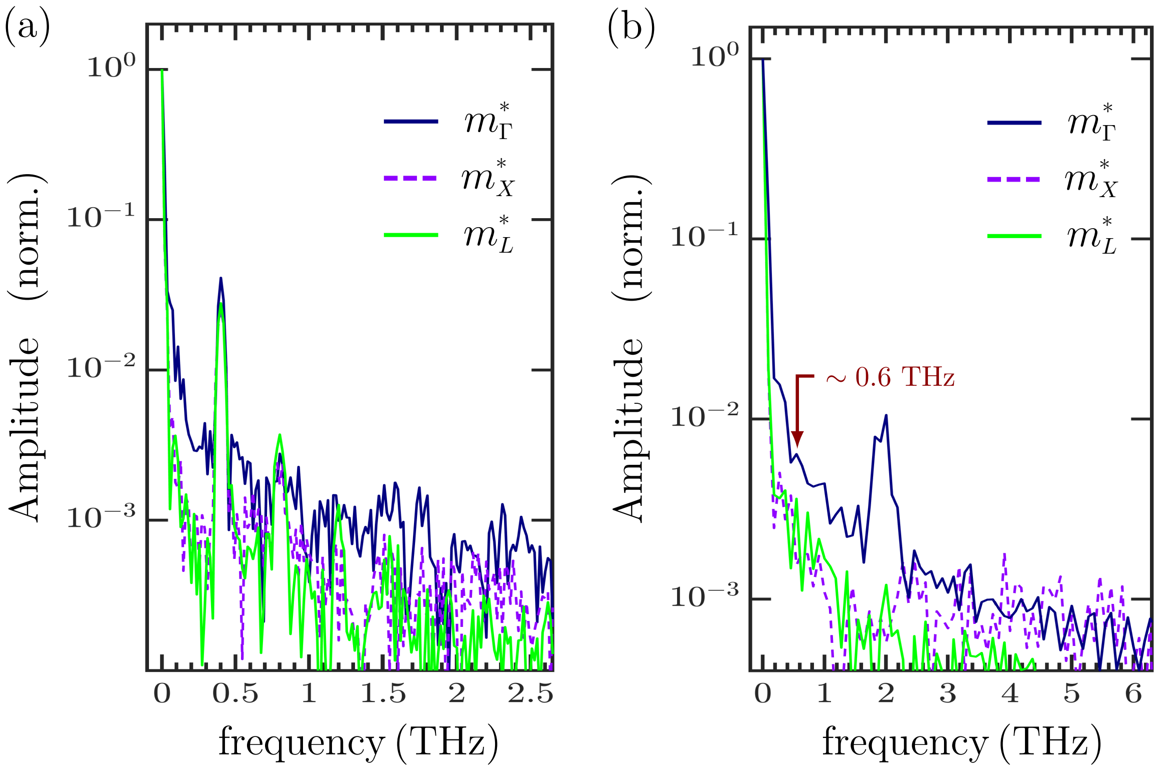

Figure 3.12: Amplitude spectra of each average carrier effective mass for the incident peak fields at (a) 350 kV/cm for 0.2 THz and (b) 114 kV/cm for 1.0 THz.

Chapter 4

Conclusions and outlooks

In this thesis, we conduct systematic numerical simulations to explain transient carrier dynamics and the nonlinear THz effects, such as the generation of THz harmonics and LFC and HFC induced by an intense multi–cycle THz pulse in an n-doped $\mathrm{In_{0.57}Ga_{0.43}As}$. Our results show that, for relatively low–frequency multi–cycle THz pulses and high incident peak fields, the carriers are accelerated to high average energy and the truncation in the current density is first achieved. The direct consequence of the distorted current phases with the driving THz fields is the clear HH peaks in the transmitted intensity spectra (up to the 11th and 7th harmonic for 0.2 THz and 0.4 THz pulses, respectively) [see Figs. 3.4(a) and 3.4(b)]. This is the result of the drastic change in the carrier effective mass in the amplitude of the electric field of the half–cycle of the original incident THz waveform. On the other hand, for relatively high frequency and low incident peak fields, the changes in the frequency are less clear due to the absence of clear current truncations. However, we can still barely observe HHG in the intensity spectra (up to the 5th order when pumping by the 1.0 THz pulses and up to the 3rd order when pumped by the 1.5 THz pulses) [see Figs. 3.4(c) and 3.4(d)].

Furthermore, for relatively high–frequency pulses and low fields, the LFC and HFC generation that appear in the transmitted amplitude spectra are due to carriers in the Γ valley accelerated to high energies, thus decreasing their mobility, causing the generated current to oscillate at lower and higher frequencies. This effect disappears at higher THz intensities since the carriers are quickly scattered into adjacent valleys [see Figs. 3.4(c) and 3.4(d)]. Furthermore, intervalley scattering does not result in clear harmonics due to the short temporal resolution. In addition, the current density will be large in this case, which can result in a huge emitted field along the entire THz waveform. We note that LFC and HFC should also be present when the InGaAs thin film is pumped with multi–cycle THz pulses with central frequencies of 0.2 and 0.4 THz. However, since the main scattering mechanism of the carriers at these particularly low frequencies is intervalley scattering, intravalley scattering is much weaker, disabling its clear observation in the transmitted spectra.

Moreover, by using the Gábor transform, we have clarified the time of emission of photons at different frequencies, providing a better understanding of the carrier dynamics. Finally, this work serves as a guideline for experiments using other possible doped semiconductors, as well as graphene [19]. Additionally, our findings show that the generation of LFC and HFC is possible in InGaAs, but since these components are much weaker than the main THz pulse, they will require measurements with a higher signal–to–noise ratio (SNR) to identify them. However, current intense THz experiments lack the SNR to measure or identify the weak low– and high–frequency components. We believe that this work will prepare the scientific community to design experiments that could be realized with the future advent of higher average power multi–cycle THz sources, allowing them to identify such relatively weak nonlinear THz signals, which could easily be overlooked.

References

[1] Lee, Y. S. *Principles of Terahertz Science and Technology.* (Springer Science Business Media, New York), 1st edition (2009).

[2] Zhang, X. C. and Xu, J. *Introduction to THz Wave Photonics.* (Springer, New York), 1st edition (2011).

[3] Laboratory of Terahertz Spectroscopy, Prague. `https://lts.fzu.cz/en/intro.php`. (2012). [Online; Accessed: 08/01/2021].

[4] Tonouchi, M. *Nature photonics* **1**, 97–105 (2007).

[5] Danciu, M., Alexa-Stratulat, T., Stefanescu, C., Dodi, G., Tamba, B. I., Mihai, C. T., Stanciu, G. D., Luca, A., Spiridon, I. A., Ungureanu, L. B., et al. *Materials* **12**, 1519 (2019).

[6] Massaouti, M., Daskalaki, C., Gorodetsky, A., Koulouklidis, A. D., and Tzortzakis, S. *Applied Spectroscopy* **67**, 1264–1269 (2013).

[7] Manceau, J.-M., Nevin, A., Fotakis, C., and Tzortzakis, S. *Applied Physics B* **90**, 365–368 (2008).

[8] Cooper, K. *Physics World* **29**, 28–31 (2016).

[9] Blanchard, F., Golde, D., Su, F. H., Razzari, L., Sharma, G., Morandotti, R., Ozaki, T., Reid, M., Kira, M., Koch, S. W., and Hegmann, F. A. *Phys. Rev. Lett.* **107**, 107401 (2011).

[10] Hafez, H. A., Chai, X., Ibrahim, A., Mondal, S., Férachou, D., Ropagnol, X., and Ozaki, T. *J. Opt.* **18**, 093004 (2016).

[11] Stone, M. R., Naftaly, M., Miles, R. E., Fletcher, J. R., and Steenson, D. P. *IEEE Trans. Microw. Theory Tech.* **52**, 2420–2429 (2004).

[12] Wu, Q. and Zhang, X. C. *Appl. Phys. Lett.* **67**, 3523–3525 (1995).

[13] Martin, C. A., Lovberg, J. A., Dean, W. H., and Ibrahim, E. in *Passive Millimeter–Wave Imaging Technology X* eds. Appleby, R. and Wikner, D. A. (International Society for Optics and Photonics, SPIE), Vol. 6548, pp. 39–48 (2007).

[14] Yang, X., Zhao, X., Yang, K., Liu, Y., Liu, Y., Fu, W., and Luo, Y. *Trends in Biotechnol.* **34**, 810–824 (2016).

[15] Akyildiz, I. F., Jornet, J. M., and Han, C. *Phys. Commun.* **12**, 16–32 (2014).

[16] Sharma, G., Razzari, L., Su, F. H., Blanchard, F., Ayesheshim, A., Cocker, T. L., Titova, L. V., Bandulet, H. C., Ozaki, T., Kieffer, J. C., Morandotti, R., Reid, M., and Hegmann, F. A. *IEEE Photonics Journal* **2**, 578–592 (2010).

[17] Razzari, L., Su, F. H., Sharma, G., Blanchard, F., Ayesheshim, A., Bandulet, H. C., Morandotti, R., Kieffer, J. C., Ozaki, T., Reid, M., and Hegmann, F. A. *Phys. Rev. B* **79**, 193204 (2009).

[18] Chai, X., Ropagnol, X., Raeis-Zadeh, S. M., Reid, M., Safavi-Naeini, S., and Ozaki, T. *Phys. Rev. Lett.* **121**, 143901 (2018).

[19] Hafez, H. A., Kovalev, S., Deinert, J. C., Mics, Z., Green, B., Awari, N., Chen, M., Germanskiy, S., Lehnert, U., Teichert, J., Wang, Z., Tielrooij, K. J., Liu, Z., Chen, Z., Naritaa, A., Müllen, K., Bonn, M., Gensch, M., and Turchinovich, D. *Nature* **561**, 507 (2018).

[20] Langer, F., Baierl, S., Huttner, U., Koch, S. W., Kira, M., Huber, M. A., Mooshammer, F., Plankl, M., Peller, D., Cocker, T. L., Repp, J., and Huber, R. in *Nonlinear Optics.* (Optical Society of America), p. NW2A.5 (2017).

[21] Langer, F., Hohenleutner, M., Schmid, C. P., Poellmann, C., Nagler, P., Korn, T., Schüller, C., Sherwin, M. S., Huttner, U., Steiner, J. T., Koch, S. W., Kira, M., and Huber, R. *Nature* **533**, 225 (2016).

[22] Langer, F., Schmid, C. P., Schlauderer, S., M. Gmitra, J. F., Nagler, P., Schüller, C., Korn, T., Hawkins, P. G., Steiner, J. T., Huttner, U., Koch, S. W., Kira, M., and Huber, R. *Nature* **557**, 76 (2018).

[23] Chai, X., Ropagnol, X., Ovchinnikov, A., Chefonov, O., Ushakov, A., Garcia-Rosas, C. M., Isgandarov, E., Agranat, M., Ozaki, T., and Savel'ev, A. *Opt. Lett.* **43**, 5463–5466 (2018).

[24] Darrow, J., Zhang, X., Auston, D. H., and Morse, J. *IEEE J. Quantum Electron.* **28**, 1607–1616 (1991).

[25] Blanchard, F., Sharma, G., Razzari, L., Ropagnol, X., Bandulet, H., Vidal, F., Morandotti, R., Kieffer, J., Ozaki, T., Tiedje, H., Haugen, H., Reid, M., and Hegmann, F. *IEEE J. Sel. Top. Quantum Electron.* **17**, 5–16 (2011).

[26] Boyd, R. W. *Nonlinear Optics.* (Academic Press, Inc., USA), 3rd edition (2008).

[27] Chai, X., Ropagnol, X., Mora, L. S., Raeiszadeh, S. M., Safavi-Naeini, S., Blanchard, F., and Ozaki, T. *Sci. Rep.* **10**, 15426 (2020).

[28] Ashcroft, N. W. and Mermin, N. D. *Solid State Physics.* (Saunders College, Philadelphia, USA), 1st edition (1976).

[29] Ibach, H. and Lüth, H. *Solid–State Physics: An Introduction to Principles of Materials Science.* (Springer Berlin Heidelberg, Heidelberg, Germany), 4th edition (2009).

[30] Böer, H. K. W. and Pohl, U. *Semiconductor Physics.* (Springer International Publishing, Berlin, Germany), 1st edition (2018).

[31] Jacoboni, C. and Reggiani, L. *Rev. Mod. Phys.* **55**, 645–705 (1983).

[32] Lundstrom, M. *Fundamentals of Carrier Transport.* (Cambridge University Press, Cambridge, UK), 2nd edition (2000).

[33] Lebwohl, P. and Price, P. *Solid State Commun.* **9**, 1221–1224 (1971).

[34] Oh, K. H., Ong, C. K., and Tan, B. T. G. *J. Phys. Chem. Solids* **53**, 555–559 (1992).

[35] Reklaitis, A. *Phys. Status Solidi B* **249**, 1566–1570 (2012).

[36] Brunetti, R. and Jacoboni, C. *Transient and Stationary Properties of Hot–Carrier Diffusivity in Semiconductors.* in *Semiconductors Probed by Ultrafast Laser Spectroscopy*, ed. Alfano, R. R. (Academic Press, Inc., New York), pp. 367–412 (1984).

[37] Jacoboni, C. and Lugli, P. *The Monte Carlo Method for Semiconductor Device Simulation.* (Springer–Verlag Wien, New York), 1st edition (1989).

[38] Ropagnol, X., Khorasaninejad, M., Raeiszadeh, M., Safavi-Naeini, S., Bouvier, M., Côté, C. Y., Laramée, A., Reid, M., Gauthier, M. A., and Ozaki, T. *Opt. Express* **24**, 11300 (2016).

[39] Ropagnol, X., Kovács, Z., Gilicze, B., Zhuldybina, M., Blanchard, F., Garcia-Rosas, C. M., Szatmári, S., Földes, I. B., and Ozaki, T. *New J. Phys.* **21**, 113042 (2019).

[40] Darrow, J., Zhang, X.-C., Auston, D., and Morse, J. *IEEE J. Quantum Electron.* **28**, 1607–1616 (1992).

[41] Reimann, K. *Rep. Prog. Phys.* **70**, 1597–1632 (2007).

[42] Kampfrath, T., Tanaka, K., and Nelson, K. *Nat. Photonics* **7**, 680–690 (2013).

[43] Ma, C. and Xu, X. *Nucl. Fusion* **57**, 016002 (2016).

[44] Ni, S., Chai, S., Wu, S. S., Cui, P. F., Yu, J., and Cong, S. L. *Chem. Phys.* **534**, 110749 (2020).

[45] Chefonov, O. V., Ovchinnikov, A. V., Romashevskiy, S. A., Chai, X., Ozaki, T., Savel'ev, A. B., Agranat, M. B., and Fortov, V. E. *Opt. Lett.* **42**, 4889–4892 (2017).

[46] Salén, P., Basini, M., Bonetti, S., Hebling, J., Krasilnikov, M., Nikitin, A. Y., Shamuilov, G., Tibai, Z., Zhaunerchyk, V., and Goryashko, V. *Phys. Rep.* **836–837**, 1–74 (2019).

[47] Blanchard, F., Razzari, L., Bandulet, H. C., Sharma, G., Morandotti, R., Kieffer, J. C., Ozaki, T., Reid, M., Tiedje, H. F., Haugen, H. K., and Hegmann, F. A. *Opt. Express* **15**, 13212–13220 (2007).

[48] Rice, A., Jin, Y., Ma, X. F., Zhang, X. C., Bliss, D., Larkin, J., and Alexander, M. *Appl. Phys. Lett.* **64**, 1324–1326 (1994).

[49] Chang, G., Divin, C. J., Liu, C. H., Williamson, S. L., Galvanauskas, A., and Norris, T. B. *Opt. Express* **14**, 7909–7913 (2006).

[50] Sell, A., Leitenstorfer, A., and Huber, R. *Opt. Lett.* **33**, 2767–2769 (2008).

[51] Hirori, H., Doi, A., Blanchard, F., and Tanaka, K. *Appl. Phys. Lett.* **98**, 091106 (2011).

[52] Zhang, Z., Chen, Y., Chen, M., Zhang, Z., Yu, J., Sheng, Z., and Zhang, J. *Phys. Rev. Lett.* **117**, 243901 (2016).

[53] Vicario, C., Monoszlai, B., and Hauri, C. P. *Phys. Rev. Lett.* **112**, 213901 (2014).

[54] Schubert, O., Hohenleutner, M., Langer, F., Urbanek, B., Lange, C., Huttner, U., Golde, D., Meier, T., Kira, M., Koch, S. W., and Huber, R. *Nat. Photonics* **8**, 119 (2014).

[55] Sharma, G., Singh, K., Al-Naib, I., Morandotti, R., and Ozaki, T. *Opt. Lett.* **37**, 4338–4340 (2012).

[56] Sharma, G., Singh, K., Ibrahim, A., Al-Naib, I., Morandotti, R., Vidal, F., and Ozaki, T. *Opt. Lett.* **38**, 2705–2707 (2013).

[57] Ibrahim, A., Férachou, D., Sharma, G., Singh, K., Kirouac-Turmel, M., and Ozaki, T. *Sci. Rep.* **6**, 23107 (2016).

[58] Razavipour, H., Yang, W., Guermoune, A., Hilke, M., Cooke, D. G., Al-Naib, I., Dignam, M. M., Blanchard, F., Hafez, H. A., Chai, X., Ferachou, D., Ozaki, T., Lévesque, P. L., and Martel, R. *Phys. Rev. B* **92**, 245421 (2015).

[59] Shan, J., Dadap, J. I., and Heinz, T. F. *Opt. Express* **17**, 7431–7439 (2009).

[60] Shimano, R., Yumoto, G., Yoo, J. Y., Matsunaga, R., Tanabe, S., Hibino, H., Morimoto, T., and Aoki, H. *Nat. Commun.* **4**, 1841 (2013).

[61] Sato, M., Higuchi, T., Kanda, N., Konishi, K., Yoshioka, K., Suzuki, T., Misawa, K., and Kuwata-Gonokami, M. *Nature Photon.* **7**, 724–731 (2013).

[62] Lu, X. and Zhang, X.-C. *Phys. Rev. Lett.* **108**, 123903 (2012).

[63] Zhang, Z., Chen, Y., Cui, S., He, F., Chen, M., Zhang, Z., Yu, J., Chen, L., Sheng, Z., and Zhang, J. *Nature Photon.* **12**, 554–559 (2018).

[64] van der Valk, N. C. J., van der Marel, W. A. M., and Planken, P. C. M. *Opt. Lett.* **30**, 2802–2804 (2005).

[65] Yasumatsu, N. and Watanabe, S. *Rev. Sci. Instrum.* **83**, 023104 (2012).

[66] Nagashima, T., Tani, M., and Hangyo, M. *J. Infrared Milli. Terahz. Waves* **34**, 740–775 (2013).

[67] Nemoto, N., Higuchi, T., Kanda, N., Konishi, K., and Kuwata-Gonokami, M. *Opt. Express* **22**, 17915–17929 (2014).

[68] Takai, M., Takeda, M., Sasaki, M., Tachizaki, T., Yasumatsu, N., and Watanabe, S. *Appl. Phys. Lett.* **105**, 151103 (2014).

[69] Yasumatsu, N., Kasatani, A., Oguchi, K., and Watanabe, S. *Appl. Phys. Express* **7**, 092401 (2014).

[70] Lü, Z., Zhang, D., Meng, C., Sun, L., Zhou, Z., Zhao, Z., and Yuan, J. *Appl. Phys. Lett.* **101**, 081119 (2012).

[71] Oguchi, K., Iwasaki, H., Okano, M., and Watanabe, S. *Appl. Phys. Lett.* **108**, 011105 (2016).

[72] Bohren, C. and Huffman, D. R. *Absorption and Scattering of Light by Small Particles.* (Wiley Science Paperback Series, Chichester, New York) (1998).

[73] Azzam, R. M. and Bashara, N. M. *Ellipsometry and Polarized Light.* (North Holland Personal Library, Amsterdam) (1987).

[74] van der Valk, N. C. J., Wenckebach, T., and Planken, P. C. M. *J. Opt. Soc. Am. B* **21**, 622–631 (2004).

[75] Goldstein, D. H. *Polarized Light.* (CRC Press, Boca Raton, Florida), 3rd edition (2011).

[76] U., S. K., Mahato, K. K., and Mazumder, N. *Lasers Med. Sci.* **34**, 1283–1293 (2019).

[77] Qi, J., He, H., Ma, H., and Elson, D. S. *Opt. Lett.* **42**, 4048–4051 (2017).

[78] Reddy, S. G., Prabhakar, S., Chithrabhanu, P., Singh, R. P., and Simon, R. *Appl. Opt.* **55**, B14–B19 (2016).

[79] Dong, H., Gong, Y. D., Paulose, V., Shum, P., and Olivo, M. *Opt. Express* **17**, 23044–23057 (2009).

[80] Peinado, A., Lizana, A., Vidal, J., Iemmi, C., and Campos, J. *Opt. Express* **18**, 9815–9830 (2010).

[81] Born, M. and Wolf, E. *Principles of Optics.* (Cambridge University Press), 7th edition (1999).

[82] Hecht, E. *Optics.* (Addison–Wesley), 4th edition (1998).

[83] Mukamel, S. *Principles of Nonlinear Optical Spectroscopy.* (Oxford University Press, London), 1st edition (1999).

[84] Avetisyan, Y. and Tonouchi, M. *Photonics* **6**, 9 (2019).

[85] Yeh, K.-L.and Hoffmann, M. C., Hebling, J., and Nelson, K. A. *Appl. Phys. Lett.* **90**, 171121 (2007).

[86] Carr, G. L., Martin, M. C., McKinney, W. R., Jordan, K., Neil, G. R., and Williams, G. P. *Nature* **420**, 153–156 (2002).

[87] Hirori, H., Nagai, M., and Tanaka, K. *Phys. Rev. B* **81**, 081305 (2010).

[88] Ogawa, T., Watanabe, S., Minami, N., and Shimano, R. *Appl. Phys. Lett.* **97**, 041111 (2010).

[89] Wright, A. R., Xu, X. G., Cao, J. C., and Zhang, C. *Appl. Phys. Lett.* **95**, 072101 (2009).

[90] Ropagnol, X., Morandotti, R., Ozaki, T., and Reid, M. *Opt. Lett.* **36**, 2662–2664 (2011).

[91] Ropagnol, X., Blanchard, F., Ozaki, T., and Reid, M. *Appl. Phys. Lett.* **103**, 161108 (2013).

[92] Al-Naib, I., Sipe, J. E., and Dignam, M. M. *Phys. Rev. B* **90**, 245423 (2014).

[93] Bowlan, P., Martinez-Moreno, E., Reimann, K., Elsaesser, T., and Woerner, M. *Phys. Rev. B* **89**, 041408 (2014).

[94] Corkum, P. B. *Phys. Rev. Lett.* **71**, 1994–1997 (1993).

[95] Popmintchev, T., Chen, M., Arpin, P., Murnane, M. M., and Kapteyn, H. C. *Nature Photon.* **4**, 822 (2010).

[96] Qiu, J., Li, Y., and Jia, Y. *Persistent Phosphors: From Fundamentals to Application.* (Elsevier Science Publishing Co. Inc.), 1st edition (2020).

[97] Kushner, M. J. *J. Appl. Phys.* **58**, 4024–4031 (1985).

[98] Thompson, B. E., Sawin, H. H., and Fisher, D. A. *J. Appl. Phys.* **63**, 2241–2251 (1988).

[99] Feoktistov, V. A., Mukhovatova, A. V., Popov, A. M., and Rakhimova, T. V. *J. Phys. D: Appl. Phys.* **28**, 1346–1383 (1995).

[100] Bogaerts, A. and Gijbels, R. *IEEE Trans. Plasma Sci.* **27**, 1406–1415 (1999).

[101] Seebeck, T. J. Magnetische Polarisation der Metalle und Erze durch Temperatur–Differenz, Abhandlungen der physikalischen Klasse der Königlichen Akademie der Wissenschafften zu Berlin, Aus den Jahren 1822 und 1823. pp. 265–373 (1825). Extracts from four lectures delivered at the Academy of Sciences in Berlin on August 16, (1821), October 18, 25 (1821), and February 11 (1822).

[102] Faraday, M. *Philos. Trans. R. Soc. Lond.* **123**, 23–54 (1833).

[103] Königsberger, T. and Weiss, T. Über die thermoelektrischen Effekte (Thermokräfte, Thomsonwärme) und die Wärmeleitung in einigen Elementen und Verbindungen und über die experimentelle Prüfung der Elektronentheorien. *Ann. Phys.* **35**, 1–46 (1911).

[104] Busch, G. *Eur. J. Phys.* **10**, 254–264 (1989).

[105] Volta, A. Del modo di render sensibilissima la più debole electtricità sia naturale, sia artiliciale. *Phil. Trans. R. Soc.* **72**, 237–281 (1782).

[106] Hittorf, J. W. Über das elektrische Leitvermögen des Schwefelsilbers und des Halbschwefelkupfers. *Ann. Phys., Lpz.* **84**, 1–28 (1851).

[107] Braun, F. Über die Stromleitung durch Schwefelmetalle. *Ann. Phys. Chem.* **153**, 556–563 (1874).

[108] Huff, H. R. *AIP Conf. Proc.* **550**, 3–32 (2001).

[109] Valsaraj, N., Sabbah, R., Jones, W., Ikossi-Anastasiou, K., Kyono, C. S., Binari, S. C., Kruppa, W., and Dietrich, H. in *Proceedings of 28th Southeastern Symposium on System Theory.* pp. 353–357 (1996).

[110] Waldrop, M. *Nature* **530**, 144–147 (2016).

[111] Batra, G., Jacobson, Z., Madhav, S., Queirolo, A., and Santhanam, N. *McKinsey & Company, New York, NY, USA, Tech. Rep* (2018).

[112] Lanin, A. and Zheltikov, A. M. *JETP letters* **104**, 449–452 (2016).

[113] Lanin, A. A., Stepanov, E. A., Fedotov, A. B., and Zheltikov, A. M. *Optica* **4**, 516–519 (2017).

[114] Cox, J. D., Marini, A., and García De Abajo, F. J. *Nat. Commun.* **8**, 1–7 (2017).

[115] Priori, E., Cerullo, G., Nisoli, M., Stagira, S., De Silvestri, S., Villoresi, P., Poletto, L., Ceccherini, P., Altucci, C., Bruzzese, R., and de Lisio, C. *Phys. Rev. A* **61**, 063801 (2000).

[116] Brabec, T. and Krausz, F. *Rev. Mod. Phys.* **72**, 545–591 (2000).

[117] Paul, P. M., Toma, E. S., Breger, P., Mullot, G., Augé, F., Balcou, P., Muller, H. G., and Agostini, P. *Science* **292**, 1689–1692 (2001).

[118] Sze, S. and Ng, K. K. *Physics of Semiconductor Devices.* (John Wiley and Sons, Inc., New Jersey), 3rd edition (2006).

[119] Long, A. P., Beton, P. H., and Kelly, M. J. *J. Appl. Phys.* **62**, 1842–1849 (1987).

[120] Goldberg, Y. A. and Schmidt, N. M. *Gallium Indium Arsenide ($Ga_xIn_{1-x}As$).* in *Handbook Series on Semiconductor Parameters*, eds. Levinshtein, M., Rumyantsev, S., and Shur, M. (World Scientific, London) Vol. 2, pp. 62–88 (1996).

[121] Koster, G. F. and Slater, J. C. *Phys. Rev.* **95**, 1167–1176 (1954).

[122] Vasileska, D. and Goodnick, S. M. *Mater. Sci. Eng. Rep.* **R38**, 181 (2002).

[123] Kutz, J. N. *Data–Driven Modeling and Scientific Computation: Methods for Complex Systems and Big Data.* (Oxford University Press, Inc., New York), 1st edition (2013).

[124] Mallat, S. *A Wavelet Tour of Signal Processing: The Sparse Way.* (Academic Press, Inc., Orlando), 3rd edition (2008).

[125] Tikhomirov, I., Sato, T., and Ishikawa, K. L. *Phys. Rev. Lett.* **118**, 203202 (2017).

[126] Tarekegne, A. T., Iwaszczuk, K., Zalkovskij, M., Strikwerda, A. C., and Jepsen, P. U. *New J. Phys.* **17**, 043002 (2015).

[127] Mohamed, M., Bharthuar, A., and Ravaioli, U. *DOI: 10.4231/D38C9R505* (2015).

[128] Kuehn, W., Gaal, P., Reimann, K., Woerner, M., Elsaesser, T., and Hey, R. *Phys. Rev. B* **82**, 075204 (2010).

[129] Kuehn, W., Gaal, P., Reimann, K., Woerner, M., Elsaesser, T., and Hey, R. *Phys. Rev. Lett.* **104**, 146602 (2010).

[130] Kane, E. O. *J. Phys. Chem. Solids* **1**, 249–261 (1957).

[131] Whalley, L. D., Frost, J. M., Morgan, B. J., and Walsh, A. *Phys. Rev. B* **99**, 085207 (2019).

[132] Altschul, V. A., Fraenkel, A., and Finkman, E. *J. Appl. Phys.* **71**, 4382–4384 (1992).

[133] Ariel, V. arxiv preprint arxiv:1205.3995. (2012).

[134] Liu, W. and Wang, E. *J. Appl. Phys.* **126**, 075706 (2019).

[135] Floss, I., Lemell, C., Wachter, G., Smejkal, V., Sato, S. A., Tong, X. M., Yabana, K., and Burgdörfer, J. *Phys. Rev. A* **97**, 011401 (2018).

[136] Kono, J., Chin, A. H., Mitchell, A. P., Takahashi, T., and Akiyama, H. *Appl. Phys. Lett.* **75**, 1119–1121 (1999).

[137] Dragoman, D. and Dragoman, M. *Optical Characterization of Solids.* (Springer–Verlag Berlin Heidelberg, Berlin), 1st edition (2002).